Exploration of nanoconfined hydrated salts as phase change materials

Doctor Degree Thesis

Xiaolei Zhu

Supervisor: Prof. Dmitry Shchukin

Chemistry Department

Oct. 2020

Abstract

Phase change materials (PCMs) are efficient medium for thermal energy storage and thermal management. Hydrated salts can be used as solid-liquid PCMs with high phase change enthalpy, high thermal conductivity, nonflammability, environment friendliness and low price. However, the disadvantages like leakage of liquid phase, phase separation and degradation over thermal cycling limit their practical applications. This PhD thesis proposed the nanoconfinement of hydrated salts inside nanocontainers as an innovative way to overcome disadvantages of hydrated salts as PCMs. Specifically, the synthesis of core-shell nanocapsules and form-stable nanocomposites has been developed to control heat uptake and release properties of inorganic PCMs.

Polyethylcyanoacrylate nanocapsules with $NaOAc \cdot 3H_2O$ PCM, polymethylmethacrylate nanocapsules with $Na_2HPO_4 \cdot 12H_2O$ PCM, gelatine nanocapsules with $KAl(SO_4)_2 \cdot 12H_2O$ PCM and silica nanocapsules with $Na_2SO_4 \cdot 10H_2O$ PCM have been developed for the first time. The polyethylcyanoacrylate PCM nanocapsules have been synthesised by interfacial polymerisation and demonstrated aggregation and no phase change thermal peaks. The polymethylmethacylate PCM nanocapsules have been synthesised by solvent evaporation precipitation of polymer showing phase change peaks, but also aggregated irregular capsule particles. The gelatine nanocapsules have been synthesised by thermal denaturation and the silica nanocapsules by sol-gel deposition method demonstrating spherical, non-aggregated morphology, but without phase change thermal peaks detected. In the first part of the thesis, we have concluded that core-shell PCM nanocapsules with organic polymer or synthetic silica shell are not suitable to nanoconfine hydrated salts. Besides the problems of morphology and phase change performance, the fabrication methods are all associated with complex, multistage procedures with the use of a large amount of organic solvent.

The second part of the thesis is devoted to the incorporation of hydrated salts into natural inorganic nanocontainers. The eutectic hydrated salt mixture of $Na_2HPO_4 \cdot 12H_2O$ and $Na_2SO_4 \cdot 10H_2O$ in 1:1 mass ratio has been chosen as a target PCM due to its thermal transition temperature range for loading into halloysite, bentonite, diatomite and sepiolite mineral hosts by vacuum impregnation. It was the first time to apply these four mineral materials to load eutectic hydrated salt to study the form-stable hydrated salt PCM nanocomposites for thermal energy storage. Controlled phase change properties have been demonstrated for halloysite and sepiolite nanocontainers. The hydrated salt PCM retained in halloysite nanotubes due to the electrostatic interaction between PCM and the inner lumen of halloysite. The crystal structure of PCM did not change after loading into halloysite. With 67% effective loading of PCM, the nanocontainer composite exhibited the melting temperature of 35.8 ˚C and the melting enthalpy of 142 $J \cdot g^{-1}$. During the thermal cycling tests, it has shown no phase separation and the thermal stability over 50 cycles.

For sepiolite form-stable nanocomposite, the effective loading of PCM has reached 88% with the melting enthalpy of 185 $J \cdot g^{-1}$, and the melting temperature of 38.1 °C. The highly loaded nanocomposite system has shown stable thermal cycling property over 50 cycles. No phase separation was observed during the cycling. The crystal structure of PCM has been remained inside nanocontainers. The hydrogen bonding sites on the surface of sepiolite, the water molecules in nanochannels of its fibrous structure and the electronic interaction between PCM and sepiolite contribute to the controlled phase change properties of inorganic PCMs.

On the other side, diatomite and bentonite nanocomposites have shown poor phase change performances, relating to the porosity, pore structure and chemical composition of the matrix materials. With low cost and abundant reserve of the clay minerals, the simple and environment-friendly fabrication procedure and the excellent phase change performances, the form-stable eutectic hydrated salt PCM nanocomposite systems with halloysite and sepiolite have great potential in thermal energy storage applications.

The methods to form nanoconfined hydrated salt PCM were also applied for the nanoconfinement of eutectic Gallium-Indium (EGaIn) PCM. Though good morphology of nanoparticles has been obtained by gelatine, poly(sodium 4-styrenesulfonate)-poly(diallyldimethyl ammonium chloride) and silica nanocapsules, no phase change behaviour was detected, as EGaIn has been oxidized in the formation of nanodroplets by ultrasonication.

Keywords: hydrated salt PCM, nanoconfinement, halloysite, sepiolite, thermal cycling

Contents

List of Figures

List of Tables

List of Schemes

Abbreviations

APTS – 3-aminopropyl triethoxysilane

CLHS – Cascaded latent heat storage

CMC – Carboxymethyl cellulose

CNT – Carbon nanotube

DHPD – Disodium hydrogen phosphate dodecahydrate

EG – Expanded graphite

EGaIn – Eutectic galium-indium alloy

EHS – Eutectic hydrated salt

FSPCM – Form-stable phase change material

G – The Gibbs free energy (J)

ΔH_m – Latent heat of melting per unit mass ($J \cdot kg^{-1}$)

HLB – Hydrophilic-lipophilic balance

HNT – Halloysite nanotube

KAlum – Potassium aluminium sulphate dodecahydrate

LHS – Latent heat storage

LHTES – Latent heat thermal energy storage

MF – Melamine-formaldehyde

MMA – Methylmethacrylate

OPCM – Organic phase change material

o/w – Oil in water

PA – Palmitic acid

PANI – Polyaniline

PAO – Poly-α-olefin

PCM – Phase change material

PDADMAC – Poly(diallyldimethyl ammonium chloride)

PDMS – Polydimethylsiloxane

PECA – Polyethylcyanoacrylate

PEG – Polyethylene glycol

PMMA – Polymethylmethacrylate

PS – Polystyrene

PSS – Poly(sodium 4-styrenesulfonate)

Q – Quantity of heat (J)

S – Entropy ($J \cdot K^{-1}$)

SAT – Sodium acetate trihydrate

SBA – Styrene-butyl acrylate

SDH – Sodium sulphate decahydrate

SDS – Sodium dodecyl sulphate

SHS – Sensible heat storage

TCS – Thermo-chemical storage

TEOS – Tetraethoxysilane

TES – Thermal energy storage

U – The internal energy (J)

w/o – Water in oil

wt% – Weight percentage

Acknowledgements

I am grateful to have the EPSRC funding offered by my supervisor Prof. Dmitry Shchukin to support my whole Ph.D. study here at the University of Liverpool. Many thanks to Prof. Shchukin, as he has given me courage and valuable suggestions when I met problems in research over the past four years. I am proud to be trained as an independent researcher during my Ph.D. study. Prof. Shchukin is the key person in my training. His guidance and his unique way of thinking as a researcher will have a profound influence on my future career.

I thank the great time spent in my group. Marios, Paula, Claudia, and Mike have helped me in the first few months to get acquainted with our lab equipment and some routines in the Chemistry Department. They are always friendly, warm-hearted and willing to be of help. The working atmosphere in our group is great. I have also enjoyed the time very much with all group members in many parties and dinners. The joyful experience is a precious treasure in my life.

Last, I would like to thank my parents. They have always trusted me and supported me with my choice. They are my backbone and source of strength to face all the struggles, pains and hardships. Thank you, Mom and Dad! I love you!

1. Introduction

Phase change materials (PCMs) store and release thermal energy during phase transformation processes. They reflect the principle of latent heat thermal energy storage (LHTES)[1], as shown in Fig. 1-1. When the temperature of phase change material achieves its phase change temperature, the heat continually added from the environment will be stored as latent heat in the material until the phase change process ends. During the phase change process, the temperature of the material kept constant at the phase change temperature.

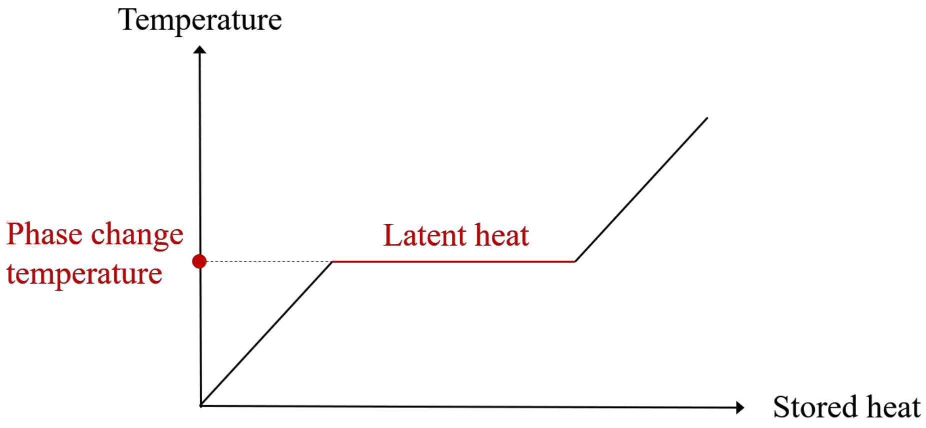

Fig. 1-1 Principle of latent heat thermal energy storage

Phase change material can store as well as release latent heat depending on the environmental temperature. So it can be repeatedly used for thermal energy storage. The working cycle of phase change material is depicted in Fig. 1-2, with the example of solid-liquid phase transformation. The solid PCM is heated and rises on its temperature until it begins to melt. During the melting process, the PCM absorbs heat and transfers into liquid state. The latent heat is stored in this process. When the liquid PCM is put into the environment with lower temperature than the freezing point, its temperature will decrease to the freezing temperature. Then, the latent heat releasing process happens during the freezing of PCM. PCM solidifies completely in the end of freezing and is ready for a repeated cycle of heating-cooling.

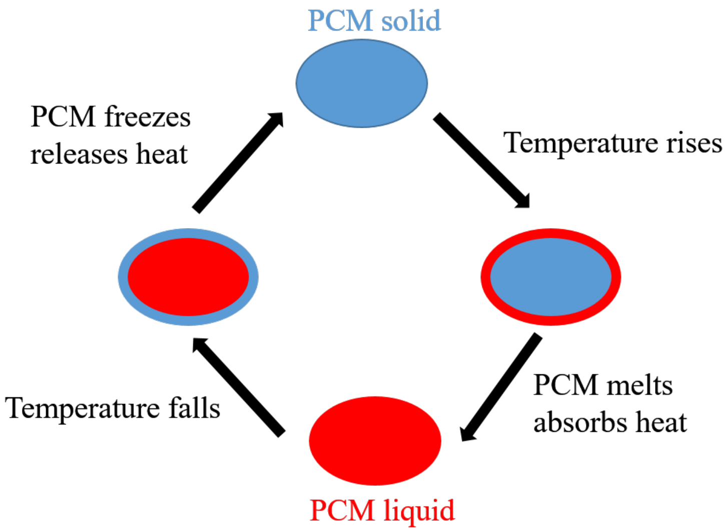

Fig. 1-2 Working cycle of phase change material

By applying PCMs, unstable and intermittent energy sources can be effectively utilised. This chapter introduces the research background on phase change material, classification of phase change materials, core-shell PCM capsules, form-stable PCM composites (FSPCM), applications of phase change material and in the last section the main content of the thesis.

1.1 Phase change materials basics

1.1.1 Energy

To address the increasing demand for energy in the 21st century, energy resources and their efficiency are in concern. Generally, the primary energy output is categorized into non-renewable and renewable energy. Non-renewable energy refers mainly to fossil fuels including coal, petroleum and natural gas. These energy resources were generated millions of years ago. They have limited reserves in the world and could not be regenerated in many lifetimes. In history, human beings have mainly lived on non-renewable energy. Along with the growing population and the process of modernisation, the demand and exploitation of fossil fuels have been largely extended in recent years. It is estimated, the global reserve of fossil fuels could only supply for 200 years.

Considering the huge disparity in the location of fossil fuels, it is with grave national strategic significance to find replacing energy resources.

Renewable energy is a good replacement for fossil fuels. In the opposite of non-renewable energy, it can be replenished in a lifetime. Resources of renewable energy include solar energy, wind energy, marine energy, bioenergy, hydropower and geothermal heat[2]. Renewable energy does not deplete. It is sustainable energy with sufficient supply. Nations or districts short of fossil fuels always have access to one or more renewable energy resources, which have the potential to meet their rising demand for energy. Besides sustainability and availability, renewable energy also shows the important advantage to environment comparing to fossil fuels. Combustion of fossil fuels produces a huge amount of carbon dioxide[3], which leads to global warming. To achieve the aim of the Paris Climate Agreement, a sharp reduction of CO_2 emission is necessary[4]. As shown in Fig.1-3, the planned reduction of CO_2 emission from 35 to 9.7 Gt/year in 2050 depends mainly on the transition from fossil fuels to renewable energy (41%) and increase of energy efficiency (40%).

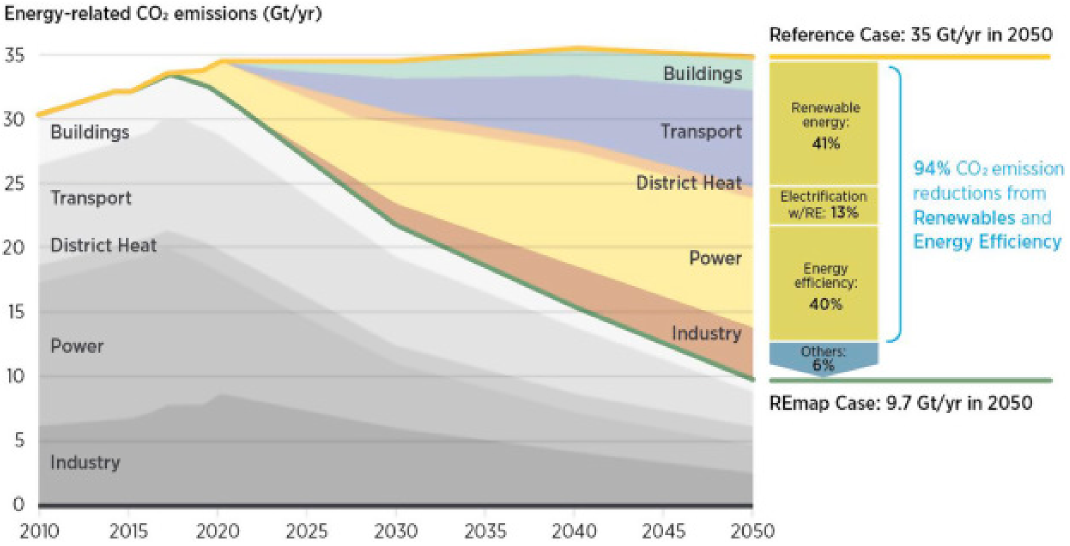

Fig.1-3 Plan of CO_2 emission reduction by technology in 2050 (Source:[5])

Despite the obvious advantages of renewable energy, fossil fuels still account for 84% of the global primary energy supply[6]. The main challenges in utilising renewable energy are its intermittent output and usually low energy intensity (watt per square metre). The strategy to address these challenges is to find medium materials to store the intermittent energy in high density and release the stored energy according to requirements steadily and efficiently.

1.1.2 Phase change materials for thermal energy storage

1.1.2.1 Latent heat storage in thermal energy storage

Energy storage is to conserve a specific form of energy for later utilisation. The types of energy available for storage include mechanical, chemical, electrical, electrochemical and thermal energy, etc. According to assessment by the European Association for Storage of Energy (EASE), thermal energy storage technology is highly recommended due to the convenience in the conventional generation, renewable generation, transmission, distribution and customer services[7].

With different mechanisms thermal energy storage systems can be classified into sensible heat storage (SHS), latent heat storage (LHS) and thermo-chemical storage (TCS)[8]. Sensible heat storage works with the change of temperature and no phase change occurs during the heat-storing and releasing processes. In the opposite of sensible heat storage, latent heat storage depends on a phase change to achieve heat storage and the temperature keeps constant. Thermo-chemical storage uses the enthalpy from reversible chemical reactions to achieve energy storage and release.

Comparing to sensible heat storage, latent heat storage has obvious advantages of high energy storage intensity and density, meaning more energy is stored per unit space and unit weight, as well as small temperature change. To illustrate these advantages, examples of sensible heat storage and latent heat storage are showed in Tab.1-1.

Tab. 1-1 Heat storage properties of sensible heat storage materials and phase change materials (Source:[9])

	Sensible Heat Storage		Phase Change Materials	
	Rock	Water	Organic	Inorganic
Latent heat of fusion ($J \cdot g^{-1}$)	/	/	190	230
Specific heat ($J \cdot g^{-1} \cdot K^{-1}$)	1	4.2	2	2
Density ($g \cdot cm^{-3}$)	2.24	1	0.8	1.6
Mass for storing 10^6 kJ (kg)*	67000	16000	5300	4350
Relative mass**	15	4	1.25	1
Volume for storing 10^6 kJ (m^3)*	30	16	6.6	2.7
Relative volume**	11	6	2.5	1

**ΔT = 15 K for SHS materials to calculate mass and volume for storing 10^6 kJ heat*

*** Relative mass and Relative volume are based on inorganic PCM properties taken as one*

Water is a usual liquid sensible heat storage material, while a rock is a usual solid sensible heat storage material. PCMs are materials representing latent heat storage principle. Typical data for the organic and inorganic PCMs are listed. Water exhibits a high specific heat, which favours heat storage. However, for storing the same amount of heat, the mass of water needed is 3.2 to 4 times of PCM, and the volume is 2.4 to 6 times of PCM. Rock shows a lower specific heat than water and PCM. Due to its high density, even more mass with 12 to 15 times of PCM and more volume with 4.4 to 11 times of PCM are required to store the same amount of heat. Further, PCM stores energy according to the latent heat of fusion during the phase change, while water and rock do not have phase change during the heat storage thus showing no latent heat of fusion but only specific heat. The latent heat of fusion by inorganic PCM is 230 times as big as the specific heat of rock, and 54.8 times as that of water. The storage capacity of PCMs using latent heat storage mechanism is much better than sensible heat storage materials. Regarding the change of temperature, by sensible heat storage the heat stored is proportional to the increase of temperature. Higher temperature brings the problem of high vapour pressure by liquid sensible heat storage materials, which requires extra costly equipment to withstand the pressure in applications. The little swing of temperature by PCMs is beneficial in practical thermal energy storage applications.

This property could even specifically utilised for thermal management applications[10][11].

Thermo-chemical storage occurs through a reversible chemical reaction at equilibrium temperature with specific reaction heat[12]–[14]. Criteria such as thermodynamics, kinetics, engineering design, etc. determine if a thermo-chemical storage system could be practically applied and cost-efficient. Currently, researches on thermo-chemical storage systems are still restrained in the laboratory stage due to the complexity involved in the operation. In this thesis, latent heat storage in thermal energy storage is concerned.

1.1.2.2 Properties of phase change materials for thermal energy storage

Phase change materials are medium to realize thermal energy storage and thermal management in an efficient and elegant way. By utilising PCMs, the intermittently generated renewable energy can guarantee a continuous energy supply, the efficiency of energy output can be increased to requirement, the waste heat produced in industry and domestic scenarios can be collected and reused, the mismatch between energy demand and supply can be compensated, the transfer and redistribution of energy can be possible, also the temperature can be regulated for specific applications.

PCMs are associated with latent heat storage system. Taking the phase change from solid to liquid as an example, the storage capacity of a PCM is expressed in Eq. 1-1.

$$Q = \int_{T_i}^{T_m} mC_p \, dT + ma_m \Delta H_m + \int_{T_m}^{Tf} mC_p dT \qquad \text{(Eq. 1-1)}$$

Q:quantity of heat (J), T_i*: start temperature (˚C),* T_m*: melting temperature (˚C),* T_f*: end temperature (˚C), m: mass of PCMs (kg),* C_p*: specific heat (J* kg^{-1} K^{-1}*),* a_m*: mass fraction of melted PCMs,* ΔH_m*: latent heat of melting per unit mass (J* kg^{-1}*)* (Source:[15])

To ignore the short sensible heat change processes before and after the melting process, and to calculate the whole quantity of heat stored for complete melting, Eq. 1-1 can be simplified as Eq. 1-2:

$$Q = a_m \Delta H_m \qquad \text{(Eq. 1-2)}$$

In a latent heat storage system, the possible phase changes of a substance could be solid to liquid, solid to solid, solid to gas, liquid to gas and the respective inverse process. The phase change process between solid and solid involves less latent heat per unit mass than the process between solid and liquid. On the other hand, the phase changes between solid and gas or between liquid and gas are associated with big volume changes, which bring serious operational problems. Thus, the phase change between solid and liquid plays the most important role in practical applications of PCMs. It is the focus of this thesis.

PCMs chosen for thermal energy storage in practice should meet a series of chemical, physical, thermal, kinetic and economical requirements.

The chemical requirements are:

I. Chemical stable for long-term
II. Compatible with construction materials
III. Non-flammable
IV. Non-toxic

PCMs can be chemically decomposed or react with oxygen in the atmosphere over long-term thermal cycling, thus losing the original phase change properties. In the case of hydrated salts PCMs, the loss of hydrated water leads to degradation of heat storage capacity. The construction materials could be incompatible with PCMs, causing the problem of corrosion. The fire hazard and toxicity of PCMs cause safety concerns in the operation.

The physical requirements include:

I. Favourable phase equilibrium
II. Small volume change during phase transformation
III. Low vapour pressure
IV. High density
V. Congruent melting

In a favourable phase equilibrium, the solid and liquid phase of PCMs are stabilised. Thus the heat can be steadily stored and released. Over the phase transformation from solid to liquid, the volume of PCMs gets bigger and generates higher vapour pressure. To avoid leakage of PCMs out of the container into the environment, volume and vapour pressure change should be kept as low as possible. A high density enables a large quantity of heat stored in the limited size and weight of PCMs, which is favourable for energy storage, transformation, and redistribution. Congruent melting enables a uniform heat storage performance and also suppresses the degradation of PCMs.

The following thermal requirements should be taken into account:

I. Desired phase change temperature
II. High latent heat of phase-transition
III. Good thermal conductivity

Different applications have a specific operating temperature. PCMs selected should exhibit the corresponding phase change temperature. High latent heat of fusion means a big amount of heat can be stored per unit mass on melting. Good thermal conductivity enables fast heat transfer, which facilitates heat storage and release.

The kinetic requirements are:

I. No supercooling
II. Adequate crystallisation

Supercooling is a usual problem for hydrated salts. The delay in nucleation leads to a lower freezing temperature than the melting temperature. In case of insufficient crystallisation, apparent part of liquid PCMs do not turn to solid in freezing, thus the heat released is incomplete.

The economical requirements are:

I. Low cost
II. Easy access

For practical applications, PCMs should be available in big quantities and at a low cost. These requirements are set for ideal PCMs. In reality, no PCM meets all the criteria perfectly. Researches to improve properties of PCMs according to their respective shortcomings can increase their potential in applications.

1.1.3 Thermodynamics of phase change materials

From the thermodynamical perspective, phase change or phase transition can be mainly classified as first-order and second-order. According to Ehrenfest's theory[16], the first derivatives of the thermodynamic free energy are discontinuous involving several thermodynamic variables for the first-order phase transition. The transitions among solid, liquid and gas are first-order transitions, which always associate with latent heat.

$$G(P,T) = U - ST + PV \qquad \text{(Eq. 1-3)}$$

$$dG = -SdT + VdP \qquad \text{(Eq. 1-4)}$$

$$(\partial G/\partial T)_p = -S \qquad \text{(Eq. 1-5)}$$

$$(\partial G/\partial P)_T = V \qquad \text{(Eq. 1-6)}$$

G: the Gibbs free energy (J), U: the internal energy (J), P: pressure (Pa), T: temperature (K), V: volume (m^3), S: entropy ($J{\cdot}K^{-1}$)

On the first-order transition of pure material, pressure and temperature are constants, there is no change in the Gibbs free energy (dG = 0). However, the derivation of the Gibbs free energy with temperature (Eq.1-5) and pressure (Eq.1-6) as variables results in minus entropy and volume respectively, which are not zero. They are the first derivatives of Gibbs free energy with finite changes and show a discontinuity in thermodynamic functions in the phase transition process.

For the second-order phase transition, the first derivatives of the Gibbs free energy are continuous while the second derivatives are discontinuous. Examples of second-order phase transition are ferromagnetic phase transition, superfluid and superconducting phase transition. In this thesis, only the first-order phase transition is concerned, as latent heat storage is the research object.

The first-order phase transitions including solid to liquid and liquid to gas as well as the sensible heating processes in between are displayed in the temperature-time diagram in Fig. 1-4. This T-t diagram can be understood from a fundamental physical perspective with the help of the kinetic molecular theory of matter[17][18]. According to the theory, material is composed of a huge number of molecules. All the molecules are in continuous Brownian movement. At the starting point O, the material has the lowest temperature T_O. It is in a highly ordered crystalline solid-state with low entropy. The molecules perform small oscillations in a fixed lattice spacing. From O to A, the amplitude of the oscillations is enlarged by heat input, resulting in the increase of the mean kinetic energy of molecules. As a macroscopic measure of the mean kinetic energy of molecules, the temperature shows an increase. The range OA is a sensible heating process. At point A, where the material starts to melt, the amplitude of oscillations has increased to such a big extent, that individual molecules leave their lattice positions and the lattice arrangement is destructed. The range AB is a melting process with the transition from the ordered solid phase to the much disordered liquid phase. The heat added to the material speeds up the movement of the molecules and their potential energy is thus increased. Latent heat has been stored in the material. The temperature is not changed, as the mean kinetic energy of molecules is not increased. From B to C, the temperature increases as the heat enhances the movement of the molecules without changing the macroscopic liquid state. At point C, the energy replenished enables some molecules to get rid of the attraction forces from other molecules and move randomly within a much larger space. The material turns from the liquid phase to the vapour phase from C to D. The change of the volume in this process is significant. The heat added after D increases the temperature of the material in the gas state.

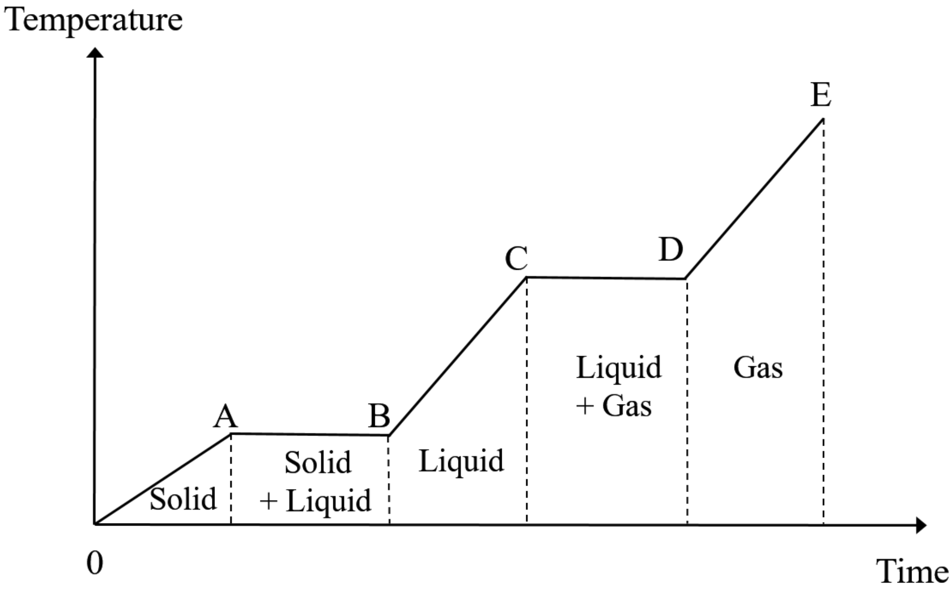

Fig. 1-4 Temperature-time diagram for phase transitions on heating (A-B-C-D-E) (Source:[19])

1.2 Classification of phase change materials

With high latent heat of fusion and small volume change, the solid-liquid phase transitions are much more interesting for practical applications than other phase transitions such as solid-solid and solid-gas. Phase change materials in research in this thesis are all about solid-liquid transitions. According to the melting temperature, PCMs can be grouped to low, middle and high-temperature PCMs[20]. Low-temperature refers to the melting temperature below 15 ℃ with the common applications in the food industry and air conditioning. Middle-temperature is the range 15-90 ℃ including the majority of PCMs applications, such as energy-saving and temperature regulation in buildings, solar energy storage, thermal insulation in textiles, thermal management of electronics equipment, temperature control in the transport of drugs and heat therapy in the medical area, etc. A high- temperature PCM exhibits a melting temperature above 90 ℃, applied mainly for aerospace and some industrial applications.

Regarding the chemical nature of the materials, solid-liquid PCMs can be classified as organic PCMs (OPCMs) and inorganic PCMs, as shown in Fig. 1-5. The discussion of the properties of different PCMs in this section is according to this classification.

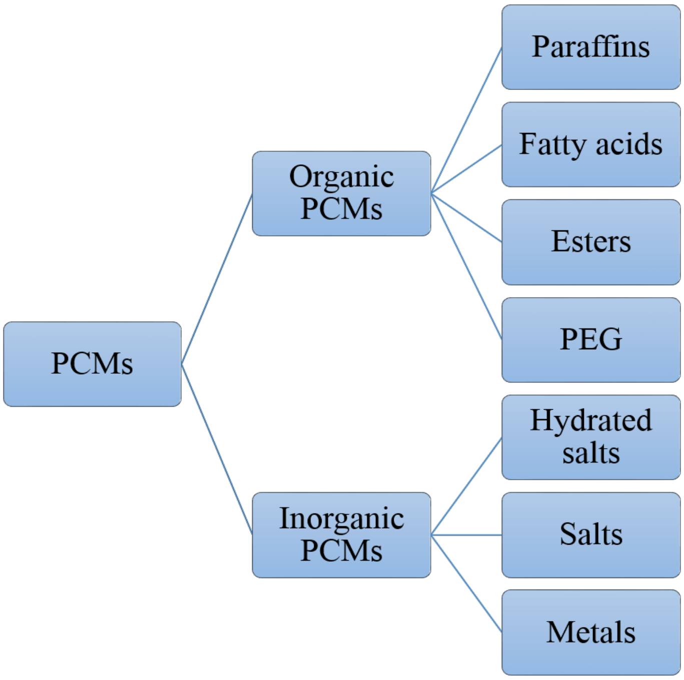

Fig. 1-5 Classification of phase change materials

1.2.1 Organic phase change materials

The common organic PCMs (OPCMs) include paraffins, fatty acids, fatty acid esters, and polyethylene glycols.

Paraffins

Paraffins are saturated hydrocarbons expressed as C_nH_{2n+2}. They are non-toxic solid-liquid PCMs, and the melting temperature increases along with the number of carbon atoms. From C_5 to C_{15} for example, the melting temperature rises from 23 to 67 °C[15]. They exhibit high thermal reliability and cycling stability. No phase separation and supercooling occur in phase transitions. Therefore, they are very popular PCMs in middle-temperature applications. However, they show a low flash point, which raises concerns for safety issues especially used in building materials. They are chemically compatible with most container materials. However, some plastic containers such as poly-olefins could suffer from light corrosion as they show chemical similarity to paraffin. At room temperature, paraffin is chemically inert. At higher temperature over 40 °C, however, oxidation may occur[21]. Despite the non-toxic nature of paraffins, the commercial-grade ones contain hazardous organic chemicals such as benzene, toluene, vinyl chloride and formaldehyde[21]. Especially benzene, toluene, and their derivatives are carcinogenic. Handling with these commercial paraffins should be taken precautions. Inhalation of their vapours or get touch with skin is not favourable. Also, paraffins are not biodegradable or renewable which makes the disposal environmentally unfriendly.

Fatty acids

Fatty acids have the formula of $CH_3(CH_2)_{2n}COOH$. They comprise a hydrocarbon chain and a carboxyl group in the end. The hydrocarbon chain is either saturated or unsaturated. The total number of carbon atoms is from 4 to 28. Their melting point and latent heat of fusion generally increase with the carbon atoms. Advantageous as PCMs, they have high latent heat of fusion, almost no supercooling, no phase separation and good cycling stability. However, they usually exhibit an unpleasant odour, mildly corrosive due to the carboxyl group, relatively expensive and flammable, which limits their applications in buildings.

Fatty acid esters

Fatty acid esters are fatty acid derivatives obtained from esterification with alcohols. Comparing to fatty acids, the ester PCMs do not have a disagreeable odour and less corrosive due to the absence of a carboxyl group. They have reasonable heat of fusion and good thermal stability[22]. In practice, they are often used in building materials. The easy accessibility, low cost, considerable heat of fusion and fast no supercooling are all merits. However, some fatty acid esters such as triglycerides have the problem of polymorphism, which may lead to the splitting of phase change peaks and unstable phase transition performances.

Polyethylene glycol

Polyethylene glycol (PEG) is polyether terminated with a hydroxide group expressed as $H(OC_2H_4)_nOH$. The repeating dimethyl ether group renders good crystallinity to the polymer, for example the crystallinity degrees of PEG 1000 to PEG 10000 are from 85.7% to 91.8%[23]. This property makes its heat of phase transition considerable. As the number of the repeating group increases, the molecular weight of polyethylene glycol increases, and the melting temperature and heat of fusion increase as well. As a widely applied PCM in low and middle-temperature range, polyethylene glycol shows good chemical and thermal stability, non-toxicity, non-corrosivity, and biodegradability. However, it exhibits the disadvantage of supercooling because the long polymer chains could not easily crystallise during cooling.

The thermophysical properties of some representative OPCMs from each subcategory are listed in Tab. 1-2.

Tab. 1-2 Thermophysical properties of some typical organic phase change materials[15][24]–[32]

OPCM	Nr. of C-atoms in a molecule	Melting T (°C)	Heat of fusion ($J \cdot g^{-1}$)	Density ($g \cdot cm^{-3}$)
Paraffin				
n-Hexadecane	16	18	216	0.773
n-Eicozane	20	36.6	247	0.788
n-Hexacozane	26	56.3	256	0.803
Fatty acids				
Lauric acid	12	41	183	0.87
Palmitic acid	16	61	203	0.942
Stearic acid	18	70	222	0.94
Fatty acid esters				
Methyl palmitate	16+1	27	163	0.85
Methyl stearate	18+1	38	161	0.846
Butyl stearate	18+4	17-23	140-200	0.86
PEG				
PEG 400	17+1	4.2	117.6	1.13
PEG 1000	44+1	40	168.6	1.204
PEG 10000	453+1	65.9	171.6	1.102

Usually, OPCMs are well compatible with most containers, only eventually show mild corrosivity to plastic containers due to the chemical similarity. They have stable chemical compositions and exhibit thermal stability over many phase transition cycles. The majority of OPCMs show no phase separation and little or no supercooling. However, the disadvantages of OPCMs are serious. They often have a low flash point, which makes them inflammable. Their thermal conductivity is usually less than 0.2 $W \cdot mK^{-1}$, while by hydrated salts it is often more than 0.5 $W \cdot mK^{-1}$. Their density is low, especially with low-molecular OPCMs, only about half the density of common hydrated salts. They could show considerable volume variation over the phase change process. A large portion of OPCMs, especially with technical grade, exhibit unneglectable toxicity. The pure form of OPCMs, on the other hand, are often costly.

1.2.2 Inorganic phase change materials

Inorganic PCMs include salts, hydrated salts, and metals. They have very broad applications, as their melting points span from the low-temperature range with some hydrated salts to the high-temperature range of several hundred or even over a thousand degree with salts and metals. Different kinds of blendings, including hydrated salts with each other, salts with each other, hydrated salts and salts can form eutectic mixtures with sharp phase transition point and congruent melting and freezing without phase separation. Metal elements such as Al, Cu, Mg, and Zn[33][34] can be fused to metallic alloys with large latent heat density and good thermal stability for high-temperature PCM applications.

Hydrated salts

Hydrated salts are PCMs with large potential in practical applications. They exhibit high energy storage density, better thermal conductivity than OPCMs, with low cost and abundant reserve. Unlike OPCMs, they are non-flammable, which guarantees the safe application in scenes such as industrial waste heat recovery, air conditioning, aerospace field, electric peak-shaving, etc. The melting temperature of these hydrated salts ranges from 8 to 117 °C[1]. Depending on applications, hydrated salts with a suitable melting point, large heat of fusion, reasonable thermal conductivity and high density can be chosen as PCMs. Some typical hydrated salts used as PCMs are listed according to the melting temperature from low to high in Tab. 1-3.

Tab. 1-3 Thermophysical properties of some typical hydrated salts phase change materials[15][35]–[39]

Hydrated salts	Melting T (°C)	Heat of fusion ($J\cdot g^{-1}$)	Thermal conductivity ($W\cdot mK^{-1}$)	Density ($g\cdot cm^{-3}$)
$LiClO_3\cdot 3H_2O$	8	253	n.a.	1.72
$KF\cdot 4H_2O$	18.5	231	n.a.	1.45
$CaCl_2\cdot 6H_2O$	29	190	0.54	1.56
$Na_2SO_4\cdot 10H_2O$	32	251	0.544	1.48
$Na_2CO_3\cdot 10H_2O$	33	247	n.a.	1.44
$Na_2HPO_4\cdot 12H_2O$	36	265	n.a.	1.52
$Na_2HPO_4\cdot 7H_2O$	48	170	n.a.	1.68
$Na(CH_3COO)\cdot 3H_2O$	58	226	n.a.	1.45
$Na_3PO_4\cdot 12H_2O$	69	190	n.a.	1.62
$KAl(SO_4)_2\cdot 12H_2O$	85.8	184	n.a.	1.73
$Mg(NO_3)_2\cdot 6H_2O$	89	163	0.49	1.55
$MgCl_2\cdot 6H_2O$	117	168.6	0.57	1.45

A hydrated salt, generally as $A\cdot nH_2O$, undergoes the process of dehydration during the melting. The hydrate molecules break up from the crystalline hydrated salts at the melting temperature, forming a hydrated salt with fewer water molecules as $A\cdot mH_2O$ or the anhydrous salt A in dehydration, as shown in chemical equation 1-7 and 1-8.

$$A \cdot nH_2O \rightarrow A \cdot mH_2O + (n-m)H_2O \qquad \text{(Eq. 1-7)}$$

$$A \cdot nH_2O \rightarrow A + nH_2O \qquad \text{(Eq. 1-8)}$$

Three kinds of melting behaviours are observed for hydrated salts. The first case is congruent melting, whereby the salt is completely dissolved in the hydration water. Then, there is the case of incongruent melting, for which only part of the salt gets dissolved in the hydration water. The third case is semi-congruent melting, when solid and liquid phases are in equilibrium and the solid phase consists of hydrated salts with less hydration water molecules[8].

Most hydrated salts exhibit an incongruent or semi-congruent melting behaviour. Pure salt or less hydrated salts with larger densities sediment as solid during the melting. This leads to the significant problem of phase separation. Due to the phase separation, not only the phase change temperature is no longer uniform and stable, but also the thermal energy storage capacity will continually decrease over thermal cycling. To handle the phase separation problem of hydrated salts, thickening agents are added. A thickening agent can enhance the viscosity of the liquid hydrated salts, which makes the distribution of the solid particles more evenly. Cellulose, nanocellulose, hydroxyethyl cellulose, polyethylene glycol, super absorbent polymer, silica gel have been used as thickening agents [40][41] .

Supercooling is another serious problem of hydrated salts as PCMs. A melt is supercooled when no crystal solid is formed under the expected freezing temperature. The crystallisation process includes the formation and growth of nuclei. Supercooling is kinetically favoured for crystallisation, as it provides the energy for ions to diffuse in solution and interface and to expand crystal growth plane. So hydrated salts tend to have a supercooling character on freezing. It is undesired in practical applications such as indoor temperature regulation, as the stored heat in the liquid phase will be able to release only when the surrounding temperature is very low and the temperature fluctuation cannot be controlled effectively. The most common way to overcome the supercooling is adding nucleating agents. A nucleating agent can provide a nucleation centre, allowing crystals to form and grow with less supercooling. In theory, an effective nucleating agent should have similar lattice parameters to the targeting crystal, so the distribution of charges and the electrical potential field match the target, and the ions tend to attach on the surface of the nucleating agent. However, the search of a nucleating agent is difficult in practice.

Borax is reported as a proper nucleating agent for $Na_2SO_4 \cdot 10H_2O$[42]. The supercooling is decreased by about 10°C. Wu et al.[43] have applied three types of SiO_2 nanoparticles to decrease the supercooling of $Na_2SO_4 \cdot 10H_2O$, liquid phase SiO_2, aerosol SiO_2, and RNS-A SiO_2. Aerosol SiO_2 shows the best suppressing on supercooling, which should relate to its better interaction with hydrated salts with a large specific surface area. Sutjahja et al.[44] have used Ba_2CO_3, K_2CO_3, and $SrCl_2 \cdot 6H_2O$ as nucleating agents for $CaCl_2 \cdot 6H_2O$. $SrCl_2 \cdot 6H_2O$ has the best effect.

Salts

Inorganic salts as PCMs have melting temperatures ranging from 192 to 1271 °C[9], which is suitable for high-temperature PCMs applications. They have also been used in cascaded latent heat storages (CLHS), in which a series of phase change temperatures are included from low to high[45]. Chlorides, fluorites, nitrates, sulphates, phosphates, and carbonates are commonly used salts PCMs[46]. The main drawbacks of salts are their corrosivity and leakage in a liquid state at high temperature. Porous supports have been used to fabricate composite PCMs with salts to handle these problems. Expanded graphite (EG) has been applied as matrix material[47]–[49].

Metals

The application of metals as PCMs is largely limited due to their high density and low latent heat of transition per unit mass. However, they also have some superior properties comparing to other PCMs. They have higher thermal conductivity, while OPCMs usually have a thermal conductivity about 0.2 $W \cdot mK^{-1}$ and hydrated salts have it from 0.5 to 2.0 $W \cdot mK^{-1}$ [41], the metals show several ten to over one hundred $W \cdot mK^{-1}$[34]. Electron motions are responsible for the high heat transfer capacity of metals. Unlike hydrated salts, metals do not have the problems of supercooling and corrosivity and show good thermal stability and cycling property. Besides, they have the advantages of low vapour pressure, low specific heat and high latent heat of fusion per unit volume. During the solid-liquid phase transition, the strong metallic bonds are loosened, leading to the rearrangement of metal atoms and movement of electron clouds, releasing a large quantity of heat.

The melting temperatures of metals and metal alloys are usually from several hundred to over one thousand Celsius degrees, which can be applied for high-temperature PCMs applications. Aluminium, copper, magnesium, zinc, silicon and their alloys are common metal PCMs[50]–[52].

Besides the normal metals with high melting points, there is one special class of metal with low melting points called liquid metal. They exhibit all the good properties of metals as PCMs, such as high thermal conductivity, a big gap between melting temperature and evaporation temperature, as well as good thermal stability. Their melting temperatures range from -38.9 °C by mercury to 271.4 °C by bismuth[53].

Gallium and gallium-based metal alloys are the most researched liquid metal with a low melting temperature of 8-30 °C[54]. Chi et al.[55] have applied gallium-based alloy to cool a laser system. Under vacuum, the laser system could maintain a temperature below 40 °C. Ge et al.[56] have used gallium to absorb the heat generated by USB flash drive on transferring data. Due to the good thermal conductivity and low melting point, gallium PCMs have also been used for thermal management of smartphones and computer[57][58].

1.3 Core-shell micro/nanoencapsulation of phase change materials

Core-shell encapsulation is to wrap the desired core material inside the chosen shell material. It is aimed to separate the functional core material from the environment. It has been widely used in medicine[59], biotechnology[60], catalysis[61][62], anticorrosion system[63] etc.

The encapsulation of PCM in a core-shell particle can prevent the leakage of PCM during the solid-liquid transition, so a stable phase change performance can be expected during the melting-freezing cycling. It also facilitates storage and transport of PCM, as the shell material provide a protection layer to avoid contamination and reactions with the environment. In case of hydrated salts PCMs, the shell can prevent corrosion to metal containers. With uniform shape and size, encapsulated PCM can be well distributed in matrices and show homogeneity in performance.

Depending on the size of the formed capsules, the encapsulation technique can be classified into macro encapsulation with particles bigger than 1 mm, microencapsulation with particles ranging from several µm to 1 mm and nanoencapsulation with particles smaller than 1µm. The surface-to-volume ratio increases rapidly as the radius of particles decreases. Comparing to pure PCM without encapsulation, PCM capsules show increscent surface area, which enhances the heat transformation of PCM. Furthermore, the smaller the size of a capsule, the larger the surface area-to-volume ratio. For the same volume, the surface area of microcapsules with the diameter of 100 µm is 100 times as the surface area of macrocapsules of 10 mm, and the nanocapsules of 100 nm have the surface area 1000 times as microcapsules of 100 µm. In the following, various techniques to fabricate PCM capsules with sizes in micro- or nanometre range are introduced.

1.3.1 Polymer shell encapsulation

PCM micro/nanocapsules with polymer shells can be formed by emulsion polymerisation, miniemulsion polymerisation, interfacial polymerisation and in situ polymerisation.

Emulsion polymerisation

In emulsion polymerisation, a minor medium containing PCM and insoluble monomer is dispersed in the reaction solvent under mechanical stirring. Emulsifier and surfactant are needed to obtain stable uniform emulsion. Then the initiator usually a free radical is added to initiate the polymerisation. The radical enters the emulsion droplets and induces the propagation of monomers which finally forms a polymer shell on the surface of a droplet containing PCM. Sari et al. fabricated PCM micro-/nanocapsules n-heptadecane@polystyrene (PS)[64] and n-nonadecane@polymethylmethacrylate (PMMA)[65] using emulsion polymerisation. The capsules were in the size of 10 nm-40 μm and showed good stability in thermal cycling.

Miniemulsion polymerisation

By miniemulsion polymerisation, tiny droplets containing PCM, monomer, and emulsifier are stabilised in reaction medium under high shear force with help of the ultrasonic sonicator. The polymerisation in the miniemulsion droplets is started by adding an initiator. The capsules finally formed is approximately the same size as the droplets formed in the first step. Miniemulsion is a popular method to form PCM nanocapsules, as the energy input is lower than traditional emulsion using mechanical stirring and the formed emulsion droplets are at smaller sizes and higher stability.

There are direct miniemulsion and inverse miniemulsion. The direct miniemulsion is an oil in water (o/w) system. The organic PCMs are dissolved in a small amount of organic solvent and form oil droplets dispersed in the water medium. The inverse miniemulsion is a water in oil (w/o) system. The inorganic PCMs that are soluble in water medium are dispersed in the organic reaction medium. Both organic and inorganic PCMs can be nano encapsulated using miniemulsion polymerisation. The common emulsifiers used are organic agents such as sodium dodecyl sulphate (SDS)[66], Span 20 (sorbitan monolaurate)[67], Span 85 (sorbitan trioleate)[68], Tween 80 (polyoxyethylene (20) sorbitan monooleate)[67], etc. The hydrophilic-lipophilic balance (HLB) value is used to measure the hydrophilicity or lipophilicity of the emulsifiers.

With a low HLB value, the emulsifier is more lipophilic and with a high HLB more hydrophilic. For w/o system, emulsifier with HLB from 3 to 6 is applied. For o/w system, the emulsifier should have an HLB from 8 to 16. Fang et al.[69][70] have fabricated polystyrene nanocapsules containing different alkanes as PCMs. The capsules were with the size around 150 nm.

Interfacial polymerisation

By interfacial polymerisation, the polymerisation develops on the interface of the two phases. First, the PCM as a core is emulsified to form an o/w or w/o emulsion with the help of the emulsifier. Then, the polymer shell is formed on the PCM core. The capsule fabricated is finally separated from the dispersing phase. As one variant of interfacial polymerisation, the solvent evaporation precipitation is applied to encapsulate inorganic PCMs[71]. The water phase with PCMs is emulsified in a non-volatile organic solvent with homogenizer or sonication in the presence of emulsifiers in the organic phase. When the small droplet size is reached, another volatile organic solvent containing one monomer is added under continuously stirring and slow stable increase of the temperature until the expected reaction temperature is reached. Then a small amount of the third non-volatile organic solvent containing the other monomer is added dropwise to start the polymerisation. The first monomer precipitate on the surface of water droplets as the volatile solvent gets evaporated, and it reacts with the second monomer in the non-volatile organic solvent to produce polymer shell on the interface. Park et al.[72] synthesised paraffin nanocapsules with polyurea shell by interfacial polycondensation.

In situ polymerisation

By in situ polymerisation, the monomer and emulsifier are dispersed outside the core in the continuous solvent. The prepolymer formed in the polymerisation process precipitates from the solvent and gradually generates the polymer shell on the surface of the PCM core droplet. Different from the emulsion polymerisation, in this technique, all the reactants to form the polymer shell are in the dispersion phase and the polymerisation occurs also in this phase. Nan et al.[73] synthesised n-octadecane nanocapsules with polymethyl methacrylate-co-allyl methacrylate via free radical and in situ polymerisation.

1.3.2 Inorganic shell encapsulation

The sol-gel technique is commonly applied to fabricate PCM micro/nano capsules with an inorganic shell. The first step is the dispersion of molecular precursors in a solvent. This is a stable colloidal solution and corresponds to the term sol. Then through the hydrolysis and condensation process, the colloidal particles aggregate to form a 3D gel network. This gel network corresponds to the term gel. Hydrogen bonding, Van der Waals force and covalent bonding can be the intermolecular force to bind the network. For the generation of silica shell, tetraethoxysilane (TEOS) as a usual silica precursor is dissolved in an alcohol solvent. It is first hydrolysed to silicate, then the condensation of the silicate molecules leads to a silica network as a gel. In this procedure, the predecessor should be well assembled around the core droplet in the beginning, and the hydrolysis should be rapid to ensure a uniform shell.

Latibari et al.[74] synthesised palmitic acid (PA) nanocapsules with silica shell via the sol-gel method. The nanocapsules showed a smooth surface, good chemical stability and good thermal properties. Hong et al.[75] encapsulated indium nanodroplets with silica by sol-gel. Both sodium silicate and tetraethoxysilane (TEOS) were applied as silica precursors.

1.4 Porous form-stable composite phase change materials

Porous form-stable composite PCMs are obtained by impregnation of liquid PCMs into porous matrices. The porous matrices should be with high pore volume and big surface area so that the loading efficiency of PCMs is ensured. Various porous materials such as metal foams[76]–[78], carbon nanotubes[79][80], graphene-based materials[81][82], expanded graphite[83]–[85], mesoporous silicas[86][87], porous polymers[88][89] and porous mineral materials[90]–[93] have been reported as supporting matrices for composite PCMs. Metal foams usually exhibit a big pore size of 0.1-5 mm, high thermal conductivity, and high mechanical strength. Aluminium, copper, nickel and stainless steel have been used as foam material to incorporate organic PCMs. Although the metal supports can increase the thermal conductivity of the PCMs, they have the disadvantages of high mass density, and the price is relatively high. Moreover, open and large pores are not favourite to prevent the leakage of PCMs. The cycling stability of the PCMs in the metal foam is seldom studied. Inorganic PCMs are generally not suitable to form composites with metal, as they are corrosive to most metals.

Carbon-based porous materials include carbon nanotubes (CNTs), graphene and expanded graphite. They all show high thermal conductivity. Carbon nanotubes are usually applied as thermal nanofillers to mix with organic PCMs. The increment of the thermal conductivity is limited because of interfacial thermal resistance[94]. Moreover, the market prices of carbon nanotubes are rather high with usually several hundred pounds per gram. Graphene consists of a single sp^2 bonded 2D carbon sheet. It has a hexagonal lattice structure of a honeycomb. Graphene and its derivatives such as graphene oxide and graphene aerogel exhibit high thermal conductivity and high surface area. They have been used as support for organic PCMs to obtain composites with increased thermal and electrical conductivity for the electric-thermal energy storage and conversion[95]. The large-scale fabrication of carbon nanotubes and graphene-based materials is limited due to the expensive precursors and complex fabrication equipment. Expanded graphite (EG) is obtained by intercalating graphite compounds under rapidly increased temperature. It has merits such as low density, large pore volume, and high thermal conductivity. It has been used as matrix for paraffin[96][97], fatty acids[98][99] and molten salts[100][101] to prepare form-stable composite PCMs. It is noticeable, the production of expanded graphite is associated with high energy consumption for the heating to high-temperature process.

Mesoporous silica can possess a controllable small pore size of 5-30 nm[102][103]. The organic PCMs were impregnated in the mesoporous silica, such as SBA-15 and MCM-41, whereby the melting and freezing temperature of the composite varies from the pure PCM as a result of nanoconfinement. Various researches studied the relationship between the phase change properties and the supporting mesoporous silica matrix properties, parameters such as interaction between PCM and supports[104], porosity and pore size of the supports[105], the chain length of the incorporated organic PCMs[106], etc. were elaborately investigated. It is unneglectable, that all the researches are based on organic PCMs. Inorganic PCMs have different molecular properties and phase change mechanisms, so the results concluded in the previous research on organic PCMs cannot be directly applied to inorganic PCMs.

Porous polymers have also been used to support PCMs. Epoxy resin[107], polyurethane[89], polyethylene[88] as well as some copolymers[108] are common porous polymer matrices for PCMs. The pore size[109], pore structures[110] and surface properties[111] of the polymer matrices can be modified to obtain form-stable composite PCMs with high adsorption ability and good thermal energy storage efficiency. But the polymer supports have the intrinsic disadvantages of low thermal conductivity, poor thermal stability, and poor chemical stability, also the production is usually associated with harmful reactants and solvents.

Porous mineral materials such as halloysite, bentonite, diatomite, sepiolite, etc. have the advantages of good porosity, good thermal stability, good chemical compatibility to building materials, relatively high thermal conductivity, low cost, abundant reserve in nature and no harm to the environment. The effective loading of PCMs in the porous mineral material is related to the different interactions, for example, surface tension, Van der Waal's force, capillary force, hydrogen bonding. Also because of these interactions, PCMs are stabilised in mineral support and the leakage of them is restrained. The common fabrication techniques of the form-stable PCMs with porous minerals include melting adsorption[112], vacuum impregnation[113], melting intercalation[114], etc. Comparing to the fabrication of other porous materials based form-stable PCMs, the matrices of minerals are usually ready to use without purification or modification, and the fabrication techniques are not complicated. Therefore, considering all the advantages of the porous mineral materials, they can be considered as the best candidate to support PCMs for the large scale industrial production and commercialization.

Porous mineral materials are various in aspects of porous structure and specific surface area. The minerals with small interlayer distance and specific surface area are not suitable as supports for PCMs. PCMs impregnated in the pore spacing of these minerals are retained by interactions between the PCMs and the pore structure such as capillary force, surface tension, etc. In this thesis, halloysite, diatomite, bentonite, and sepiolite were applied as porous mineral matrices.

1.5 Applications of phase change materials

Phase change materials using the latent heat storage principle can improve the utilisation efficiency and conversion rate of energy, solve the contradiction between energy supply and demand, and finally realize the reasonable utilisation of energy especially renewable energy. The research on their applications is very important. They have been used in various fields such as building, textile, industrial waste heat, solar energy and thermal fluid, as shown in Fig. 1-6.

Adding phase change materials in building materials can decrease the energy consumption on buildings, drop the temperature variation of the indoor environment and thus improve the thermal comfort. Griffiths et al.[115] incorporated a kind of commercial PCM microcapsules of 2-8 μm with the melting temperature at 18 ˚C in ceiling panels to achieve the chilling function. Various building materials including concrete[116], plaster[117] and insulating foam materials[118] have been added with PCM microcapsules. Castellon et al.[119] synthesised concrete containing PCM microcapsules. The mechanical strength of the compounded concrete was not reduced and reasonable energy was saved on the chamber cooling. Zhou et al.[120] fabricated montmorillonite form-stable paraffin PCM and added it into concrete to construct the walls. The heat diffusion from outside into the interior space was decreased and the thermal comfort was improved.

Textile is another important application for PCMs. Fabrics added with PCMs as capsules or form-stable composites show a regulated temperature and are regarded as smart textiles. Renzi et al.[121] fabricated PCM microcapsules with phase change temperature at 18 and 28 ˚C in the range of 5-40 μm and attached them to leather. The energy produced by the body could be better stored in the jacket with PCM microcapsules. Wang[122] used a mixture of fatty acids with the phase change temperature close to the human body temperature to fabricate expanded perlite form-stable PCM and applied this FSPCM in foam rubber to make wetsuit. It showed this wetsuit was proper for diving in water over 5 ˚C. It demonstrated good thermal insulation property. The temperature decrease slowed down when the FSPCM was added.

The industrial waste heat can be recycled by PCMs. Nomura[123] applied the eutectic mixture of Na_2CO_3 and NaOH to the transport system of waste heat. The system with PCMs required 9.5% energy, lost 39.5% effective energy and had 19.6% CO_2 emissions compared to the traditional system. Pandiyarajan et al.[124] added PCMs with a thermal energy storage capacity of 20 MJ to heat exchanger. 10-15 % of waste heat was recycled.

The application of PCMs can solve the instability and dispersibility of solar energy. Koca et al.[125] incorporated $CaCl_2{\cdot}6H_2O$ as PCM into plate solar collector. The energy efficiency increased by 2.2%. Xiao et al.[126] made polyethylene form-stable paraffin

PCM and added it to the floor. This floor can utilise the sunshine in the day time and maintained the room temperature over 18 ˚C.

PCM particles can be added to a continuous phase to obtain latent functional thermal fluid for heat transfer and storage. Wang et al.[127] fabricated slurry with water and microencapsulated 1-bromohexadecane. The heat transfer coefficients and thermal storage capacity increased as PCM microcapsules rose from 5% to 27.6%.

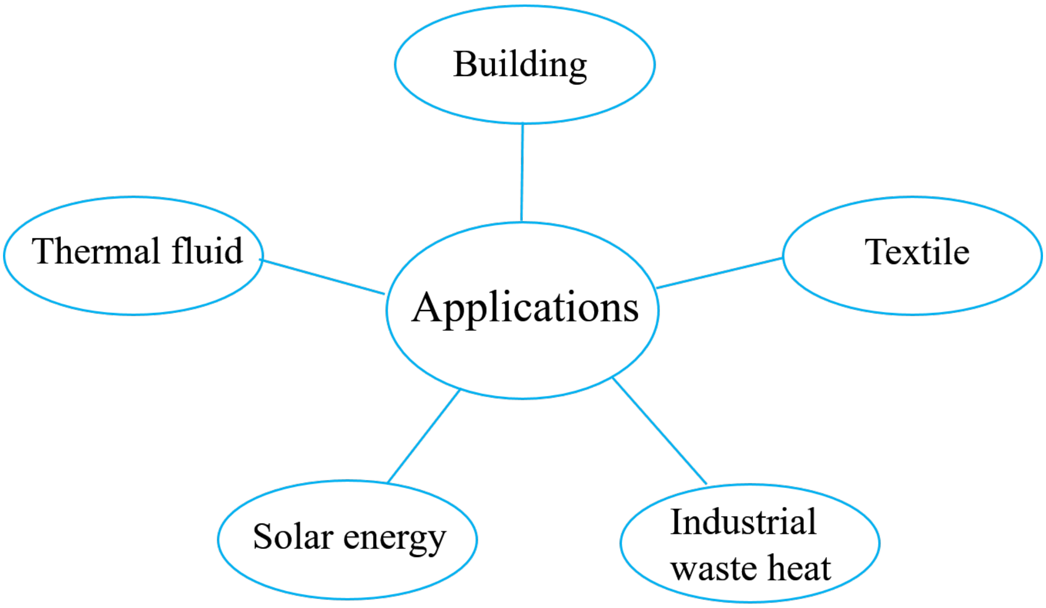

Fig. 1-6 Applications of phase change materials

1.6 Main contents of the thesis

This thesis tried to confine hydrated salts PCM with two strategies:

I. Fabrication of core-shell nanocapsules

II. Fabrication of form-stable PCMs with nanoporous minerals

The confinement should prevent leakage of hydrated salts PCM in the solid-liquid transformation. The compatibility of shell or matrix material to the container can overcome the corrosion problem of hydrated salts to metal. The phenomena of phase separation and supercooling should be mitigated as phase change transformation is confined in a small space. The small-sized capsules and porous supporting matrices function as small containers to hold the hydrated salts PCMs, which may prevent them from degradation over cycling. Further, special properties associated with nanosized

PCM particles and interaction between PCMs and nanocontainers need to be investigated.

Previous research on the fabrication of core-shell PCM capsules was usually about organic PCM microcapsules. Nanoencapsulation of hydrated salts has many challenges, such as the capsule size is hard to control to the nanosize, aggregation of nanoparticles could be observed, and the evaporation of hydrated water during the production of capsules may lead to the loss of the original phase change character. In my work, hydrated salts were tried to be nanoencapsulated with polymer and silica shells. The phase change properties of the samples were measured. And finally, the fabrication methods and results were evaluated.

On the fabrication of form-stable PCM (FSPCM), halloysite, bentonite, diatomite and sepiolite were applied to incorporate a mixture of $Na_2SO_4 \cdot 10H_2O$ and $Na_2HPO_4 \cdot 12H_2O$ as PCM. Usually, the porous mineral was mixed with organic PCM to form FSPCM. In this work, starting from the system halloysite form-stable hydrated salts PCM, the optimum composition of hydrated salts, the best fabrication parameters as well as the balance between loading ratio and cycling property were determined. Then, other FSPCMs with bentonite, diatomite and sepiolite were investigated. The morphology, phase change properties and in necessary cases cycling stability of the samples were characterised and discussed.

References

[1] M.H. Zalba B, Marin J.M, Cabeza L.F, *Appl. Therm. Eng.* **2003**, *23*, 251.

[2] O. Ellabban, H. Abu-Rub, F. Blaabjerg, *Renew. Sustain. Energy Rev.* **2014**, *39*, 748.

[3] *Intergovernmental Panel on Climate Change (IPCC), Climate Change 2014: Synthesis Report. Contribution of Working Groups I, II and III to the Fifth Assessment Report of the Intergovernmental Panel on Climate Change, IPCC*, Geneva **2014**.

[4] United Nations, *Conf. Parties, Twenty-First Sess.* **2015**, *21932*, 32.

[5] IRENA, *Global Energy Transformation: A Roadmap to 2050*, International Renewable Energy Agency Abu Dhabi **2018**.

[6] *BP Statistic Review of World Energy* **2019**.

[7] *Joint EASE-EERA recommendations for a european energy storage technology development roadmap towards 2030 - update* **2017**.

[8] A. Sharma, V. V. Tyagi, C.R. Chen, D. Buddhi, *Renew. Sustain. Energy Rev.* **2009**, *13*, 318.

[9] S.M. Hasnain, *Energy Convers. Manag.* **1998**, *39*, 1127.

[10] Z. Ling, Z. Zhang, G. Shi, X. Fang, L. Wang, X. Gao, Y. Fang, T. Xu, S. Wang, X. Liu, *Renew. Sustain. Energy Rev.* **2014**, *31*, 427.

[11] V. V. Tyagi, A.K. Pandey, D. Buddhi, R. Kothari, *Energy Build.* **2016**.

[12] T. Yan, R.Z. Wang, T.X. Li, L.W. Wang, I.T. Fred, *Renew. Sustain. Energy Rev.* **2015**, *43*, 13.

[13] P. Neveu, S. Tescari, D. Aussel, N. Mazet, *Energy Convers. Manag.* **2013**, *71*, 186.

[14] D. Aydin, S.P. Casey, S. Riffat, *Renew. Sustain. Energy Rev.* **2015**, *41*, 356.

[15] A. Abhat, *Sol. Energy* **1983**, *30*, 313.

[16] G. Jaeger, *Arch. Hist. Exact Sci.* **1998**, *53*, 51.

[17] a. Einstein, *Ann. d. Phys.* **1905**, *322*, 549.

[18] M. von Smoluchowski, *Ann. Phys.* **1906**, *326*, 756.

[19] A. Abhat, A.A. Short, R. De Physique, **1980**, *15*, 477.

[20] M.M. Farid, A.M. Khudhair, S.A.K. Razack, S. Al-Hallaj, *Energy Convers. Manag.* **2004**, *45*, 1597.

[21] S.S. Chandel, T. Agarwal, *Renew. Sustain. Energy Rev.* **2017**, *67*, 581.

[22] A. Sarı, A. Biçer, A. Karaipekli, C. Alkan, A. Karadag, *Sol. Energy Mater. Sol. Cells* **2010**, *94*, 1711.

[23] K. Pielichowski, K. Flejtuch, *Polym. Adv. Technol.* **2002**, *13*, 690.

[24] S.M. Hasnain, *Energy Convers. Manag.* **1998**, *39*, 1127.

[25] S. HIMRAN, A. SUWONO, G.A.L.I. MANSOORI, *Energy Sources* **1994**, *16*, 117.

[26] G.A. Lane, *Solar Heat Storage: Latent Heat Materials. Volume 1. Background and Scientific Principles*, CRC Press Inc. **1983**.

[27] W.R. Humphries, E.I. Griggs, *A Design Handbook for Phase Change Thermal Control and Energy Storage Devices*, United States **1977**.

[28] Z. Liu, D.D.L. Chung, *Thermochim. Acta* **2001**, *366*, 135.

[29] S.D. Sharma, K. Sagara, *Int J Green Energy* **2005**, *2*, 1.

[30] J. Morikawa, T. Hashimoto, *Thermochim. Acta* **2000**, *352*, 291.

[31] D.Q.M. Craig, J.M. Newton, *Int. J. Pharm.* **1991**, *74*, 33.

[32] D. Rozanna, T.G. Chuah, A. Salmiah, T.S.Y. Choong, M. Sa'ari, *Int. J. Green Energy* **2005**, *1*, 495.

[33] J.Q. Sun, R.Y. Zhang, Z.P. Liu, G.H. Lu, *Energy Convers. Manag.* **2007**, *48*, 619.

[34] M. Liu, W. Saman, F. Bruno, *Renew. Sustain. Energy Rev.* **2012**, *16*, 2118.

[35] I. Dincer, M.A. Rosen, *Thermal Energy Storage, Systems and Applications*, John Wiley & Sons, New York **2002**.

[36] G. Belton, F. Ajami, *Thermochemistry of Salt Hydrates*, Pennsylvania University, Philadelphia **1973**.

[37] R. Naumann, H.H. Emons, *J. Therm. Anal.* **1989**, *35*, 1009.

[38] G.A. Lane, *Int. J. Ambient Energy* **1980**, *1*, 155.

[39] D.W. Hawes, D. Feldman, D. Banu, *Energy Build.* **1993**, *20*, 77.

[40] H.W. Ryu, S.W. Woo, B.C. Shin, S.D. Kim, *Sol. Energy Mater. Sol. Cells* **1992**, *27*, 161.

[41] N. Xie, Z. Huang, Z. Luo, X. Gao, Y. Fang, Z. Zhang, *Appl. Sci.* **2017**, *7*, 1317.

[42] G. Feng, X. Xu, N. He, H. Li, K. Huang, *Mater. Res. Innov.* **2015**, *19*, S5.

[43] X. Wu, Y. Wang, R. Sun, M. Lai, R. Du, Z. Zhang, *J. Phys. Conf. Ser.* **2009**, *188*, 12046.

[44] I.M. Sutjahja, S.R.A. U, N. Kurniati, I.D. Pallitine, D. Kurnia, *J. Phys. Conf. Ser.* **2016**, *739*, 12064.

[45] M.E. Zayed, J. Zhao, A.H. Elsheikh, F.A. Hammad, L. Ma, Y. Du, A.E. Kabeel, S.M. Shalaby, *Sol. Energy Mater. Sol. Cells* **2019**, *199*, 24.

[46] M.M. Kenisarin, *Renew. Sustain. Energy Rev.* **2010**, *14*, 955.

[47] J. Lopez, Z. Acem, E.P. Del Barrio, *Appl. Therm. Eng.* **2010**, *30*, 1586.

[48] L. Zhong, X. Zhang, Y. Luan, G. Wang, Y. Feng, D. Feng, *Sol. Energy* **2014**, *107*, 63.

[49] J. Xiao, J. Huang, P. Zhu, C. Wang, X. Li, *Thermochim Acta* **2014**, *587*.

[50] J.P. Kotzé, T.W. von Backström, P.J. Erens, *Energy Procedia* **2014**, *49*, 860.

[51] R. Fukahori, T. Nomura, C. Zhu, N. Sheng, N. Okinaka, T. Akiyama, *Appl. Energy* **2016**, *163*, 1.

[52] J.P. Kotzé, T.W. von Backström, P.J. Erens, *J. Sol. Energy Eng.* **2013**, *135*, 035001.

[53] H. Ge, H. Li, S. Mei, J. Liu, *Renew. Sustain. Energy Rev.* **2013**, *21*, 331.

[54] D.G. Archer, *J. Chem. Eng. Data* **2002**, *47*, 304.

[55] R. Wei, C., Jianzeng, G., Xiaohong, Z. and Xiaoming, *High Power Laser Part. Beams* **2009**, *8*, 1170.

[56] H. Ge, J. Liu, *Front. Energy* **2012**, *6*, 207.

[57] H. Ge, J. Liu, *J. Heat Transfer* **2013**, *135,* 054503.

[58] J. Liu, Y.-G. Deng, Z.-S. Deng, **2010**, *4*, 161.

[59] M.-L. De Temmerman, J. Demeester, S.C. De Smedt, J. Rejman, *Nanomedicine* **2012**, *7*, 771.

[60] M. Delcea, A. Yashchenok, K. Videnova, O. Kreft, H. Möhwald, A.G. Skirtach, *Macromol. Biosci.* **2010**, *10*, 465.

[61] X. Gao, Q. Ma, T. Zhao, J. Bao, N. Tsubaki, *Chinese J. Chem. Phys.* **2018**, *31*, 393.

[62] F. Cuomo, A. Ceglie, A. De Leonardis, F. Lopez, *Catalysts* **2018**, *9*, 1.

[63] J. Sun, Y. Wang, N. Li, L. Tian, *Tribol. Int.* **2019**, *136*, 332.

[64] A. Sarı, C. Alkan, D.K. Döğüşçü, A. Biçer, *Sol. Energy Mater. Sol. Cells* **2014**, *126*, 42.

[65] A. Sarı, C. Alkan, A. Biçer, A. Altuntaş, C. Bilgin, *Energy Convers. Manag.* **2014**, *86*, 614.

[66] M.D. Besteti, A.G. Cunha, D.M.G. Freire, J.C. Pinto, *Macromol. Mater. Eng.* **2014**, *299*, 135.

[67] M. Graham, E. Shchukina, P.F. De Castro, D. Shchukin, *J. Mater. Chem. A* **2016**, *4*, 16906.

[68] A.S. Chaurasia, S. Sajjadi, *Chem. Eng. Sci.* **2015**, *129*, 260.

[69] Y. Fang, X. Liu, X. Liang, H. Liu, X. Gao, Z. Zhang, *Appl. Energy* **2014**, *132*, 551.

[70] Y. Fang, H. Yu, W. Wan, X. Gao, Z. Zhang, *Energy Convers. Manag.* **2013**, *76*,

430.

[71] S. Freitas, H.P. Merkle, B. Gander, *J. Control. Release* **2005**, *102*, 313.

[72] S.H. Park, *Appl. Math. Lett.* **2014**, *31*, 46.

[73] G.-H. Nan, J.-P. Wang, Y. Wang, H. Wang, W. Li, X.-X. Zhang, *Wuli Huaxue Xuebao/ Acta Phys. - Chim. Sin.* **2014**, *30*, 338.

[74] S.T. Latibari, M. Mehrali, M. Mehrali, T.M.I. Mahlia, H.S.C. Metselaar, *Energy* **2013**, *61*, 664.

[75] Y. Hong, W. Wu, J. Hu, M. Zhang, A.A. Voevodin, L. Chow, M. Su, *Chem. Phys. Lett.* **2011**, *504*, 180.

[76] X. Xiao, P. Zhang, M. Li, *Int. J. Therm. Sci.* **2014**, *81*, 94.

[77] F. Zhu, C. Zhang, X. Gong, *Appl. Therm. Eng.* **2016**, *109*, 373.

[78] P. Zhang, Z.N. Meng, H. Zhu, Y.L. Wang, S.P. Peng, *Appl. Energy* **2017**, *185*, 1971.

[79] D.J. Yang, Q. Zhang, G. Chen, S.F. Yoon, J. Ahn, S.G. Wang, Q. Zhou, Q. Wang, J.Q. Li, *Phys. Rev. B* **2002**, *66*, 165440.

[80] J. Che, T. Çagin, W.A. Goddard, *Nanotechnology* **2000**, *11*, 65.

[81] M. Mehrali, S.T. Latibari, M. Mehrali, T.M.I. Mahlia, H.S.C. Metselaar, *Energy* **2013**, *58*, 628.

[82] G. Li, X. Zhang, J. Wang, J. Fang, *J. Mater. Chem. A* **2016**, *4*, 17042.

[83] W. Wang, X. Yang, Y. Fang, J. Ding, J. Yan, *Appl. Energy* **2009**, *86*, 1479.

[84] Y. Cai, C. Gao, T. Zhang, Z. Zhang, Q. Wei, J. Du, Y. Hu, L. Song, *Renew. Energy* **2013**, *57*, 163.

[85] D. Kim, J. Jung, Y. Kim, M. Lee, J. Seo, S.B. Khan, *Int. J. Heat Mass Transf.* **2016**, *95*, 735.

[86] J. Zhang, Y. Feng, H. Yuan, D. Feng, X. Zhang, G. Wang, *Comput. Mater. Sci.* **2015**, *109*, 300.

[87] T. Nomura, C. Zhu, N. Sheng, K. Tabuchi, A. Sagara, T. Akiyama, *Sol. Energy*

Mater. Sol. Cells **2015**, *143*, 424.

[88] X. Huang, G. Alva, L. Liu, G. Fang, *Appl. Energy* **2017**, *200*, 19.

[89] B. Tang, L. Wang, Y. Xu, J. Xiu, S. Zhang, *Sol. Energy Mater. Sol. Cells* **2016**, *144*, 1.

[90] T. Nomura, N. Okinaka, T. Akiyama, *Mater. Chem. Phys.* **2009**, *115*, 846.

[91] M. Li, Z. Wu, H. Kao, J. Tan, *Energy Convers. Manag.* **2011**, *52*, 3275.

[92] C.-M. Li, Y. Liu, *Adv. Mater. Res.* **2013**, *718*, 1908.

[93] X. Li, J.G. Sanjayan, J.L. Wilson, *Energy Build.* **2014**, *76*, 284.

[94] R.J. Warzoha, A.S. Fleischer, *Nano Energy* **2014**, *6*, 137.

[95] Z. Chen, W. Ren, L. Gao, B. Liu, S. Pei, H.-M. Cheng, *Nat. Mater.* **2011**, *10*, 424.

[96] Z. Zhang, X. Fang, *Energy Convers. Manag.* **2006**, *47*, 303.

[97] A. Sarı, A. Karaipekli, *Appl. Therm. Eng.* **2007**, *27*, 1271.

[98] S. Wang, P. Qin, X. Fang, Z. Zhang, S. Wang, X. Liu, *Sol. Energy* **2014**, *99*, 283.

[99] Y. Li, H. Yan, Q. Wang, H. Wang, Y. Huang, *J. Therm. Anal. Calorim.* **2017**, *128*, 1313.

[100] P. Zhang, F. Ma, X. Xiao, *Appl. Energy* **2016**, *173*, 255.

[101] X. Xiao, P. Zhang, M. Li, *Energy Convers. Manag.* **2015**, *105*, 272.

[102] J.S. Beck, J.C. Vartuli, W.J. Roth, M.E. Leonowicz, C.T. Kresge, K.D. Schmitt, C.T.W. Chu, D.H. Olson, E.W. Sheppard, S.B. McCullen, J.B. Higgins, J.L. Schlenker, *J. Am. Chem. Soc.* **1992**, *114*, 10834.

[103] D. Zhao, J. Feng, Q. Huo, N. Melosh, G.H. Fredrickson, B.F. Chmelka, G.D. Stucky, *Science* **1998**, *279*, 548.

[104] D. Zhang, S. Tian, D. Xiao, *Sol. Energy* **2007**, *81*, 653.

[105] L.P. Wang, J. Sui, M. Zhai, F. Tian, X.Z. Lan, *J. Phys. Chem. C* **2015**, *119*, 18697.

[106] X. Yan, C. Gao, T. Wang, L. Wang, X. Lan, *RSC Adv.* **2013**, *3*, 18028.

[107] Q. Lian, K. Li, A.A.S. Sayyed, J. Cheng, J. Zhang, *J. Mater. Chem. A* **2017**, *5*, 14562.

[108] A. Sarı, C. Alkan, A. Biçer, *Mater. Chem. Phys.* **2012**, *133*, 87.

[109] W. Liang, G. Zhang, H. Sun, Z. Zhu, A. Li, *RSC Adv.* **2013**, *3*, 18022.

[110] J. Tang, M. Yang, F. Yu, X. Chen, L. Tan, G. Wang, *Appl. Energy* **2017**, *187*, 514.

[111] J. Tang, S. Fan, W. Dong, J. Wang, H. Gao, M. Yang, M. Yang, G. Wang, *RSC Adv.* **2016**, *6*, 44807.

[112] J.H. Deng, W.B. Li, D.H. Jiang, in *Sustain. Dev. Urban Environ. Build. Mater.*, Trans Tech Publications Ltd **2012**, 807.

[113] S. Liu, H. Yang, *Energy Technol.* **2015**, *3*, 77.

[114] Q. Ying, W. Qisheng, L. Shuiping, *J. Mater. Sci. Eng.* **2013**, *2*, 268.

[115] P.W. Griffiths, P.C. Eames, *Appl. Therm. Eng.* **2007**, *27*, 1756.

[116] M. Pomianowski, P. Heiselberg, R.L. Jensen, R. Cheng, Y. Zhang, *Cem. Concr. Res.* **2014**, *55*, 22.

[117] A.M. Borreguero, I. Garrido, J.L. Valverde, J.F. Rodríguez, M. Carmona, *Energy Build.* **2014**, *76*, 631.

[118] A.M. Borreguero, J.F. Rodríguez, J.L. Valverde, T. Peijs, M. Carmona, *J. Appl. Polym. Sci.* **2013**, *128*, 582.

[119] C. Castellón, A. Castell, M. Medrano, I. Martorell, L.F. Cabeza, *J. Sol. Energy Eng.* **2009**, *131*.

[120] Z. Dunbai, H. Rui, Z. Zhihao, J. Deming, *Energy Technol.* **2009**, *2*, 102.

[121] A.I. Renzi, C. Carfagna, P. Persico, *Appl. Therm. Eng.* **2010**, *30*, 1369.

[122] W. Zheng, *Preparation and Study on Properties of Insulating Wetsuit with Fatty Acid/Expanded Perlite Composite PCM*, **2013**.

[123] T. Nomura, T. Oya, N. Okinaka, T. Akiyama, *ISIJ Int.* **2010**, *50*, 1326.

[124] V. Pandiyarajan, M.C. Pandian, E. Malan, R. Velraj, R. V Seeniraj, *Appl. Energy* **2011**, *88*, 77.

[125] A. Koca, H.F. Oztop, T. Koyun, Y. Varol, *Renew. Energy* **2008**, *33*, 567.

[126] X. Wei, W. Xin, Z. Qunli, *Acta Energlae Solaris Sin.* **2008**, *29*, 1319.

[127] X. Wang, J. Niu, Y. Li, X. Wang, B. Chen, R. Zeng, Q. Song, Y. Zhang, *Int. J. Heat Mass Transf.* **2007**, *50*, 2480.

2. Characterisation techniques

2.1 Differential scanning calorimetry

As a thermal analysis technique, differential scanning calorimetry (DSC) records the difference in the heat needed between a sample and the reference as temperature linearly increases with time[1]. The temperature of the sample and the reference is kept the same in the whole measuring process.

Heat flux DSC is the most common type of DSC instrument and is applied in the thesis. Its construction is shown in Fig. 2-1. The instrument comprises the heating block, the thermoelectric disc, the sample and the reference holders as well as the thermocouples in one closed chamber. The heat from the heating block is transferred via the constantan thermoelectric disc to the reference and the sample pan on the respective holder. The thermocouples made of alumel and chromel wires are used to measure the temperature of the sample and the reference independently. Different heat amount is supplied instantly to compensate the temperature difference between the two holders.

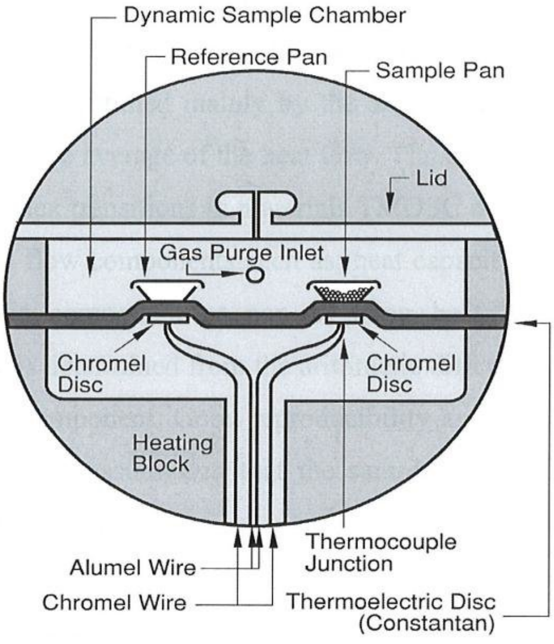

Fig. 2-1 Construction of heat flux DSC (Source:[2])

From the DSC plot the phase change enthalpy and the phase transition temperature can be quantitatively determined. In case of melting, an endothermic peak is detected with the integrated peak area as melting enthalpy and the peak point as melting temperature. For crystallisation, an exothermic peak is found with the peak area as freezing enthalpy and the peak point as freezing temperature. To obtain comparable experimental data, instrumental factors such as heating rate, purge gas inlet rate, types of pans applied must be kept consistent.

2.2 Gas physisorption

Gas physisorption is a characterisation method to get information on the specific surface area, pore volume and pore size distribution of solid material[3]. The Van der Waals interaction between gas molecules and solid leads to plots of equilibrium isotherms, showing the change of absorbed amount of gas molecules versus the relative pressure. Nitrogen, argon and carbon dioxide can be applied as gas sources for this technique. Nitrogen is used in this thesis due to its cheap price, high purity, good accessibility to solid material and inert characteristics.

One of the widely accepted mechanisms to explain the physical adsorption of gas molecules on a solid surface is the Brunauer-Emmett-Teller theory (BET). It extends the monolayer molecular adsorption described by the Langmuir theory to the multilayer adsorption. This theory[4]–[6] assumes that the sample has homogeneous surface and all surface sites have same adsorption energy for adsorbate. Each adsorbate molecule interacts only vertically with other molecules, while the lateral interactions are neglected. Each layer shows the same adsorption behaviour. This theory can be applied to estimate the pore volume and the specific surface area of solid material from the equilibrium adsorption isotherm measured at the boiling point of the gas adsorbate (77 K for nitrogen).

The Barett-Joyner-Halenda theory (BJH) is a common method to calculate pore size distribution of solid based on the equilibrium desorption isotherm. This theory[7] assumes all the pores are cylindrical, and the adsorbates are physically adsorbed on pore walls as well as capillary condensated in mesopores. This method is incorrect to determine micropores with size smaller than 2 nm due to the restrictive assumptions and the neglect of physical effects such as tensile strength and pore network effects[8][9].

The gas physisorption procedure consists of the degassing and adsorption steps. In the degassing step, the measurement cell is first calibrated by evacuation and running one adsorption cycle. Then, the sample is loaded to the cell, which is connected to the degassing station of the apparatus. Physically adsorbed impurities such as water and volatiles should be removed from the solid sample during degassing. In this step, the degassing temperature and time should be enough but not exceeded, as morphology of material could be changed. In the following adsorption step, the cell is switched to the adsorption station. After evacuation, the adsorbate gas is introduced incrementally in the adsorption cycle. The adsorbed amount of gas is calculated by the difference in pressure from the measurement cell and the empty reference cell. During measurement of adsorption and desorption isotherms, the cells are maintained at 77 K by immersing in liquid nitrogen.

The nitrogen physisorption isotherms are commonly classified in six types, as shown in Fig. 2-2(a). Type I isotherms represent materials with micropores. The pores are filled at low relative pressure fast due to the adsorbent-adsorbate interactions[10]. As the micropore volume is limited, no further adsorption is observed at higher relative pressure. Type II isotherms are for nonporous or macroporous materials. The adsorbate molecules are adsorbed first in monolayer, then in multilayers. Point B is the transition point from monolayer to multilayer adsorption. Type III isotherms indicate the interactions between adsorbate and adsorbent surface are weaker than those between adsorbate layers. Type IV isotherms are typical for micro- and mesoporous materials. The hysteresis loop between the adsorption and desorption isotherm is caused by the capillary condensation in mesopores. Type V isotherms exhibit the initial zero slope similar to type III and the hysteresis loop indicates the existence of micro- and mesopores. Type VI isotherms shows stepwise multilayer adsorption on nonporous materials.

The types of hysteresis loops (Fig. 2-2 (b)) give information on the pore shape[11]. H1 loop, which comprises the adsorption and desorption isotherms both in vertical course and starts at high relative pressure, is associated with well-defined spherical and cylindrical mesopores. H2 loop with delayed fast release of adsorbate in the desorption isotherm indicates pore blocking, which is often found in ink bottle-shaped pores and interconnected networks of pores. H3 loop starts at low relative pressure and is often observed for non-rigid aggregated plate-like particles. H4 loop with isotherms in nearly horizontal course is common for microporous surfaces with narrow slit pores. The dashed lines show hysteresis could be observed at low relative pressure for some microporous materials. The reasons could be swelling of non-rigid pores or chemisorption.

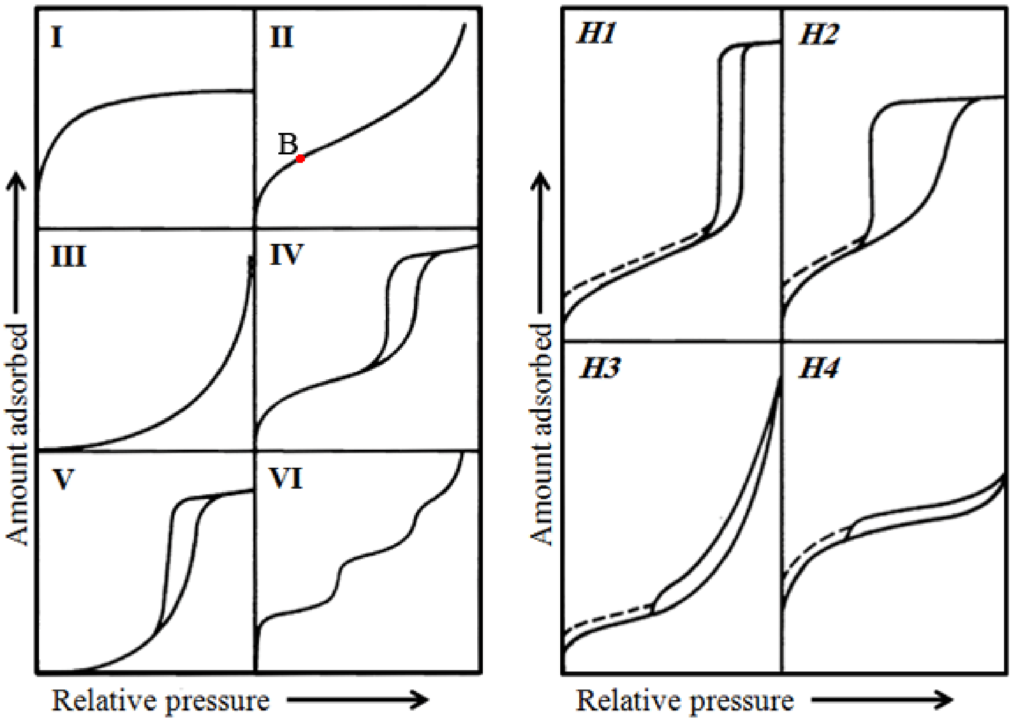

(a) (b)

Fig. 2-2 (a) Types of isotherms (b) types of hysteresis loops by nitrogen physisorption (Source:[4])

2.3 Scanning electron microscopy

Scanning electron microscopy (SEM) is a type of electron microscopy applying an electron beam to raster scan the surface of a sample and producing images with the magnification up to 500,000 times and the lateral resolution down to 1 nm[12][13]. The electron beam interacts with the atoms on the surface and particles such as electrons, x-rays and photons are emitted, producing signals for the image.

Depending on the types of emitted particles (Fig. 2-3), various imaging modes are available by SEM[12][14]. Secondary electron image is the most common mode generated by secondary electrons escaped from the shallow area of the surface and give information on surface topography. Backscattered electron image is generated by backscattered electrons from a slightly deep surface area. Comparing to the secondary electrons, backscattered electrons give a larger signal, leading to a lower resolution for the image. However, this mode is useful to determine the composition, as elements of higher atomic mass produce more backscattered electron signals and show brighter contrast. The X-rays are emitted when electrons jump from an outer atom orbit to an inner empty orbit. The energy dispersive X-ray spectrometer is applied to detect the X-rays, giving qualitative information on chemical composition from energies of the X-rays.

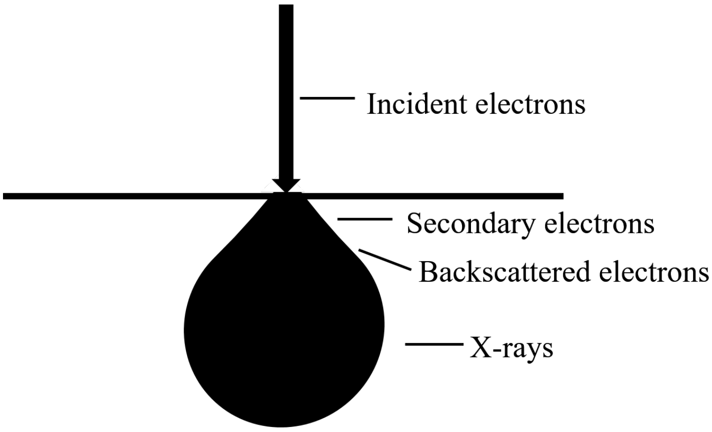

Fig. 2-3: Regions of emitted particles by SEM

The basic optic components of SEM microscope[12][14] include the electron source, the condenser lenses, the objective lenses, scan coils, and the detectors (Fig. 2-4). The electron gun emits electrons with energies of 5-40 keV in vacuum of 0.1-10^{-4} Pa[14]. The electromagnetic lenses demagnify the electrons into a fine beam, and move the beam across a chosen surface area in a raster mode with help of scan coils. Secondary electron detector, backscattered electron detector and X-ray detector are available to detect various particles emitted from the sample to generate SEM images.

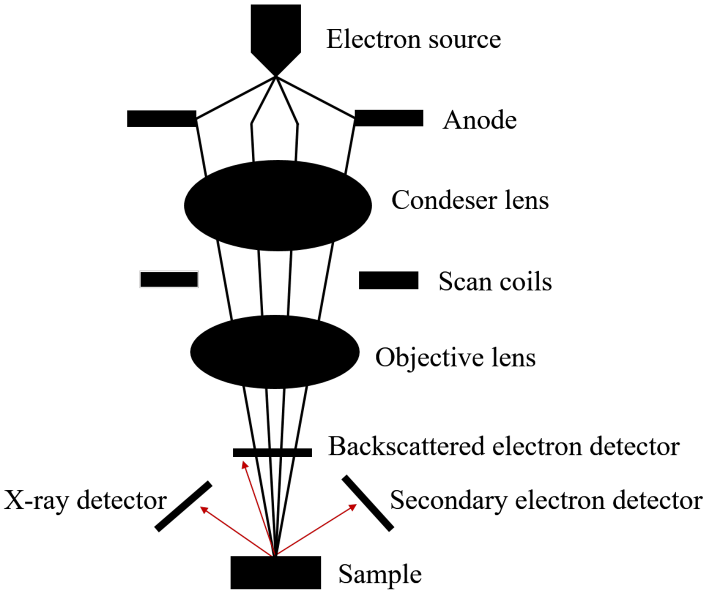

Fig. 2-4 Basic construction of SEM microscope

During the sample preparation for SEM, the contamination on the surface must be avoided. A sealed box is used to store and transport the samples. Samples with poor conductivity need an ultrathin coating to conduct away electrostatic charges which may accumulated on the surface. Gold and chromium are the common coating materials.

2.4 Transmission electron microscopy

By the transmission electron microscopy (TEM) an electron beam is transmitted through an ultrathin sample. The interaction between the electrons and the sample produces an image, which is then magnified and projected onto an imaging device[15][16]. The TEM images can reach a high magnification up to 1,000,000 times and a lateral resolution of 100 pm[16].

The basic optic components of TEM microscope[16] include the electron source, various lenses as optics and the fluorescent screen for imaging (Fig. 2-5). For the emission of electrons, an electron gun made of tungsten or lanthanum hexaboride is connected to 80-300 kV accelerating voltage[15], so the accelerated electrons have enough energy to penetrate material of 1 µm. For protecting light elements from damaging, a lower voltage of about 100 kV could be considered. Otherwise, 200-300 kV is the routine working voltage. The lenses by TEM are more complicated than in SEM. Condenser lenses focus the accelerated electrons as a beam to the sample. The electrons pass through the sample and are focused by objective lens. After transmitting objective aperture and further objective lens, the diffraction pattern is formed. Projector lens further magnifies the pattern, which is monitored by a fluorescent screen in the end. Charged coupled devices (CCD) as digital electron detection systems are usually attached to modern TEM microscopes, so the incoming electrons can be converted into an electronic pulse per pixel.

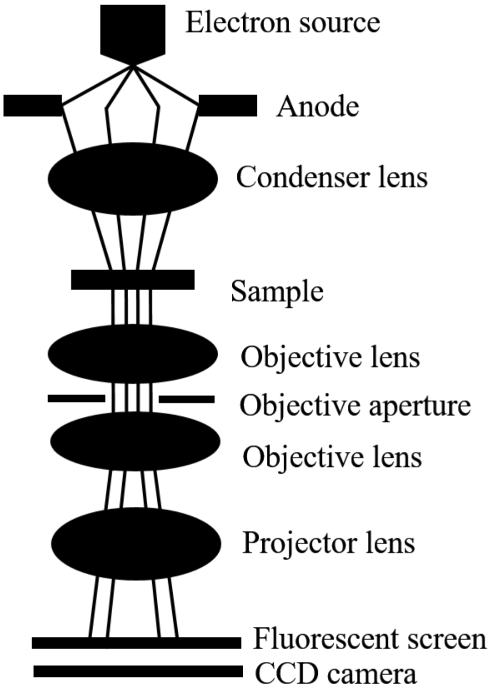

Fig. 2-5 Basic construction of TEM microscope

The sample preparation for TEM depends on the material properties and the desired information. Materials such as inorganic nanopowders have enough small size to be electron transparent. They can be made dilute suspension and deposited onto a support grid. For specimen with larger sizes in micrometre and millimetre ranges, or in size of several hundred nanometre but containing heavy elements, a destructive sample preparation is required to obtain a thin section. Controlled fracture, mechanical abrasion, ion sputtering, chemical etching and electrochemical dissolution have been reported as thinning techniques[17][18]. The cleanliness of sample must be kept well during the sample preparation and storage before measurement, as images of sub-nm resolution are desired by TEM.

2.5 X-Ray powder diffraction

X-ray powder diffraction (XRD) is an analytical technique using an X-ray beam to irradiate a sample and generate a diffraction pattern, which reflects the crystal structure of the sample. The fundamental principle is Bragg's law[19] as:

$$n\lambda = 2d\sin\Theta \qquad \text{(Eq. 2-1)}$$

n: integer order; λ: wavelength of incident X-ray; d: atomic planar spacing of crystal lattice; Θ: angle of incident X-ray

Bragg's Law can be understood as illustrated in Fig. 2-6. A monochromatic X-ray beam with a fixed wavelength λ hits onto the sample atomic planes. At a certain incident angle Θ, the scattered X-rays interfere constructively and an intense diffracted beam is detected to leave the lattice planes at the same angle Θ as the incident beam. The wavelength λ, the incident angle Θ and the material lattice planar spacing d have to fulfil the relationship described by Bragg's law, so the constructive interference can happen. By detecting the angles of diffracted X-rays, the d spacings can be recognized, which allows phase identification of the crystalline sample. By scanning the sample through a range of 2Θ angles, a set of d spacings is obtained as characteristics for each sample. The identification of an unknown crystalline material can be achieved by comparing the d spacings with standard reference patterns.

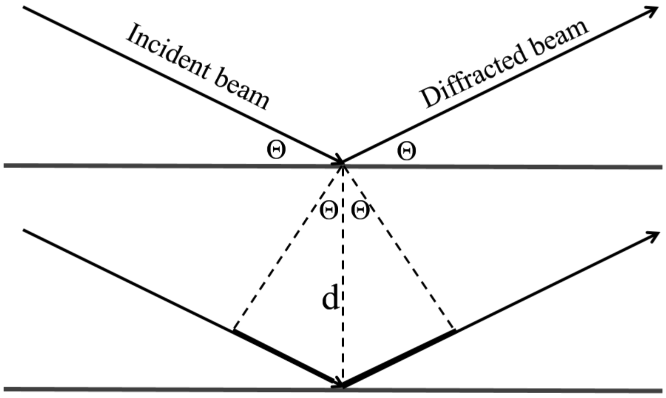

Fig. 2-6. Bragg's law

In the X-ray diffractometer, the incident X-rays are first generated in a cathode ray tube. Accelerated electrons with high energy bombard the target material, leading to expel of inner shell electrons of the target material, so a series of characteristic X-rays including K_α and K_β are produced. Copper is the common target material for single crystal diffraction. A crystal monochrometer is applied to filter the polychromatic X-rays. After the filtration, CuK_α with the wavelength of 1.5418 Å is collimated to the sample. During the measurement, the sample is rotated at an angle of Θ and the detector is rotated at 2Θ. The diffracted X-ray signals from various 2Θ angles with different intensities are recorded to generate the diffraction pattern of the sample.

The sample for X-ray powder diffraction measurement should be ground to homogeneous and fine powder. A powder size of less than 10 µm is preferred. The sample amount required for one measurement is relative big with several hundred milligrams. The substrate to hold the sample should be amorphous. The upper surface of the sample should be kept flat to randomize crystal lattice orientations. The advantages of XRD technique are simple sample preparation, wide availability of the instrument, fast measurement process with high sensitivity and accuracy and straightforward data interpretation.

2.6 Fourier transform infrared spectroscopy

Infrared spectroscopy (IR) applies infrared light to interact with material, and detects the molecular vibrations from the absorption bands of the light to resolve the chemical functional groups[20]. Fourier transform infrared spectroscopy (FTIR) is the commonly accepted method to obtain a wide range of spectrum data at one time[21].

A mode of molecular vibration can absorb infrared light (infrared active) only when the molecule dipole moment changes during the vibration. According to the movement type, the vibrations can be classified as stretching vibrations and bending vibrations. The stretching vibrations are vibrations along chemical bonds. The bending vibrations on the other hand show changes in bond angles, and include in plane and out of plane bending. The stretching vibrations can be modelled by the harmonic oscillator model (Fig. 2-7), whereby the spring represents the chemical bond and the connected two point masses represent the atom masses linked to the bond. The bond strength is the spring tenseness k.

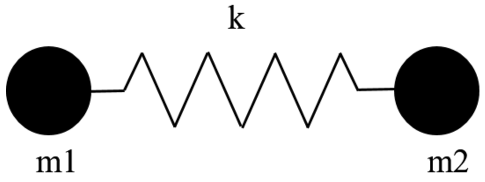

Fig. 2-7 Harmonic oscillator model for molecular stretching vibration

From the eq. 2-2 it is obvious, the stretching vibration frequency is related to the mass of atoms and the strength of the chemical bond. The FTIR spectra in the mid-IR region (4000-400 cm^{-1}), whereby most organic and inorganic groups are tested, can be generally classified into four ranges: single bond (O-H, C-H and N-H) in 4000-2500 cm^{-1}, triple bond (C≡C, C≡N, X=C=Y (C, O, N, S)) in 2500-2000 cm^{-1}, double bond (C=O, C=N, C=C, N=O) in 2000-1500 cm^{-1} and fingerprint region below 1500 cm^{-1} to characterise the whole molecules.

$$v = (1/2\pi c)\sqrt{k\,(m1 + m2)/m1m2} \qquad \text{(Eq. 2-2)}$$

v: frequency of vibration (cm^{-1}), c: speed of light ($cm{\cdot}s^{-1}$), k: bond strength ($dyne{\cdot}cm^{-1}$) m1, m2: atom mass 1, 2

The main components of FTIR spectrometer[22] include an IR source, interferometer, sample compartment, detector and Fourier transform computer software. A silicon carbide at 1200 K similar as a black body is applied to emit infrared light for the mid-IR region. The Michelson interferometer is the main difference between FTIR spectrometer and dispersive IR spectrometer. Beams with different path lengths are recombined in the interferometer and create an interferogram with constructive and destructive interference. Then the beams pass through the sample in sample compartment, whereby specific frequencies of energy are absorbed. The transmitted interferogram signals are measured by the detector for all frequencies simultaneously. Finally, the interferogram is transformed to the sample IR spectrum by Fourier transform computer software.

The sample preparation for the traditional direct transmission measurement is to press pellets. A tiny amount of powder sample (1% of the KBr amount) is mixed with the dried KBr powder and carefully ground into homogeneous fine powder. With the press tool, thin and transparent KBr pellets should be obtained for the measurement. It could easily fail to prepare a proper KBr pellet in practice. A too thin pellet tends to fragmentize in the sample holder. A too thick and opaque pellet hinders the transmission of IR beam. White spots are often found in a pellet if the powder is not ground and dispersed well enough. With help of the attenuated total reflection (ATR) accessory, the press of pellets is eliminated. A sample is put into direct contact with the ATR crystal in its natural state. The surface of the crystal can be easily cleaned and ready for the next measurement. The ATR-FTIR technique is with high sensibility[22]. The ATR crystal as the main component is made of materials with high refractive index such as diamond and germanium. The sample absorbs energy from evanescent wave out of internal reflectances of IR beam in crystal, so the evanescent wave is attenuated and then reflected back to the crystal. In the end side of the crystal all the reflected attenuated waves are detected. The ATR-FTIR is widely applied to analyse materials such as natural powder, coating and plastics. Excellent IR spectra can be obtained by this technique.

2.7 Raman spectroscopy

Raman spectroscopy is based on Raman scattering of incident light to determine the chemical structure of a sample[23][24]. When a light beam interacts with the sample, it can be elastically scattered (Rayleigh scattering) or inelastically scattered (Raman scattering). The scattered photon can have lower (Stokes Raman scattering) or higher (anti-Stokes Raman scattering) energy than the incident photon. By detecting the energy shift the molecule vibration modes can be determined to resolve the structural information.

Some molecules are Raman inactive. Generally, molecules with inversion symmetry can be either Raman active or optically active[23]. This rule of mutual exclusion is especially applicable by linear molecules and relaxed by nonlinear molecules. As the spontaneous Raman scattering is a very weak process, monochromatic laser light with narrow beam and high intensity is preferred as the incident light source. The common applied wavelengths of laser source are 785 nm and 532 nm. A longer wavelength generates a lower Raman signal intensity and requires longer acquisition time. However, it reduces photoluminescence in organic molecules so the Raman peaks are not masked.

The wavelength range of 500-830 nm is suitable for inorganic materials and most organic materials[25]. Only materials with strong fluorescence requires the wavelength of 1064 nm[25]. In practice, the laser light is not purely monochromatic but with a narrow spectrum of wavelengths called a linewidth. A narrow linewidth of laser source limits the shift of Raman peaks. Long integration times and repeated acquisitions are often needed to get Raman spectra with good quality. During the long measuring time, the laser source must be kept stable in wavelength and power.

The filter system is needed to block Raman signals generated from the transporting optical fibres. It is also applied to inhibit the laser light from entering the spectrometer, as it may generate Raman scatterings in the device.

The spectrometer is the key component to measure Raman spectra, whereby the spectral range and resolution can be chosen. The spectral range depends on the position of the Raman peaks to be researched. A high spectral resolution is needed to resolve closely packed Raman peaks.

References

[1] E. Freire, in *Methods Mol. Biol.*, Humana Press **1995**, 191.

[2] G. Höhne, W. F. Hemminger, H. J. Flammersheim, *Differential Scanning Calorimetry*, Springer **2003**.

[3] A. Peigney, C. Laurent, E. Flahaut, R.R. Bacsa, A. Rousset, *Carbon N. Y.* **2001**, *39*, 507.

[4] K.S.W. Sing, *Pure Appl. Chem.* **1984**, *57*, 603.

[5] G. Fagerlund, *Matériaux Constr.* **1973**, *6*, 239.

[6] L. S., S. J.E., T. M.A., T. M., in *Charact. Porous Solids Powders Surf. Area, Pore Size Density.*, Springer **2004**, 58.

[7] E.P. Barrett, L.G. Joyner, P.P. Halenda, *J. Am. Chem. Soc.* **1951**, *73*, 373.

[8] M. Luisa Ojeda, J. Marcos Esparza, A. Campero, S. Cordero, I. Kornhauser, F. Rojas, *Phys. Chem. Chem. Phys.* **2003**, *5*, 1859.

[9] J.C. Groen, L.A.A. Peffer, P. Javier, **2003**, *60*, 1.

[10] P. Schneider, *Appl. Catal. A Gen.* **1995**, *129*, 157.

[11] K. Kaneko, *J. Memb. Sci.* **1994**, *96*, 59.

[12] L. Reimer, *Scanning Electron Microscopy*, Springer **1998**.

[13] D. Stokes, *Principles and Practice of Variable Pressure: Environmental Scanning Electron Microscopy*, Wiley-Blackwell **2008**.

[14] R.F. Egerton, *Physical Principles of Electron Microscopy: An Introduction to TEM, SEM, and AEM*, Springer **2011**.

[15] H. Reimer, L. Kohl, *Transmission Electron Microscopy: Physics of Image Formation*, Springer **2008**.

[16] C.B. Williams, D.B., Carter, *Transmission Electron Microscopy*, Springer **2009**.

[17] P. Echlin, *Handbook of Sample Preparation for Scanning Electron Microscopy and X-Ray Microanalysis*, Springer, **2009**.

[18] D. Ayache, J., Beaunier, L., Boumendil, J., Ehret, G., Laub, *Sample Preparation Handbook for Transmission Electron Microscopy*, Springer, **2010**.

[19] B.D. Cullity and S.R.Stock, *Elements of X-RAY DIFFRACTION Second Edition*, Addison-Wesley **1978**.

[20] N. Colthup, L. Daly, *Introduction to Infrared and Raman Spectroscopy*, Academic Press **1975**.

[21] P. Griffith, J. de Haseth, *Fourier Transform Infrared Spectroscopy*, Wiley-New York **1986**.

[22] B. Smith, *Fundamentals of Fourier Transform Infrared Spectroscopy*, CRC Press Taylor & Francis Group **2006**.

[23] D.A. Long, *The Raman Effect: A Unified Treatment of the Theory of Raman Scattering by Molecules*, John Wiley & Sons Ltd **2002**.

[24] R.S. Das, Y.K. Agrawal, *Vib. Spectrosc.* **2011**, *57*, 163.

[25] H. Bowley, D. Gardiner, *Practical Raman Spectroscopy*, Springer **1989**.

3. Hydrated salts phase change material nanocapsules

Crystalline hydrated salts are a type of PCMs with big potential in practice. They are widely available and of low cost. Not like organic phase change material (OPCM), they are non-flammable and non-toxic. Their latent heat of fusion is high and their thermal conductivity is often 2-3 times of OPCM. However, the problems of leakage on melting, phase separation, supercooling, degradation of phase change enthalpy due to the loss of hydrate water limit the application of hydrated salts as PCM. In the previous solutions, each single problem was addressed by a separate method. In this work, however, the nanoencapsulation of hydrated salts PCM is expected to be an innovative solution to address multiple problems.

To reduce the phase separation of hydrated salts, thickening agents such as superabsorbent polymer[1] and cellulose[2][3] have been commonly applied. This strategy shows its limitation as phase separation of hydrated salts can be only inhibited for the first few thermal cycles, since the boundary interface between PCM crystals and thickening agent increases. Nanoencapsulation offers the nanoconfinement of hydrated salts, and the PCM is more evenly distributed, so the phase separation should subside. Different as addition of thickening agents, this method should be favourable to increase the cycling performance of the PCM due to the encapsulation. To deal with the supercooling of hydrated salts, usually nucleating agents such as borax[4] and metal nanoparticles[5][6] can be added. These mixtures, however, have poor thermal stability, as PCM crystal and the additives tend to separate during cycling. Nanoencapsulation largely increases the surface area of PCM and accelerated the heat transfer rate, so the supercooling should be mitigated or overcome without help of nucleating agent.

The previous researches on micro/nanoencapsulation of PCM are mainly on OPCM[7]–[12], as it is difficult to formulate water soluble hydrated salt PCM core. The nanoencapsulation of hydrated salts PCM is rarely reported. In this chapter, four nanocapsule systems polyethylcyanoacrylate nanocapsules with $NaOAc \cdot 3H_2O$ PCM ($NaOAc \cdot 3H_2O$@polyethylcyanoacrylate), polymethylmethacrylate nanocapsules with $Na_2HPO_4 \cdot 12H_2O$ PCM ($Na_2HPO_4 \cdot 12H_2O$@polymethylmethacrylate), gelatine nanocapsules with $KAl(SO_4)_2 \cdot 12H_2O$ PCM ($KAl(SO_4)_2 \cdot 12H_2O$@gelatine) and SiO_2 nanocapsules with $Na_2SO_4 \cdot 10H_2O$ PCM ($Na_2SO_4 \cdot 10H_2O$@SiO_2) were fabricated and investigated. As it was the first time to fabricate these types of nanocapsules, the success in loading of respective hydrated salt in the capsules needs to be evaluated.

3.1 Polyethylcyanoacrylate nanocapsules with NaOAc·3H₂O as phase change material

Sodium acetate trihydrate (SAT, $NaOAc \cdot 3H_2O$) is a classical hydrated salt PCM with the melting temperature of 58 °C and high latent heat of fusion of 226 $J \cdot g^{-1}$[13]. With low cost it has been widely used in waste heat storage and solar heat[14]-[16]. However, it has serious problems of phase separation, supercooling and instability over thermal cycling[17]. In this work, the nanoencapsultion of pure sodium acetate trihydrate was intented without addition of thickning agent and nucleating agent.

Polyethylcyanoacrylate (PECA) is an acrylic resin with good sealing property and structural flexibility to adapt the volume change of PCM core over phase transformations[18]. The polymerisation mechanisms to form polyethylcyanoacrylate from ethyl cyanoacrylate as monomer is shown in Sch. 3-1. The polymerisation was initiated by the nucleophile addition from water molecule to ethyl cyanoacrylate. The generated carbanion acts as nucleophile to attack a further ethyl cyanoacylate, and the polymer chain propagates by repeated nucleophile addition to the monomer.

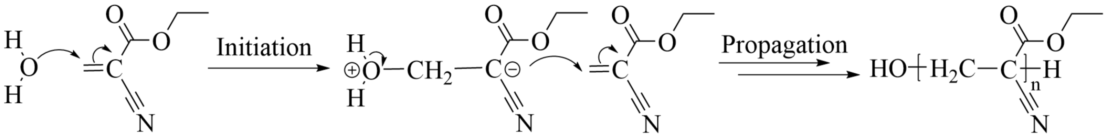

Sch. 3-1 Polymerisation mechanism to form polyethylcyanoacrylate

Lambert etc.[19]fabricated nanocapsules of isobutylcyanoacrylate containing aqueous core for drug delivery. The obtained nanocapsules were 20 to 400 nm. The acylate shell was formed by interfacial polymerisation in a w/o emulsion. This method was applied to fabricate polyethylcyanoacrylate nanocapsules with $NaOAc \cdot 3H_2O$ PCM ($NaOAc \cdot 3H_2O$@polyethylcyanoacrylate). However, as the property of the PCM core is different from the drug, the feasibility of the method needs to be proved.

3.1.1 Experimental part

3.1.1.1 Chemicals and instruments

The chemical reagents applied in the fabrication of NaOAc·3H_2O@ polyethylcyanoacrylate are listed in Tab. 3-1.

Tab. 3-1 Chemical reagents for the fabrication of NaOAc·3H_2O@ polyethylcyanoacrylate

Reagent	Purity	Supplier
NaOAc·3H_2O	>99%	Sigma, UK
Ethanol	99%	Sigma, UK
*Miglyol 812	Reagent grade	Oleo Chemical, Germany
*Span 80	Reagent grade	Sigma, UK
Ethyl cyanoacrylate	Reagent grade	Sigma, UK

**Miglyol 812 is composed of 55% triglycerides of C8 and 45% triglycerides of C10 fatty acids; Span 80 is sorbitan monooleate*

All the reagents were used as purchased without further purification. Milli Q water has been used in the washing process.

The instruments used to fabricate and characterise NaOAc·3H_2O@ polyethylcyanoacrylate are listed in Tab. 3-2.

Tab. 3-2 Instruments for the fabrication and characterisation of NaOAc·3H_2O@ polyethylcyanoacrylate

Instrument	Model	Supplier
Ultrasonicator	Q500	Qsonica, US
Centrifuge	2-16 KL	Sigma, UK
Scanning electron microscopy (SEM)	JSM- 7001F	JEOL, Japan
Fourier transform infrared spectroscopy (FTIR)	TENSOR II	Bruker, Germany

3.1.1.2 Procedure and characterisation

The procedure was modified from the method of Lambert etc.[19] to fabricate polyisobutylcyanoacrylate nanocapsules with aqueous core. 1 g $NaOAc \cdot 3H_2O$ was dissolved in 1 mL mixture of ethanol and water (1:4). The aqueous phase was added to an organic phase of 8 g Miglyol 812 and 1.5 g Span 80. The mixture was sonicated at 50 amplitude for 5 min in a pulse mode of 10 s sonicated and 5 s pause to obtain the w/o miniemulsion. Then 100 µL of monomer ethyl cyanoacrylate was added slowly to the miniemulsion under stirring at 600 rpm. The polymerisation was carried out at R.T. for 4h. Then the sample was centrifuged (6000 rpm, 10 min) and washed with ethanol. After drying at ambient conditions overnight, white powder as end product was obtained.

The morphology of the sample was characterised by SEM. The JSM-7001F setup was applied. For sample preparation, a small amount of sample was deposited on a sample holder with an adhesive carbon foil. To increase the conductivity, 100 nm Cr was sputtered on the sample. The chemical composition was characterised by FTIR using TENSOR II instrument. The sample powder was directly used for measurement. The transmittance mode was recorded in the wavenumber range from 400 to 4000 cm^{-1} with 64 consecutive scans.

3.1.2 Results and discussions

The SEM image of $NaOAc \cdot 3H_2O$@polyethylcyanoacrylate is shown in Fig. 3-1. Instead of single dispersed nanocapsules, serious aggregation of particles and big block material were formed.

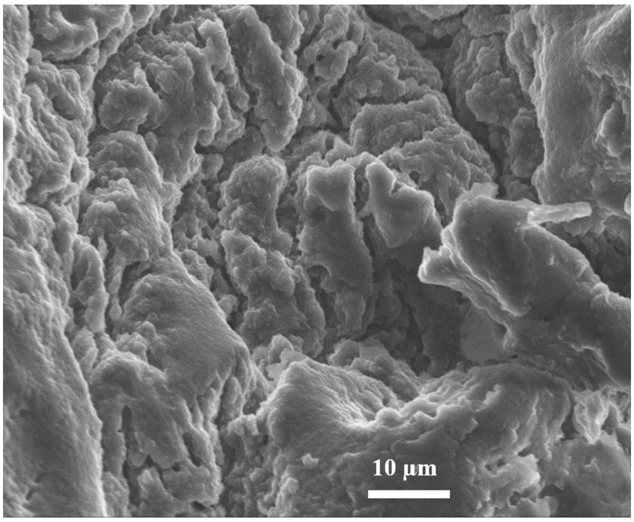

Fig. 3-1 SEM image of $NaOAc·3H_2O$@polyethylcyanoacrylate

The FTIR patterns of the product $NaOAc·3H_2O$@polyethylcyanoacrylate and $NaOAc·3H_2O$ are displayed in Fig. 3-2. The data of transmittance spectra is tabulated in Tab. 3-3. The FTIR of the product showed a typical pattern of polyethylcyanoacrylate[20]. The peak at 2925 cm^{-1} (A) is from C-H stretching vibration. The one at 1738 cm^{-1} (B) is due to the normal dimeric carboxylic C=O stretching vibration. The peak at 1440 cm^{-1} (C) is from C-H bending vibration. The peaks at 1246 cm^{-1} (D) and 1157 cm^{-1} (E) are attributed to C-CO-C strectching and bending vibrations. Further, 1009 cm^{-1} (F) is from O-C-C bending of esters from the primary alcohols, 851 cm^{-1} (G) from streching of alkanes and 746 cm^{-1} (H) from CH_2 rocking vibration of –CH_2 long chains. On the other hand, the FTIR spectrum of $NaOAc·3H_2O$ shows an obviously different pattern. The broad peaks in the range from 3500 cm^{-1} to 3000 cm^{-1} are attributed to O-H stretching of hydrate water molecules. The peak at 1699 cm^{-1} (I) is from C=O stretching, while the peaks at 1632 cm^{-1} (II) and 1546 cm^{-1} (III) are from symmetric and asymmetric C-O stretching, and the peak at 1410 cm^{-1} (IV) is due to C-H bending[21]. By comparing the FTIR spectrum of the product to $NaOAc·3H_2O$, it is clear, $NaOAc·3H_2O$ was not encapsulated in the product.

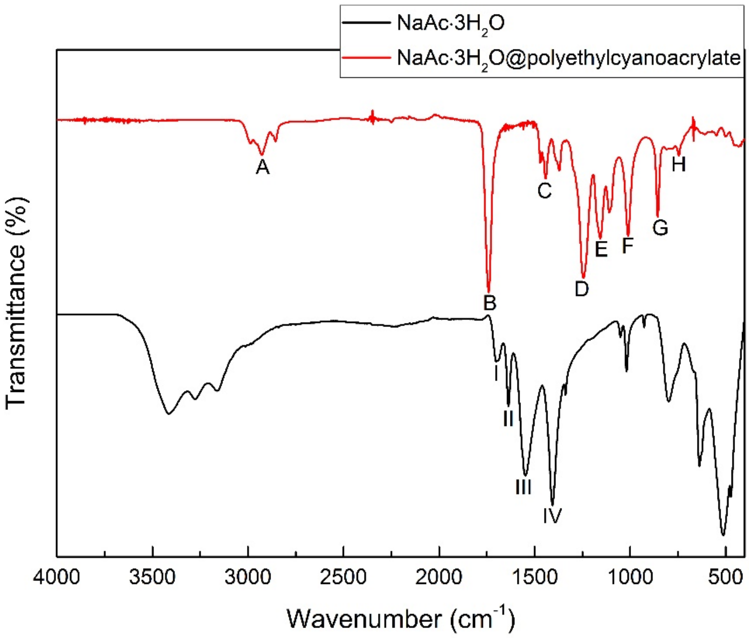

Fig. 3-2 FTIR spectra of NaOAc·3H_2O@polyethylcyanoacrylate and NaOAc·3H_2O

Tab. 3-3 Tabulation of FTIR spectra transmittance of NaOAc·3H_2O @polyethylcyanoacrylate[20] and NaOAc·3H_2O[21]

Signal	A	B	C	D	E	F
Peak position (cm^{-1})	2925	1738	1440	1246	1157	1009
Assignment	C-H	C=O	C-H	C-CO-C	C-CO-C	O-C-C
Signal	G	H	I	II	III	IV
Peak position (cm^{-1})	851	746	1699	1632	1546	1410
Assignment	Alkanes	CH_2-	C=O	C-O	C-O	C-H

As shown in Fig. 3-3, NaOAc·3H_2O@polyethylcyanoacrylate shows no phase change peak in the DSC curves. This result is in consistent with the result from the FTIR characterisation.

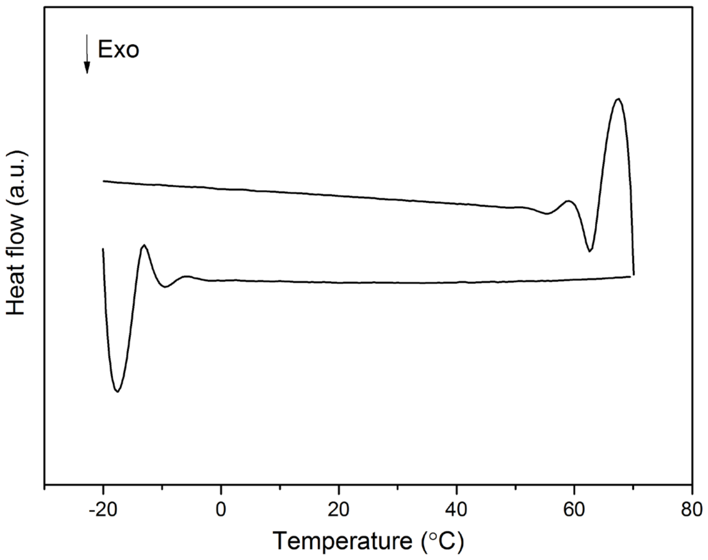

Fig. 3-3 DSC curves of NaOAc·3H_2O@polyethylcyanoacrylate

3.1.3 Conclusions

The experiment on fabricating nanocapsules with NaOAc·3H_2O as core and polyethylcyanoacrylate as shell was not successful. Polyethylcyanoacrylate polymer blocks were formed without encapsulating NaOAc·3H_2O. The possible reason is the fast polymerisation reaction of ethylcyanoacrynate in the presence of water, as shown in Sch. 3-1. Instead of forming polymer shell around the hydrated salts droplets in the interface of water and oil phase, polymer blocks were rapidly formed in the water phase.

3.2 Polymethylmethacylate nanocapsules with $Na_2HPO_4 \cdot 12H_2O$ as phase change material

Disodium hydrogen phosphate dodecahydrate (DHPD, $Na_2HPO_4 \cdot 12H_2O$) is a useful PCM with the melting temperature at 40 °C and very high latent heat of fusion of 265 $J \cdot g^{-1}$[22]. It is of low cost and could be used in buildings[23]. It also has obvious shortcomings such as serious phase separation and supercooling over thermal cycling. Huang etc.[24] fabricated microcapsules with $Na_2HPO_4 \cdot 7H_2O$ as PCM and polymethylmethacrylate (PMMA) as shell in size of several micrometres, whereby no phase separation of PCM was observed. For the formation of PMMA polymer shell, they carried out solvent evaporation precipitation from a suspension.

The polymerisation mechanism from methyl methacrylate to polymethylmethacrylate is shown in Sch. 3-2. Overall, it is a free radical addition polymerisation. First, the free radical is generated by homogeneous splitting of peroxide bond of the initiator. As the free radical attacks the ending of the allyl bond in methyl methacrylate, the polymerisation is started. The produced carbon radical reacts further with methyl methacrylate to form the polymer chain of polymethylmethacrylate.

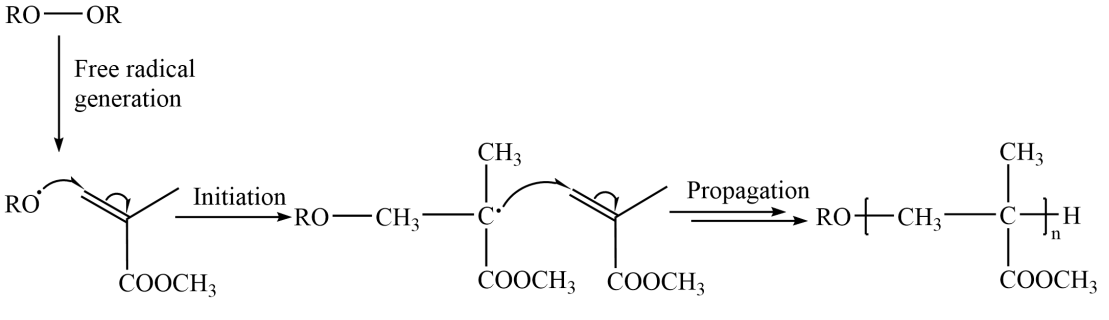

R: Ph-CO- for dibenzoyl peroxide as initiator

Sch. 3-2 Polymerisation mechanism to form polymethylmethacrylate

In my work, a reduced nanocapsule system with $Na_2HPO_4 \cdot 12H_2O$ as starting PCM and polymethylmethacrylate as shell ($Na_2HPO_4 \cdot 12H_2O$@polymethylmethacrylate) was designed by polymerisation from a w/o miniemulsion, the same solvent evaporation precipitation technique was applied. The morphology and thermal properties of the as fabricated $Na_2HPO_4 \cdot 12H_2O$@ polymethylmethacrylate system were evaluated.

3.2.1 Experimental part

3.2.1.1 Chemicals and instruments

The chemical reagents applied in the fabrication of $Na_2HPO_4\cdot12H_2O$@polymethylmethacrylate are listed in Tab. 3-4.

Tab. 3-4 The chemical reagents for the fabrication of $Na_2HPO_4\cdot12H_2O$@ polymethylmethacrylate

Reagent	Purity	Supplier
$Na_2HPO_4\cdot12H_2O$	>99%	Sigma, Germany
Span 80	Reagent grade	Sigma, UK
Methyl methacrylate	Reagent grade	Sigma, UK
Ethyl acrylate	Reagent grade	Sigma, UK
Toluene	99.8%	Sigma, UK
Acetone	99%	Sigma, UK
Hexane	99.5%	Sigma, UK
Dibenzoyl peroxide	Reagent grade	Sigma, UK
Hydroquinone monomethyl ether	Reagent grade	Sigma, UK

All the reagents were used as purchased without further purification. Milli Q water has been used in the washing process.

The instruments used to fabrication and characterisation of $Na_2HPO_4\cdot12H_2O$ @polymethylmethacrylate are listed in Tab. 3-5.

Tab. 3-5 Instruments for the fabrication and characterisation of $Na_2HPO_4 \cdot 12H_2O$@ polymethylmethacrylate

Instrument	Model	Supplier
Ultrasonicator	Q500	Qsonica, US
Centrifuge	2-16 KL	Sigma, UK
Scanning electron microscopy (SEM)	JSM- 7001F	JEOL, Japan
Differential scanning calorimeter (DSC)	214 NETZSCH	NETZSCH, Germany

3.2.1.2 Procedure and characterisation

The procedure is modified from the fabrication of microcapsules with polymethylmethacrylate shell[25]. 10 g $Na_2HPO_4 \cdot 12H_2O$ was melt to liquid and mixed with 50 mL toluene in the presence of 1.0 mL Span 80 as surfactant. Then the mixture was emulsified by sonication at 50 amplitude for 5 min in a pulse mode of 10 s sonication and 5 s pause. 5 g H_2O was added as extra supplementary water during the emulsification. Next, 12.5 mL methyl methacrylate (MMA) dissolved in 30 mL acetone was added to the emulsion. The mixture was heated to 80 °C and stirred at 900 rpm for 30 min. By dripping a small amount of ethyl acrylate (EA) solution (2.5 mL EA dissolved in 10 mL toluene) and adding dibenzoyl peroxide (BPO) as initiator the precipitation was started. The reaction mixture was stirred at 800 rpm at the temperature range from 80 to 90 °C for 4 h. At the end of the reaction 0.001 g hydroquinone monomethyl ether as inhibitor was added. The crude product was centrifuged (4000 rpm, 10 min) and washed by hexane. After drying at R.T. for 24 h, white powder as end product was obtained. The morphology of the sample was characterised by SEM with JSM-7001F model. For sample preparation, a small amount of sample was deposited on a sample holder with an adhesive carbon foil. To increase the conductivity, 100 nm Cr was sputtered on the sample. The phase change property was characterised by DSC with 214 Netsch model. The measurements were undertaken in the temperature range from -20 to 70 °C with the ramp of 10 $°C \cdot min^{-1}$ under nitrogen atmosphere.

3.2.2 Results and discussions

The SEM images of $Na_2HPO_4 \cdot 12H_2O$@polymethylmethacrylate are shown in Fig. 3-4. Aggregation of nanoparticles is observed. Small blocks in size of several micrometres are present.

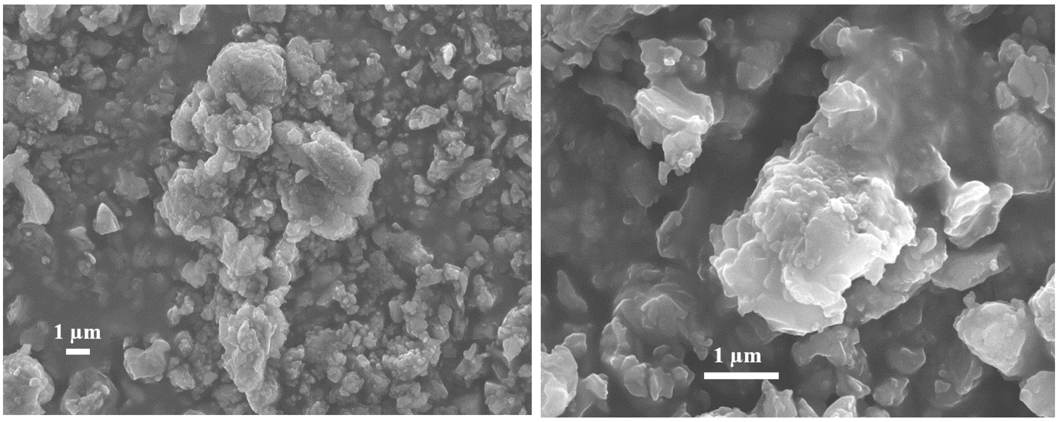

Fig. 3-4 SEM images of $Na_2HPO_4 \cdot 12H_2O$@polymethylmethacrylate

The DSC curves of $Na_2HPO_4 \cdot 12H_2O$@polymethylmethacrylate are displayed in Fig. 3-5. The sample shows a main melting peak at 56.3 °C with a shoulder at 54.2 °C. Instead of $Na_2HPO_4 \cdot 12H_2O$， $Na_2HPO_4 \cdot 7H_2O$ is the main component in the composite. The phase separation of the hydrated salt is not completely inhibited. The melting enthalpy is 130.9 $J \cdot g^{-1}$.

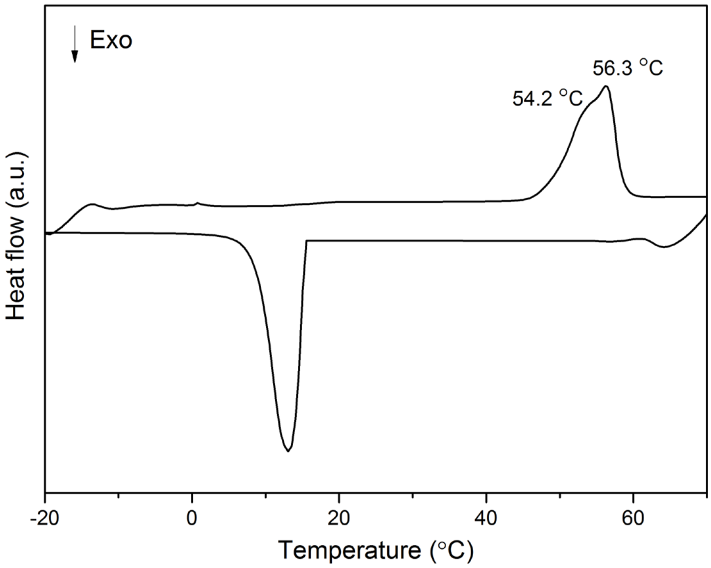

Fig. 3-5 DSC curves of $Na_2HPO_4·12H_2O$@polymethylmethacrylate

3.2.3 Conclusions

The fabrication of $Na_2HPO_4·12H_2O$@polymethylmethacrylate by miniemulsion polymerisation and solvent evaporation precipitation methods has generated micrometre-sized blocks and aggregation of particles. $Na_2HPO_4·7H_2O$ has been incorporated into the composite, as shown in DSC curves. This results are in consistent with the report in literature[25]. The morphology and the phase change property are not improved.

3.3 Gelatine nanocapsules with $KAl(SO_4)_2 \cdot 12H_2O$ as phase change material

Potassium aluminium sulphate dodecahydrate (KAlum, $KAl(SO_4)_2 \cdot 12H_2O$) has the melting temperature of 86 °C and high latent heat of fusion of 260 $J \cdot g^{-1}$[26]. As a common hydrated salt PCM with relative high melting point, it could have great potential in the utilisations of solar assisted thermal storage[27]. Its main problems are supercooling and instability over thermal cycling. The encapsulation of $KAl(SO_4)_2 \cdot 12H_2O$ has been reported in the work from Toth etc.[28]. They applied coacervation method to fabricate $KAl(SO_4)_2 \cdot 12H_2O$ macrocapsules with ethyl cellulose and polymethylmethacrylate coatings. The obtained capsules were in big size of 1.25-2 mm, and leakage of the salt was tested.

Gelatine is a natural polymer with low cost. It is generated from partial hydrolysis of collagen from animal skins and bones[29], and composed of peptides and proteins[30]. Due to the non-toxic, biodegradable and biocompatible properties[30], it is a useful material widely used in food and pharma industry[31][32]. Using gelatine to fabricate PCM capsules has never been reported.

In this work, the fabrication of gelatine nanocapsules with $KAl(SO_4)_2 \cdot 12H_2O$ PCM ($KAl(SO_4)_2 \cdot 12H_2O$@gelatine) was designed by thermal denaturation treatment of gelatine in a w/o miniemulsion. The procedure was derived from generation of gelatine microparticles by thermal denaturation in emulsion, as reported by Gallo etc.[33]. The denaturation temperature at 140 °C should change the solubility of gelatine and make the under cooling precipitated particles form-stable in solvent, but the chemical composition of gelatine is unchanged, and the in gelatine entrapped water molecules is mostly remained[34]. The morphology and thermal properties of the as synthesised nanocapsules were evaluated.

3.3.1 Experimental part

3.3.1.1 Chemicals and instruments

The chemical reagents applied in this section are listed in Tab. 3-6.

Tab. 3-6 Chemical reagents for the fabrication of $KAl(SO_4)_2 \cdot 12H_2O$@gelatine

Reagent	Purity	Supplier
$KAl(SO_4)_2 \cdot 12H_2O$	99%	Sigma, UK
Gelatine	Type A, 175 Bloom	Sigma, UK
Sunflower oil	Bp. 200-220 °C	Amazon, UK
Diethyl ether	99.5%	Sigma, UK

All the reagents were used as purchased without further purification. Milli Q water has been used in the washing process.

The instruments used to fabrication and characterisation all the samples in this section are listed in Tab. 3-7.

Tab. 3-7 Instruments for the fabrication and characterisation of $KAl(SO_4)_2 \cdot 12H_2O$ @gelatine

Instrument	Model	Supplier
Ultrasonicator	Q500	Qsonica, US
Centrifuge	2-16KL	Sigma, UK
Scanning electron microscopy (SEM)	JSM- 7001F	JEOL, Japan
Energy-dispersive X-ray spectroscopy (EDS)	JSM-7001F	JEOL, Japan
Transmission electron microscopy (TEM)	STEM-2100F	JEOL, Japan
Fourier transform infrared spectroscopy (FTIR)	TENSOR II	Bruker, Germany
X-Ray diffraction (XRD)	Diffractometer with CuK_a radiation	Bruker, Germany
Differential scanning calorimeter (DSC)	214 NETZSCH	NETZSCH, Germany

3.3.1.2 Procedure and characterisation

The fabrication of $KAl(SO_4)_2 \cdot 12H_2O$@gelatine nanocapsules was carried out by precipitation of gelatine in a miniemulsion. The stabilisation of the gelatine shell is through thermal denaturation[33]. 250 mg gelatine (Type A, 175 Bloom) and 400 mg $KAl(SO_4)_2 \cdot 12H_2O$ were dissolved in 2 mL H_2O at 35°C and the solution was stirred for 10 minutes. 0.5 mL of the as-formed aqueous solution was added in 30 mL sunflower oil. The mixture was sonicated at 50 amplitude for 5 min in a pulse mode of 10 s sonication and 5 s pause. Then the generated w/o miniemulsion was dripped dropwise to 100 mL oil at 140 °C under stirring at 1500 rpm. After heating for 10 min, the suspension was cooled down at R.T. Then, the samples were centrifuged (6000 rpm, 5 min) and washed with diethyl ether. After drying in the air for 24 h, white powder as end product was obtained.

The morphology of the sample was characterised by SEM with JSM-7001F model. For sample preparation, a small amount of sample was deposited on a sample holder with an adhesive carbon foil. To increase the conductivity, 100 nm Cr was sputtered on the sample. EDS, which was obtained in conjunction with SEM, was applied for elemental analysis. TEM images were also acquired under the STEM-2100F mode at 200 kV. The chemical composition was characterised by FTIR using TENSOR II instrument. The sample powder was directly used for measurement. The transmittance mode was recorded in the wavenumber range from 400 to 4000 cm^{-1} with 64 consecutive scans. The crystal structure of the samples was analysed by X-ray diffraction. The diffraction data were recorded in the range of 5-50 ° with the scan speed of 1 ° min^{-1}. The phase change property was characterised by DSC with 214 Netsch model. The measurements were undertaken in the temperature range from -20 to 110 °C with the ramp of 10 $°C \cdot min^{-1}$ under nitrogen atmosphere.

3.3.2 Results and discussions

The SEM image of $KAl(SO_4)_2 \cdot 12H_2O$@gelatine is shown in Fig. 3-6a. Particles with diameter from 200 nm to 4 μm were obtained. The size distribution is not uniform. The morphology of the particles keeps well after heating at 140 ˚C for 10 min (Fig. 3-6b).

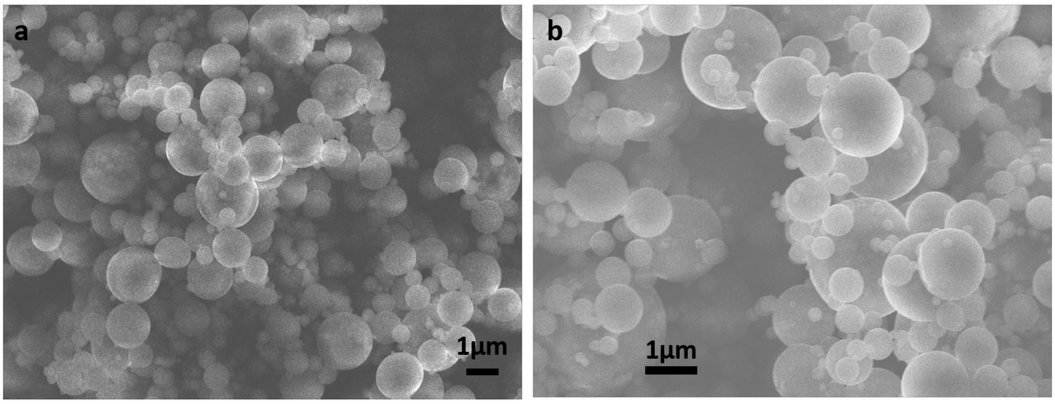

Fig. 3-6 SEM images of $KAl(SO_4)_2 \cdot 12H_2O$@gelatine (a) before (b) after heating at 140 ˚C

The EDS of $KAl(SO_4)_2 \cdot 12H_2O$@gelatine is shown in Fig. 3-7. The elements Al, K, S from $KAl(SO_4)_2 \cdot 12H_2O$ are detected.

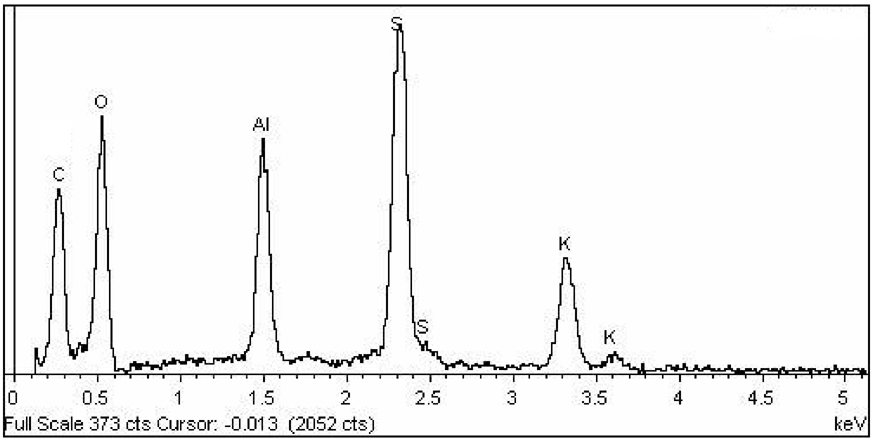

Fig. 3-7 EDS of $KAl(SO_4)_2 \cdot 12H_2O$@gelatine

The TEM image of $KAl(SO_4)_2 \cdot 12H_2O$@gelatine is shown in Fig. 3-8. The core-shell structure is evident. The gelatine shell shows a transparent texture, and the inorganic salts are as dark core material. The core material is well wrapped by the shell. No breakage in the shell is observed.

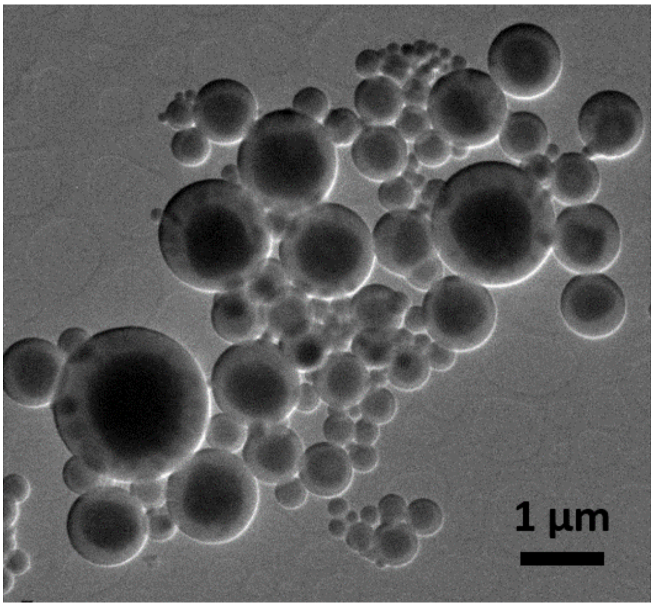

Fig. 3-8 TEM image of $KAl(SO_4)_2·12H_2O$@gelatine (collected from technician)

The FTIR spectrum of $KAl(SO_4)_2·12H_2O$@gelatine comparing to the spectra of gelatine and $KAl(SO_4)_2·12H_2O$ is displayed in Fig. 3-9. The data of the transmittance spectra is summarised in Tab. 3-8[35]-[37]. $KAl(SO_4)_2·12H_2O$ shows strong peaks at 3346 cm^{-1} and 2888 cm^{-1} due to the O-H stretching vibrations from the hydrated water. The strong peak at 1617 cm^{-1} is from the S=O stretching vibration of sulphate. The peaks at 1189 cm^{-1}, 1084 cm^{-1} and 586 cm^{-1} are attributed to the vibrations of SO_4^{2-}. The peak at 680 cm^{-1} is from the stretching vibration of $[Al(H_2O)_6]^{3+}$. On the other hand, gelatine shows the different FTIR spectrum pattern as $KAl(SO_4)_2·12H_2O$. The broad peak at 3285 cm^{-1} is from the N-H stretching bond of amide, and the medium peak at 1628 cm^{-1} is attributed to the C=O stretching vibration of amide[35]. The peak at 1519 cm^{-1} is mainly from the N-H bending vibration of amide[36]. The peak at 1445 cm^{-1} is attributed to the bending vibration of methyl group. $KAl(SO_4)_2·12H_2O$@gelatine shows a similar pattern as gelatine in the range from 1300 to 4000 cm^{-1}. Peaks from N-H and C=O are observed at 3291 cm^{-1}, 1537 cm^{-1} and 1643 cm^{-1}, indicating the chemical structure of gelatine is kept well in the capsules. However, the peaks from vibrations of O-H from the hydrate water is not observed in spectrum of $KAl(SO_4)_2·12H_2O$@gelatine. Also the peak from $[Al(H_2O)_6]^{3+}$ disappears by the capsules. Although the vibration peaks from SO_4^{2-} are evidently present at 1217 cm^{-1}, 1132 cm^{-1} and 605 cm^{-1}, which are a bit shifted comparing to the correspondent peaks in $KAl(SO_4)_2·12H_2O$ spectrum. It is suspected,

$KAl(SO_4)_2\cdot 12H_2O$ has lost its hydrated water when encapsulated in gelatine. The small shift by the SO_4^{2-} vibrations is due to the change of chemical structure of $KAl(SO_4)_2\cdot 12H_2O$ in the composite.

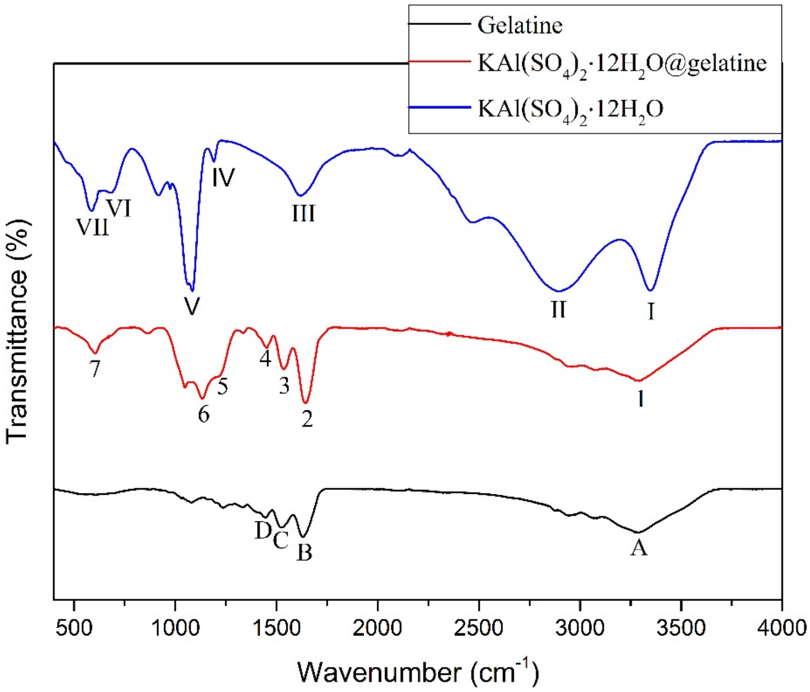

Fig. 3-9 FTIR spectra of gelatine, $KAl(SO_4)_2\cdot 12H_2O$ and $KAl(SO_4)_2\cdot 12H_2O$@ gelatine

Tab. 3-8 Tabulation of FTIR spectra transmittance of gelatine[35][36], $KAl(SO_4)_2\cdot 12H_2O$[37] and $KAl(SO_4)_2\cdot 12H_2O$@gelatine

Signal	A	B	C	D	
Peak position (cm^{-1})	3285	1628	1519	1445	
Assignment	N-H	C=O	N-H	CH_3-	
Signal	I	II	III	IV/V/VII	VI
Peak position (cm^{-1})	3346	2888	1617	1189/1084/586	680
Assignment	O-H	O-H	S=O	SO_4^{2-}	$[Al(H_2O)_6]^{3+}$
Signal	1	2	3	4	5/6/7
Peak position (cm^{-1})	3291	1643	1537	1450	1217/1132/605
Assignment	N-H	C=O	N-H	CH_3-	SO_4^{2-}

As displayed in Fig. 3-10, the measured XRD pattern of $KAl(SO_4)_2 \cdot 12H_2O$ is in good agreement with the standard PDF (Number: 07-0017). Both gelatine and $KAl(SO_4)_2 \cdot 12H_2O$@gelatine show no peak in the XRD patterns. The composite exhibits no crystallinity.

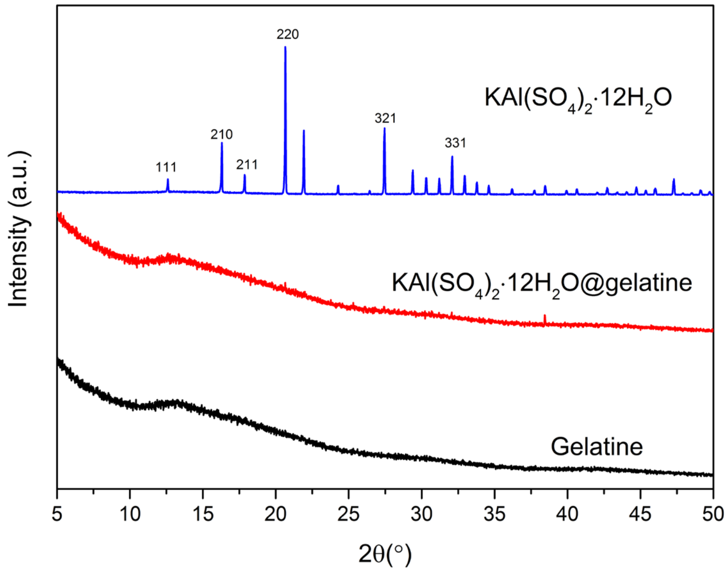

Fig. 3-10 XRD patterns of gelatine, $KAl(SO_4)_2 \cdot 12H_2O$ and $KAl(SO_4)_2 \cdot 12H_2O$ @gelatine

As shown in Fig. 3-11, $KAl(SO_4)_2 \cdot 12H_2O$@gelatine shows no phase change peak in the DSC curves.

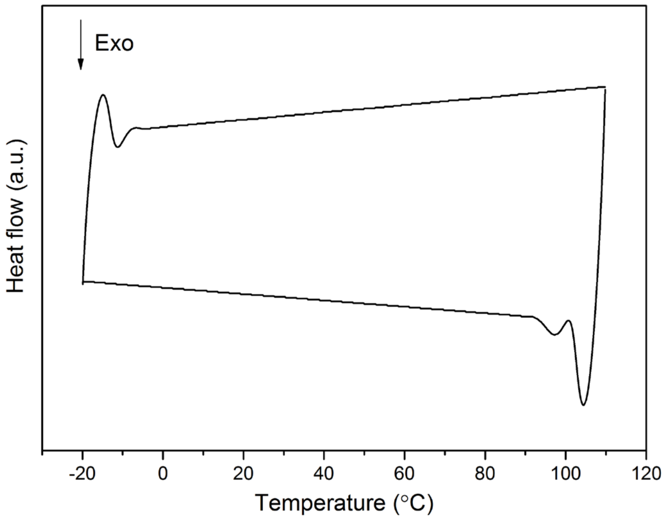

Fig. 3-11 DSC curves of $KAl(SO_4)_2 \cdot 12H_2O$@gelatine

3.3.3 Conclusions

$KAl(SO_4)_2 \cdot 12H_2O$@gelatine micro/nanocapsules with a core-shell structure are fabricated by miniemulsion polymerisation and thermal denaturation of gelatine. The capsules show no phase change property, the possible reason could be the hydrate water molecules were absorbed and entrapped in gelatine shell, making the recovery of crystalline hydrated salt impossible.

3.4 Silica nanocapsules with $Na_2SO_4 \cdot 10H_2O$ as phase change material

Sodium sulphate decahydrate (SDH, $Na_2SO_4 \cdot 10H_2O$), also known as Glauber's salt is a typical hydrated salt PCM with the melting temperature of 44 °C and the latent heat of fusion of 251 $J \cdot g^{-1}$[22]. It has been used in solar water thermal storage and buildings[37]. The main drawbacks include tendency to lose hydrate water in air, serious supercooling and phase separation over phase transitions[22].

Silica (SiO_2) is a common inorganic shell material in fabrication of microcapsules[38][39]. It has the advantages of non-flammability, higher thermal conductivity, better chemical and thermal stability and often higher mechanical strength comparing to organic polymer shells. Fang etc.[40] have microencapsulated paraffin as OPCM core with silica shell. In the first step, an oil in water emulsion containing paraffin in the oil phase was formed. Then, on the surface of the emulsion droplets, silica shell was generated by sol-gel method. The formation reactions of silica shell from tetraethyl orthosilicate as precursor is shown in Sch. 3-3. First, an alkoxysilane group is hydrolysed to a reactive silanol group. The silanol group could either condensate with another alkoxysilane group or with another silanol group from a second silane molecule and split small molecules such as alcohol and water. The network of the silica gel is formed by repeated hydrolysis and condensation.

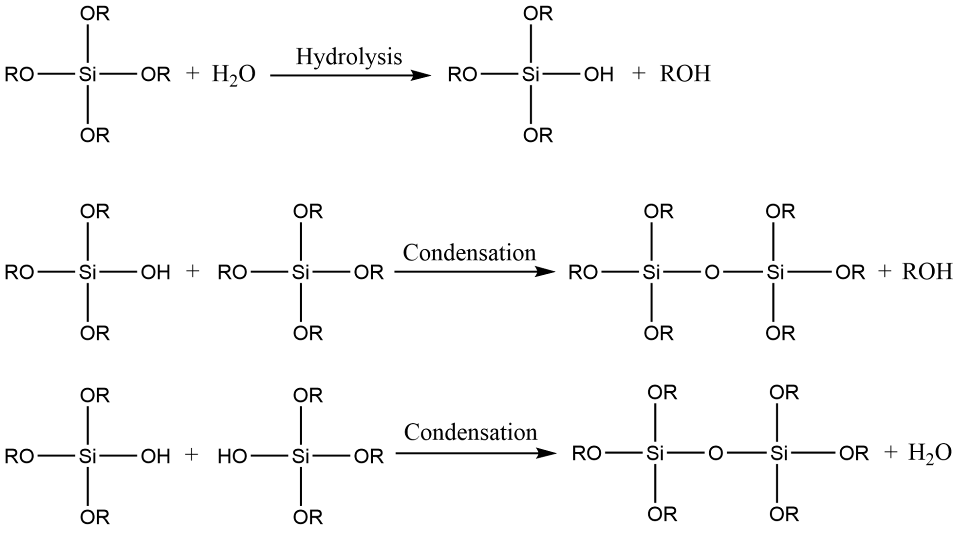

R: CH_3CH_2- for tetraethyl orthosilicate as precursor

Sch. 3-3 Silica gel formation by sol-gel method

In my work for nanoencapsulation of hydrated salts with silica shell, a water in oil miniemulsion with PCM in water phase was formed before fabrication of silica shell. The sol-gel method was applied as well. The morphology and properties of as synthesised silica nanocapsules with $Na_2SO_4 \cdot 10H_2O$ PCM ($Na_2SO_4 \cdot 10H_2O@SiO_2$) were evaluated.

3.4.1 Experimental part

3.4.1.1 Chemicals and instruments

The chemical reagents applied in this section are listed in Tab. 3-9.

Tab. 3-9 Chemical reagents for the fabrication of $Na_2SO_4 \cdot 10H_2O@SiO_2$

Reagent	Purity	Supplier
$Na_2SO_4 \cdot 10H_2O$	> 99%	Sigma, UK
Cyclohexane	99%	Sigma, Germany
n-pentanol	> 99%	Sigma, UK
Tetraethyl orthosilicate	> 99.5%	Sigma, UK
3-aminopropyl triethoxysilane	> 99.5%	Sigma, UK
Ethanol	> 99%	Sigma, UK

All the reagents were used as purchased without further purification. Milli Q water has been used in the washing process.

The instruments used to fabrication and characterisation all the samples in this section are listed in Tab. 3-10.

Tab. 3-10 Instruments for the fabrication and characterisation of $Na_2SO_4 \cdot 10H_2O$ @SiO_2

Instrument	Model	Supplier
Ultrasonicator	Q500	Qsonica, US
Scanning electron microscopy (SEM)	JSM- 7001F	JEOL, Japan
Digital pH meter	HI-98219	Hanna instruments, UK
Differential scanning calorimeter (DSC)	214 NETZSCH	NETZSCH, Germany

3.4.1.2 Procedure and characterisation

0.95 mL of sodium sulphate anhydrous solution (2 mol/L) was added to 25 mL of cyclohexane containing 0.18 g of sodium dodecyl sulphate (SDS) at 60 °C under stirring. Then 5 mL of n-pentanol was added. The mixture was sonicated at 50 amplitude for 5 min in a pulse mode of 10 s sonication and 5 s pause. Light white emulsion was obtained. Further, 0.70 mL of tetraethyl orthosilicate (TEOS) was added to the emulsion drop by drop at 60°C. Then the pH value of the mixture was adjusted to 9 by introducing 3-aminopropyl triethoxysilane (APTS), followed by stirring at 1000 rpm for 24 h at 60°C. After stirring, homogeneous milky suspension was obtained. It was washed with ethanol for three times (6000 rpm, 5 min each time) and dried at R.T. for 20 h.

The morphology of the product was characterised by SEM with JSM-7001F model. The sample preparation before measurement is described in chapter 2.3.1.2. The phase change property was characterised by DSC with 214 Netsch model. The measurements were undertaken in the temperature range from -20 °C to 70 °C with the ramp of 10 °C·min^{-1} under nitrogen atmosphere.

3.4.2 Results and discussions

The SEM image of $Na_2SO_4 \cdot 10H_2O@SiO_2$ in Fig. 3-12 shows, nanoparticles with uniform morphology and size are formed. The average diameter is 120 nm.

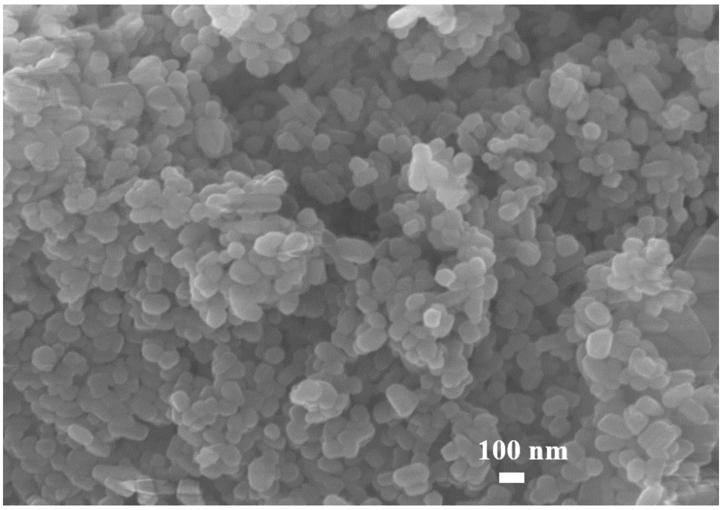

Fig. 3-12 SEM image of $Na_2SO_4 \cdot 10H_2O@SiO_2$

$Na_2SO_4 \cdot 10H_2O@SiO_2$ nanocapsules show no phase change peak in DSC curves, as shown in Fig. 3-13. $Na_2SO_4 \cdot 10H_2O$ should have lost all hydrated water during the drying and storing process. The SiO_2 shell is not compact enough to prevent the loss of water.

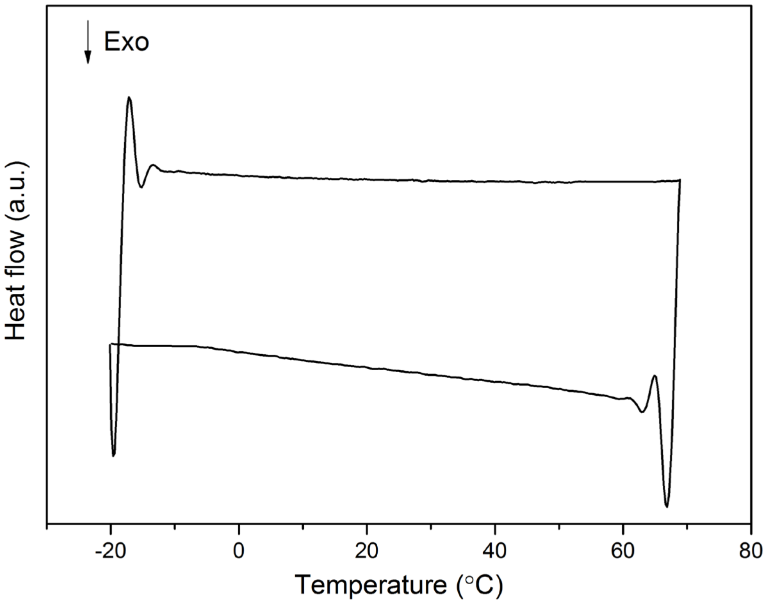

Fig. 3-13 DSC curves of $Na_2SO_4{\cdot}10H_2O@SiO_2$

3.4.3 Conclusions

$Na_2SO_4{\cdot}10H_2O@SiO_2$ nanocapsules in the average diameter of 120 nm are fabricated by sol-gel method. However, the capsules show no phase change property. The as synthesised SiO_2 shell could not retain the hydrate water in $Na_2SO_4{\cdot}10H_2O$.

References

[1] H.W. Ryu, S.W. Woo, B.C. Shin, S.D. Kim, *Sol. Energy Mater. Sol. Cells* **1992**, *27*, 161.

[2] L.F. Cabeza, G. Svensson, S. Hiebler, H. Mehling, *Appl. Therm. Eng.* **2003**, *23*, 1697.

[3] H.K. Shin, M. Park, H.-Y. Kim, S.-J. Park, *Appl. Therm. Eng.* **2015**, *75*, 978.

[4] G. Feng, X. Xu, N. He, H. Li, K. Huang, *Mater. Res. Innov.* **2015**, *19*, S5.

[5] B.M.L. Garay Ramirez, C. Glorieux, E. San Martin Martinez, J.J.A. Flores Cuautle, *Appl. Therm. Eng.* **2014**, *62*, 838.

[6] X. Wu, Y. Wang, R. Sun, M. Lai, R. Du, Z. Zhang, *J. Phys. Conf. Ser.* **2009**, *188*, 12046.

[7] Y. Özonur, M. Mazman, H.Ö. Paksoy, H. Evliya, *Int. J. Energy Res.* **2006**, *30*, 741.

[8] A. Jamekhorshid, S.M. Sadrameli, M. Farid, *Renew. Sustain. Energy Rev.* **2014**, *31*, 531.

[9] Y. Konuklu, M. Unal, H. Paksoy, *Sol. Energy Mater. Sol. Cells* **2014**, *120*, 536.

[10] Y. Konuklu, H.O. Paksoy, M. Unal, *Appl. Energy* **2015**, *150*, 335.

[11] E.M. Shchukina, M. Graham, Z. Zheng, D.G. Shchukin, *Chem. Soc. Rev.* **2018**.

[12] E. Alehosseini, S.M. Jafari, *Trends Food Sci. Technol.* **2019**, *91*, 116.

[13] J. Heckenkamp, H. Baumann, *Latentwärmespeicher, Sonderdruck Aus Nachrichten 11*, **1997**.

[14] S. Arunachalam, **2019**, *141*, 1.

[15] P. Hu, D.-J. Lu, X.-Y. Fan, X. Zhou, Z.-S. Chen, *Sol. Energy Mater. Sol. Cells* **2011**, *95*, 2645.

[16] G. Zhou, Y. Xiang, *Sol. Energy* **2017**, *155*, 1261.

[17] W. Hua, X. Zhang, M.J. Muthoka, X. Han, *Materials (Basel).* **2018**, *11*, 1016.

[18] J. Yang, H. Lee, W. Hyung, S.B. Park, S. Haam, *J. Microencapsul.* **2006**, *23*, 203.

[19] G. Lambert, E. Fattal, H. Pinto-Alphandary, A. Gulik, P. Couvreur, *Pharm. Res.* **2000**, *17*, 707.

[20] R.M. Silverstein, F.X. Webster, *Spectrometric Identification Of Organic Compounds 6th Ed - Silverstein & Webster.Pdf*, Wiley **1998**.

[21] K. Ito, H.J. Bernstein, *Can. J. Chem.* **1956**, *34*, 170.

[22] M. Telkes, in *Proc. Work. Sol. Energy Storage Subsystems Heat. Cool. Build.*, Charlottesville **1975**.

[23] K. Huang, J. Li, X. Luan, L. Liu, Z. Yang, C. Wang, *ACS Omega* **2020**, *5*, 15210.

[24] J. Huang, T. Wang, P. Zhu, J. Xiao, *Thermochim. Acta* **2013**, *557*, 1.

[25] T.Y. Wang, J. Huang, *J. Appl. Polym. Sci.* **2013**, *130*, 1516.

[26] R. Naumann, H.H. Emons, *J. Therm. Anal.* **1989**, *35*, 1009.

[27] European Environment Agency (EEA), **2019**, *53*, 1689.

[28] J. TÓth, B. NÉmeth, Ján. Gyenis, *Period. Polytech. Chem. Eng.* **2015**, *59*, 201.

[29] A.A. Mariod, H.F. Adam, *Acta Sci. Pol. Technol. Aliment.* **2013**, *12*, 135.

[30] M.C. Gómez-Guillén, B. Giménez, M.E. López-Caballero, M.P. Montero, *Food Hydrocoll.* **2011**, *25*, 1813.

[31] D. Liu, M. Nikoo, G. Boran, P. Zhou, J.M. Regenstein, *Annu. Rev. Food Sci. Technol.* **2015**, *6*, 527.

[32] I. Akbar, I. Jaswir, P. Jamal, F. Octavianti, *Int. Food Res. J.* **2017**, *24*, 255.

[33] J.M. Gallo, C.T. Hung, D.G. Perrier, *Int. J. Pharm.* **1984**, *22*, 63.

[34] I. V Yann, *Eur. Polym. J.* **1968**, *4*, 257.

[35] Z.A. Nur Hanani, Y.H. Roos, J.P. Kerry, *11th Int. Congr. Eng. Food* **2011**, *5*, 6.

[36] J. Kong, S. Yu, *Acta Biochim. Biophys. Sin.* **2007**, *39*, 549.

[37] M. V Barashkov, A.I. Komyak, S.N. Shashkov, *J. Appl. Spectrosc.* **2004**, *71*, 328.

[38] J. Hirschey, K.R. Gluesenkamp, A. Mallow, S. Graham, *5th Int. High Perform. Build. Conf.* **2018**, 1.

[39] H. Zhang, X. Wang, D. Wu, *J. Colloid Interface Sci.* **2010**, *343*, 246.

[40] F. He, X. Wang, D. Wu, *Energy* **2014**, *67*, 223.

[41] Y. Fang, H. Wei, X. Liang, S. Wang, X. Liu, X. Gao, Z. Zhang, *Energy and Fuels* **2016**, *30*, 9652.

4. Halloysite form-stable hydrated salts phase change material

Halloysite is natural aluminosilicate mineral, which can be found across the world[1]. It has a similar chemical composition as kaolin. It is composed of the octahedral $Al(OH)_3$ sheet and its adjacent tetrahedral SiO_2 sheet. As these two sheets are not matched in the space, the layer shaped crystal curls into a tube. Halloysite has the morphology of hollow nanotubes, which are intact without curling, cracking or casing[2]. The inner lumen of the nanotubes is with the diameter of 10-30 nm and the length is from hundreds of nanometres to several micrometres[2]. Easy accessibility, low-cost, non-toxicity as well as regular nanoconfinement and high specific surface area[1] have made halloysite widely used as nanoreactors[3]-[5], adsorption materials[6] or nanocontainers for controlled release of functional materials[1][5]. In a few recent research works[7][8], they have been used as supporting matrix for organic phase change material (OPCM). Mei et al.[7] synthesised halloysite form-stable capric acid PCM via the liquid phase method. The loading efficiency was 60%. The phase change temperature of the composite was 29.3 ˚C and the latent heat reached 75.5 $J·g^{-1}$. The composite showed good shape stability after heating to 40 ˚C. Liang et al.[8] modified halloysite with polydimethylsiloxane (PDMS) and fabricated a series of halloysite form-stable OPCM composites via the vacuum impregnation method. The latent heat of the composites ranges from 44.7 to 72.1 $J·g^{-1}$.

The surface of halloysite nanotube is hydrophilic and it consists of inner and outer parts with different chemical composition. The inner surface of the tube lumen has a positive charge due to Al-OH groups, and the external surface is negative with siloxane (Si-O-Si) groups[2]. Till now, halloysite have not been reported as nanocontainers for encapsulation of inorganic crystallohydrate PCMs. In this chapter, $Na_2HPO_4·12H_2O$ (disodium phosphate dodecahydrate, DHPD) was first selected as target hydrated salt PCM to develop form-stable phase change material (FSPCM) with halloysite as it has the merits of high mass heat storage capacity and proper melting temperature. To address the phase separation problem of $Na_2HPO_4·12H_2O$, the PCM in liquid form was impregnated into halloysite nanotubes under vacuum. The nano-confinement effect of halloysite as supporting matrix on the performance of halloysite form-stable

$Na_2HPO_4 \cdot 12H_2O$ PCM ($Na_2HPO_4 \cdot 12H_2O$@halloysite) was evaluated. Further, to eliminate the phenomenon of phase separation in the FSPCM, the other hydrated salt $Na_2SO_4 \cdot 10H_2O$ (sodium sulphate decahydrate, SDH) with also high mass heat storage capacity and similar melting temperature was mixed with $Na_2HPO_4 \cdot 12H_2O$. The optimum mass ratio of $Na_2HPO_4 \cdot 12H_2O$ to $Na_2SO_4 \cdot 10H_2O$ to form eutectic hydrated salt (EHS) in the halloysite based FSPCM was determined. Combing the strategy of eutectic mixture and form-stable PCM with halloysite as mineral nanocontainers, the investigated halloysite form-stable eutectic hydrated salt PCM (EHS@halloysite) showed no phase separation, high loading efficiency and good stability over thermal cycling.

4.1 Experimental part

4.1.1 Chemicals and instruments

The chemical reagents applied in this chapter are listed in Tab. 4-1.

Tab. 4-1 Chemical reagents for the fabrication of hydrated salts@halloysite

Reagent	Purity/Form	Supplier
$Na_2SO_4 \cdot 10H_2O$	> 99%	Sigma, USA
$Na_2HPO_4 \cdot 12H_2O$	> 99%	Sigma, Germany
Halloysite nanoclay	Nanopowder	Aldrich, UK
$Na_2B_4O_7$ (borax)	≥ 99%, anhydrous	Sigma, UK

All materials were used as purchased without further purification. Milli Q water was applied as a solvent media.

The instruments used for the fabrication and characterisation of all the samples in this chapter are listed in Tab. 4-2.

Tab. 4-2 Instruments for the fabrication and characterisation of hydrated salts@ halloysite

Instrument	Model	Supplier
Ultrasonic Cleaner	USC 500TH	VWR, Germany
Vacuum oven	OV-11/12	JEIO Tech, UK
N_2 adsorption isotherms	3Flex 5.00	Micrometrics, UK
Scanning electron microscopy (SEM)	JSM- 7001F	JEOL, Japan
Energy-dispersive X-ray spectroscopy (EDS)	JSM- 7001F	JEOL, Japan
Transmission electron microscopy (TEM)	STEM- 2100F	JEOL, Japan
X-Ray diffraction (XRD)	Diffractometer with CuK_a radiation	Bruker, Germany
Fourier transform infrared spectroscopy (FTIR)	TENSOR II	Bruker, Germany
Differential scanning calorimeter (DSC)	214 NETZSCH	NETZSCH, Germany

4.1.2 Procedure and characterisation

The PCM@halloysite were prepared by sonication and impregnation of concentrated hydrated salts solutions under vacuum. First, 7 g hydrated salts were dissolved in 3 mL deionized H_2O under 40 °C. Then, 3 g halloysite was added to the solution forming a white suspension. The suspension was sonicated (output 100 W) at 40 °C for 30 minutes. After the sonication the mixture was put into the vacuum oven at 40 °C. To achieve better impregnation of the PCMs into the halloysite lumen, the samples were first put under vacuum for 10 min, then exposed to the air at room temperature for 10 min. This process was repeated two times. In the last step, the samples were cooled at 4 °C for 30 minutes and dried in desiccator at room temperature for 2 days until the weight was constant.

The pore properties of the inorganic matrixes were investigated by N_2 adsorption isotherms at 77 K using the 3Flex Version 5.00 from Micrometrics Instrument. All the matrixes samples were degassed at 250 ˚C for 2 h before measurement. The pore size distribution was depicted based on BJH report. The morphology of the samples was characterised by scanning electron microscopy (SEM) and transmission electron microscopy (TEM). SEM images were recorded by JSM-7001F setup. The samples were sputter coated by 100 nm chromium layer before measuring. TEM measurements were operated on STEM-2100F with STEM mode at 200 kV. The average diameter, inner diameter and shell thickness of the halloysite were calculated from 100 measurements. Energy-dispersive X-ray spectroscopy (EDS) was applied for elemental analysis. The chemical composition was characterised by Fourier transform infrared spectroscopy (FTIR) using TENSOR II instrument (Bruker, Germany) with all reflective diamond ATR. The transmittance mode was recorded from 400 to 4000 cm^{-1} as the result of 64 consecutive scans. The crystal structure of the samples was analysed by X-ray diffraction. The diffraction data were recorded in the range of 10-80 ° with the scan speed of 1 ° min^{-1}. The thermal properties including cycling tests were characterised by differential scanning calorimeter (DSC). The measurements were undertaken in the temperature range from -20 to 70 °C with the ramp of 10 $°C \cdot min^{-1}$ under nitrogen.

4.2 Results and discussions

4.2.1 Morphology and pore structure of halloysite

The SEM image of halloysite is shown in Fig. 4-1. Halloysite has the form of nanotubes, with an average outer diameter of 70 nm. The dominant morphologies are long tubes with the length from 800 nm to 1 μm, although some short tubes below 200 nm are observed.

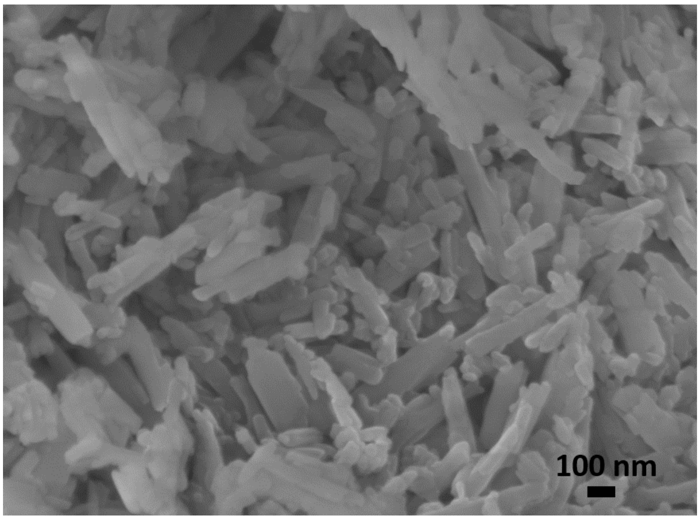

Fig. 4-1 SEM image of halloysite

The N_2 adsorption-desorption isotherms of halloysite are graphed in Fig. 4-2. Halloysite shows Type IV isotherms with H1 hysteresis loop, indicating the mesoporous character of the matrix. The course of the adsorption isotherm is attributed to the monolayer-multilayer adsorption of N_2 in the mesopores. The hysteresis loop is due to the capillary condensation in adsorption. The narrow steep shape of the loop indicates the mesopores distribute uniformly within a small range. According to the BET calculation, halloysite has the pore volume of 0.284 $cm^3 \cdot g^{-1}$ and the surface area of 68.96 $m^2 \cdot g^{-1}$. The pore size distribution characterised by BJH method is shown in Fig. 4-3. The main pore size of halloysite is 23 nm, corresponding to the size of inner lumen of halloysite.

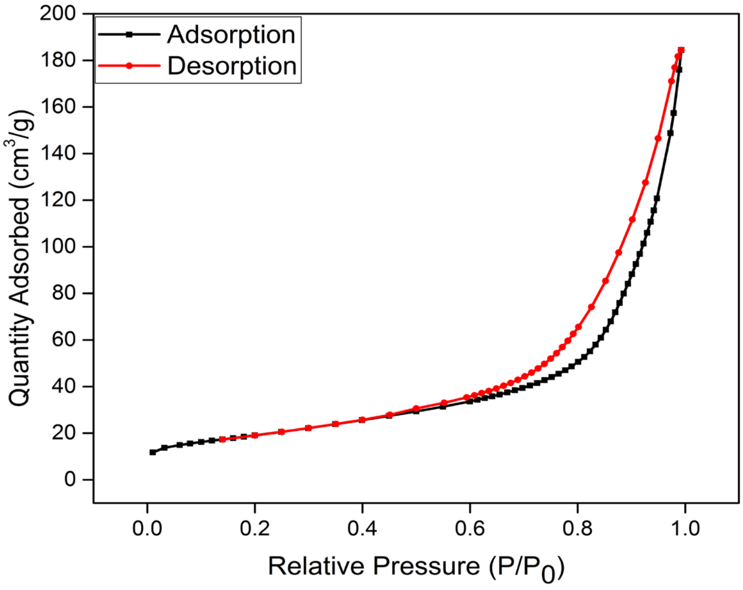

Fig. 4-2 N_2 adsorption-desorption isotherms of halloysite

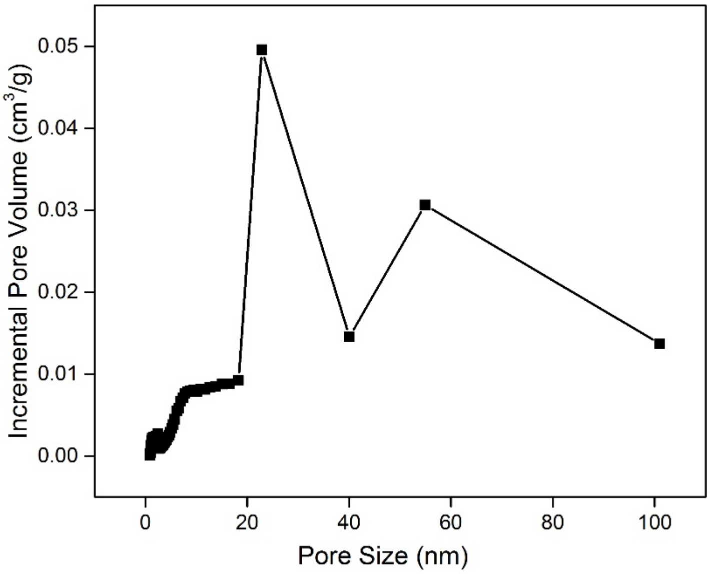

Fig. 4-3 Pore size distribution of halloysite

4.2.2 Halloysite form-stable $Na_2HPO_4 \cdot 12H_2O$ phase change material

70% $Na_2HPO_4 \cdot 12H_2O$ was loaded into halloysite via vacuum impregnation as described in 4.1.2. After the sonication procedure, white homogenous pulpy mixture was obtained. The form of the mixture was remained after the impregnation process. The final sample after drying was obtained as white powder and noted as $Na_2HPO_4 \cdot 12H_2O$@halloysite in the following characterisations. To investigate the loading effect of halloysite on $Na_2HPO_4 \cdot 12H_2O$, the chemical composition of the composite was characterised by FTIR and XRD. The SEM image showed the morphology of the composite. The heat uptake/release was measured by DSC.

Fig. 4-4 shows the FTIR spectrum of $Na_2HPO_4 \cdot 12H_2O$@halloysite composite comparing to that of halloysite and $Na_2HPO_4 \cdot 12H_2O$. The important peak positions are listed in Tab. 4-3. The characteristic peaks at 3625 cm^{-1} and 3694 cm^{-1} due to the stretching vibrations of O-H connected to aluminium ion in halloysite[9] are found in the composite without any shift, indicating the chemical composition of the halloysite does not change in the composite. In the spectrum of $Na_2HPO_4 \cdot 12H_2O$, the broad peak at 3251 cm^{-1} is responded to the O-H stretching of hydrate water molecules, which is also present in the composite as a strong broad peak, showing the water molecules retain well in the composite. The peaks at 1065 cm^{-1} and 981 cm^{-1} from the hydrated salt are resulted from the asymmetric and symmetric stretching vibrations of P-O bonding[10], while the peak at 854 cm^{-1} is from the stretching vibration of P-OH bonding[10] In the composite, a shift of the two peaks from P-O is observed. The new peaks are at 994 cm^{-1} and 905 cm^{-1}. The shift can be attributed to the electrostatic interactions between negatively charged P-O bonds and the positively charged alumina layer in the inner side of halloysite nanotubes. This indicates the hydrated salt is predominantly absorbed inside the halloysite nanotubes. The peak of 854 cm^{-1} from P-OH is found in the composite without shift. In the FTIR spectrum of $Na_2HPO_4 \cdot 12H_2O$@halloysite composite, all characteristic peaks of halloysite and $Na_2HPO_4 \cdot 12H_2O$ are displayed, and no new peaks are found. This could be considered as evidence, that no new covalent chemical bonding is formed between the hydrated salt and halloysite as nanocontainer matrix material.

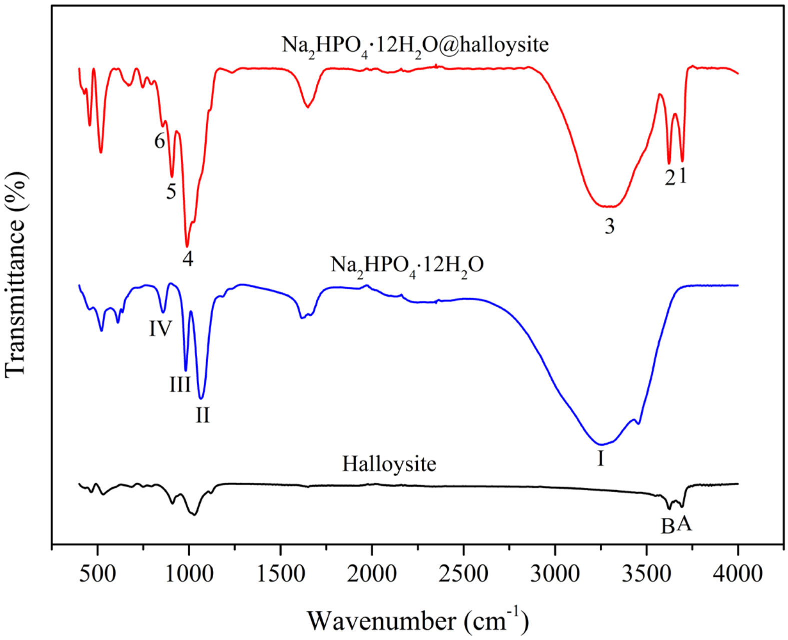

Fig. 4-4 FTIR spectra of halloysite, $Na_2HPO_4\cdot 12H_2O$ and $Na_2HPO_4\cdot 12H_2O$ @halloysite

Tab. 4-3 Tabulation of FTIR spectra transmittance of halloysite[9], $Na_2HPO_4\cdot 12H_2O$[10] and $Na_2HPO_4\cdot 12H_2O$@halloysite

Signal	A	B			
Peak position (cm^{-1})	3694	3625			
Assignment	AlO-H	AlO-H			
Signal	I	II	III	IV	
Peak position (cm^{-1})	3251	1065	981	854	
Assignment	O-H	P-O	P-O	P-OH	
Signal	1	2	3	4	5	6
Peak position (cm^{-1})	3694	3625	3251	994	905	854
Assignment	AlO-H	AlO-H	O-H	P-O	P-O	P-OH

The XRD patterns of halloysite, $Na_2HPO_4 \cdot 12H_2O$@halloysite and $Na_2HPO_4 \cdot 12H_2O$ are shown in Fig. 4-5. Halloysite shows strong reflections at 11.9 °, 19.8 °, 24.8 °, 35.1 °, 38.4 ° and 62.4 °. In the pattern of the $Na_2HPO_4 \cdot 12H_2O$@halloysite composite, these peaks have integrated with the sharp peaks from $Na_2HPO_4 \cdot 12H_2O$. Both the peaks from halloysite and from the hydrated salt are present in the composite. This indicates, the hydrated salts have been successfully loaded into the halloysite, and the crystal structures of PCM and matrix have retained well in the composite. Specifically, the reflection at 11.9 ° is assigned to the multiwall nano-tubular structure of halloysite[11], which is clearly observed in the spectrum of the composite, showing the same tube wall structure of halloysite is preserved.

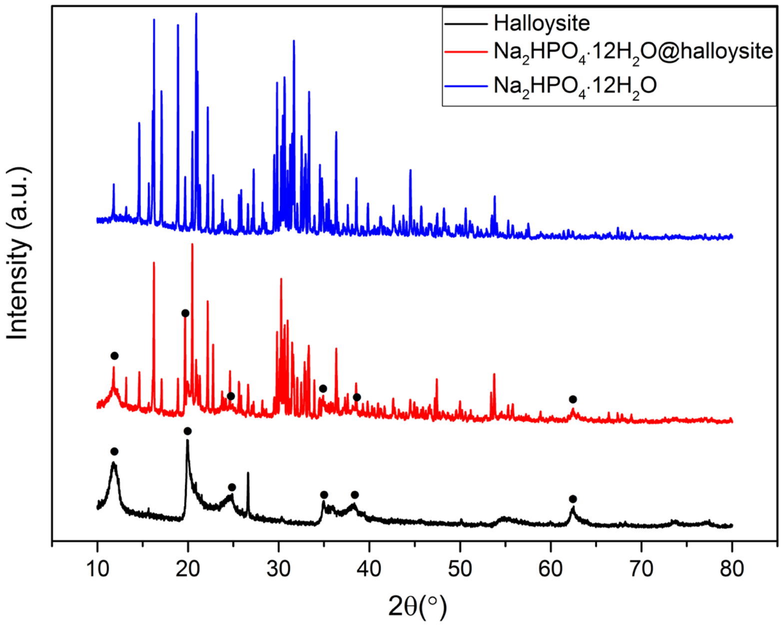

Fig. 4-5 XRD patterns of halloysite, $Na_2HPO_4 \cdot 12H_2O$ and $Na_2HPO_4 \cdot 12H_2O$ @halloysite

The SEM image of $Na_2HPO_4 \cdot 12H_2O$@halloysite is shown in Fig. 4-6. Aggregated nanotubes are observed. No obvious leakage is shown on the surface of the nanotubes. This indicates, the hydrated salt has been largely impregnated into the lumen of halloysite nanotubes.

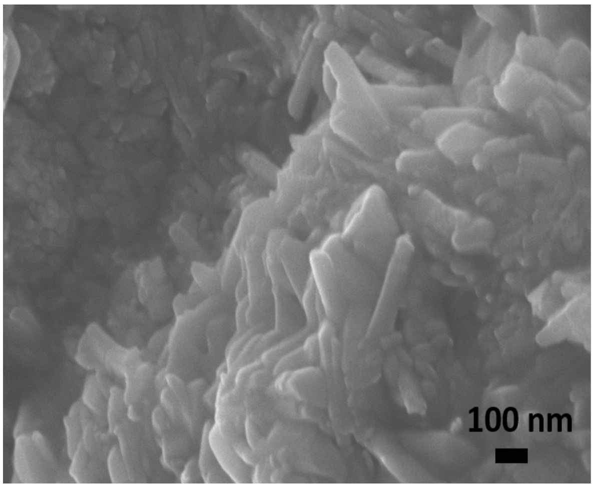

Fig. 4-6 SEM image of $Na_2HPO_4 \cdot 12H_2O$@halloysite

Fig. 4-7 displays the phase change behaviours of pure $Na_2HPO_4 \cdot 12H_2O$ and $Na_2HPO_4 \cdot 12H_2O$@halloysite. The melting curve of the hydrated salt shows strong phase separation with two main melting peaks at 42.6 °C and 51.9 °C. The first peak is due to the melting of $Na_2HPO_4 \cdot 12H_2O$[12], while the peak at 51.9 °C appears from the melting of $Na_2HPO_4 \cdot 7H_2O$[13]. In comparison, the $Na_2HPO_4 \cdot 12H_2O$@halloysite has a main peak at 42.4 °C from the melting of $Na_2HPO_4 \cdot 12H_2O$ and a small shoulder peak at 47.6 °C. The composite shows a smaller melting temperature range than the pure $Na_2HPO_4 \cdot 12H_2O$. The splitting of the melting peak is much weaker, confirming the phase separation of $Na_2HPO_4 \cdot 12H_2O$ has been clearly reduced in the halloysite nanocontainer composite. This could result from the nano-confinement effect of halloysite nanotubes. The diffusion of the hydrated salts is accelerated inside nanosized halloysite lumen[14]–[17], leading to homogenization during the melting.

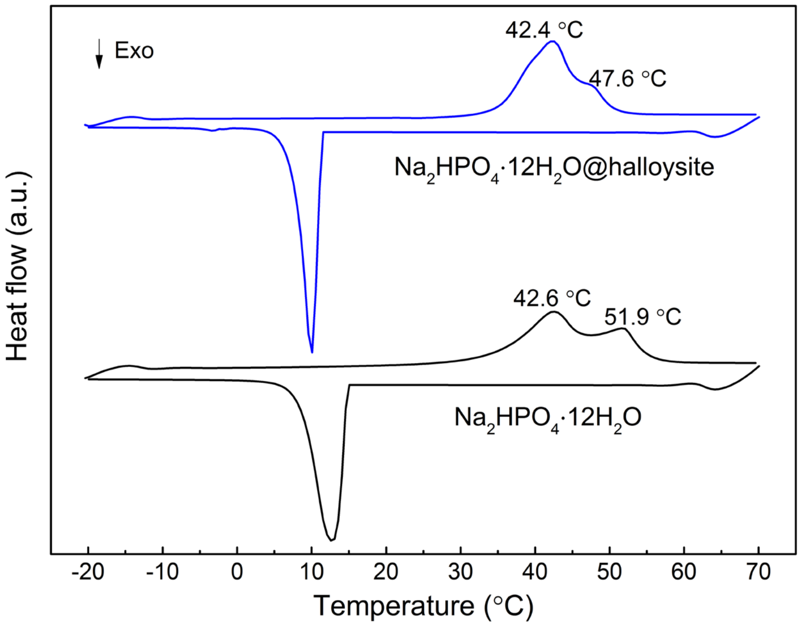

Fig. 4-7 DSC curves of $Na_2HPO_4·12H_2O$ and $Na_2HPO_4·12H_2O$@halloysite

Further, to obtain a hydrated salts@halloysite composite with the phase separation eliminated, a mixture of $Na_2HPO_4·12H_2O$ and $Na_2SO_4·10H_2O$ was loaded to halloysite, as discussed in 4.2.3.

4.2.3 Halloysite form-stable eutectic hydrated salt phase change material

4.2.3.1 Compositions

Series of PCM@halloysite composites with pure $Na_2HPO_4·12H_2O$ (DHPD), mixture of $Na_2HPO_4·12H_2O$ and $Na_2SO_4·10H_2O$ (SDH) with mass ratios of 3:1, 1:1 and 1:3 as well as pure $Na_2SO_4·10H_2O$ as PCM were prepared as described in 4.1.2.

Fig. 4-8 displays the melting behaviour of PCM@halloysite nanocontainer composite with different mass ratios of DHPD to SDH. Hydrated salts mixture@halloysite show different melting temperature as compared to pure DHPD@halloysite and SDH@halloysite. The 3DHPD:1SDH@halloysite have separation of two melting peaks. The one at 35 °C is caused by the melting of the eutectic mixture, while the one at

46.9 °C could be attributed to the phase separation of the DHPD excess. As the ratio of SDH increases to 1DHPD:1SDH, only one melting peak at 35.8 °C is present, which is the eutectic point of the mixture. The melting enthalpy is 142 J·g^{-1}. 1DHPD:3SDH@halloysite also shows one melting peak at 35.7 °C, and the melting enthalpy is 124 J·g^{-1}. The melting peak from the eutectic mixtures and the one from SDH excess could fuse together to form one broad peak. The lower melting enthalpy compared to 1DHPD:1SDH@halloysite should be attributed to the excess amount of SDH. For further investigation of the optimum loading in halloysite, the eutectic hydrated salt mixture 1DHPD:1SDH is selected.

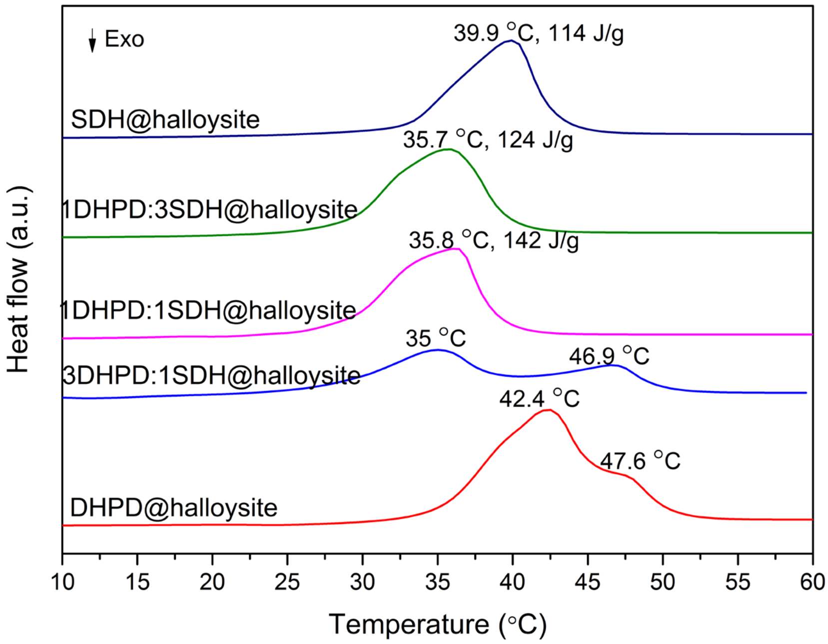

Fig. 4-8 DSC melting curves of different mass ratios of $Na_2HPO_4 \cdot 12H_2O$ (DHPD) to $Na_2SO_4 \cdot 10H_2O$ (SDH)

The phase change behaviour of 1DHPD:1SDH@halloysite is compared with the pure hydrated salts mixture 1DHPD:1SDH in Fig. 4-9. The nano-confinement effect of halloysite on the hydrated salts PCM embodies in the change of melting temperature. The nanocontainer composite exhibits a slightly lower melting peak at 35.8 °C than the melting peak of hydrated salts mixture at 38.5 °C. As the surface energy of PCM increases in nanotubes, its melting temperature decreases accordingly [18]–[20].

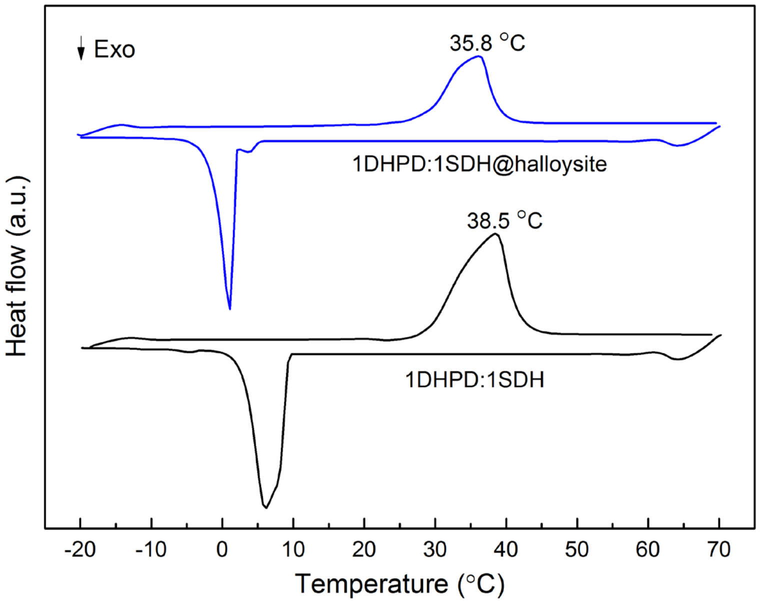

Fig. 4-9 DSC curves of EHS (1DHPD:1SDH) and EHS@halloysite

4.2.3.2 Loadings

Regarding different starting loading percentage of PCM, the melting behaviour of composite is shown in Fig. 4-10, including correspondent melting point and melting enthalpy. All the composites consist of eutectic hydrated salt (EHS) with 1DHPD:1SDH mass ratio and have a consistent single melting peak at about 36 °C. The melting enthalpy of the composite increases with the loading percentage of EHS. Further, by comparing the increment of melting enthalpy per 1% mass ratio increase of loading, it should be noticed that from 58% to 70% the rate is 3.6 $J\cdot g^{-1}\cdot\%^{-1}$, which is much higher than the one from 70% to 82% (1.9 $J\cdot g^{-1}\cdot\%^{-1}$), and from 82% to 88% (1.8 $J\cdot g^{-1}\cdot\%^{-1}$). The hydrated salts loaded into the halloysite nanotubes can retain latent heat enthalpy much better than the ones absorbed on the surface or even not attached to halloysite, as the confined nanotube volume prevent the degradation of hydrated salts. Correspondently, the hydrated salts from 58% to 70% are loaded inside halloysite nanotubes, while increased PCM content from 70% to 88% should locate largely outside halloysite nanotubes. The much smaller increasing rates of the melting enthalpy indicates the formation of PCM aggregates outside halloyiste nanotube lumen over 70%.

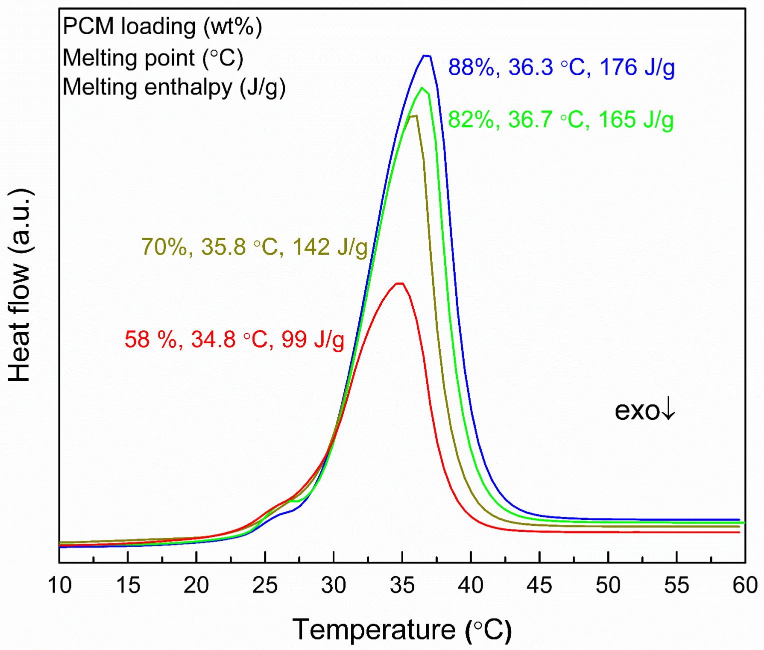

Fig. 4-10 DSC melting curves of EHS@halloysite with various loadings of EHS as PCM

The SEM images of halloysite and EHS@halloysite nanocontainer composites with different loading are illustrated in Fig. 4-11. Halloysite has the form of nanotubes (Fig. 4-11a), with an average outer diameter of 70 nm. The dominant morphologies are long tubes with the length from 800 nm to 1 µm, although some short tubes below 200 nm are observed. With 58% of loaded hydrated salts (Fig. 4-11b), the composite shows similar morphology as unloaded halloysite. Separated nanotubes can be observed. The ends of most nanotubes are blocked with loaded hydrated salts. Composite with 70% loading (Fig. 4-11c) also maintains the nanotubular morphology with increased number of the aggregates. When the loading rises to 82% (Fig. 4-11d), some irregular block material is observed besides the nanotube aggregates, indicating existence of hydrated salts crystals outside nanotubes. For the sample with 88% PCM content (Fig. 4-11e), more irregular block material randomly appeared among or on the surface of nanotubes, showing oversaturation of the loading.

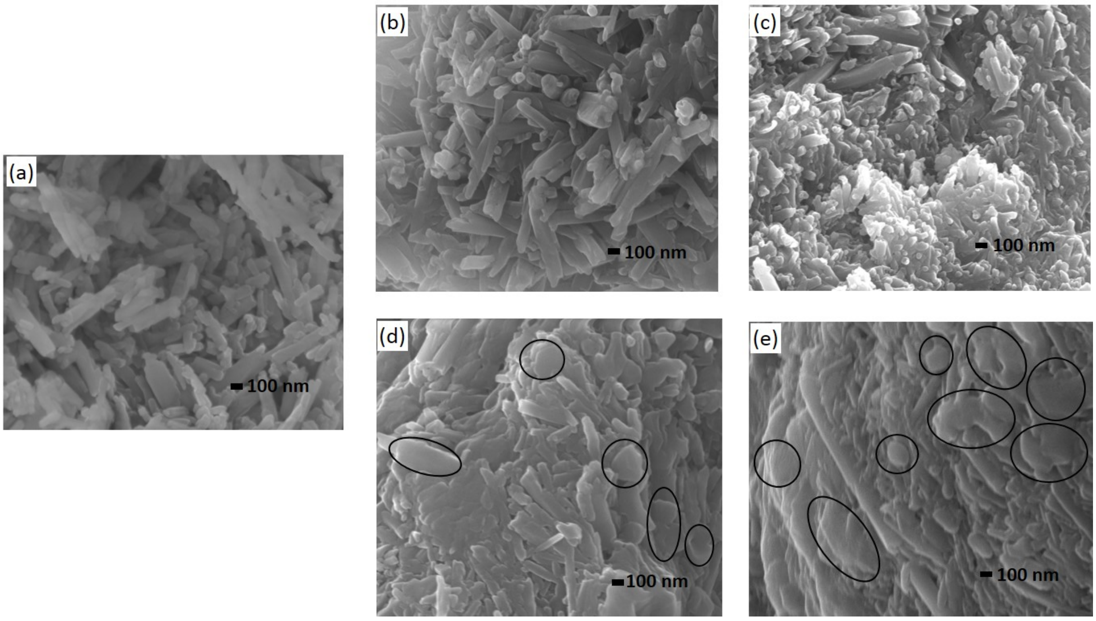

Fig. 4-11 SEM images of (a) halloysite (b) 58% (c) 70% (d) 82% (e) 88% EHS@ halloysite (Circles indicate unloaded PCMs)

To determine the optimum PCM loading into halloysite nanocontainers, thermal cycling tests of samples with 58%, 70%, 82% and 88% loading were carried out. Changes of the melting enthalpy in the heat uptake/release cycles are displayed in Fig. 4-12. At 88% loading, the melting enthalpy decreases rapidly after 10 cycles and the decrement reaches 52% after 33 cycles. Composite with 82% of hydrated salts is relatively stable for 33 cycles, and start to degrade after that. The melting enthalpy reduces by 43% after 50 cycles. On the contrary, the one with 70% loading shows the best thermal stability. The melting enthalpy change is only 7% after 50 cycles. Sample with 58% loading also shows stability for 50 cycles, but the melting enthalpy is much lower than that of the 70%. So the 70% sample was used for further characterisations in this chapter.

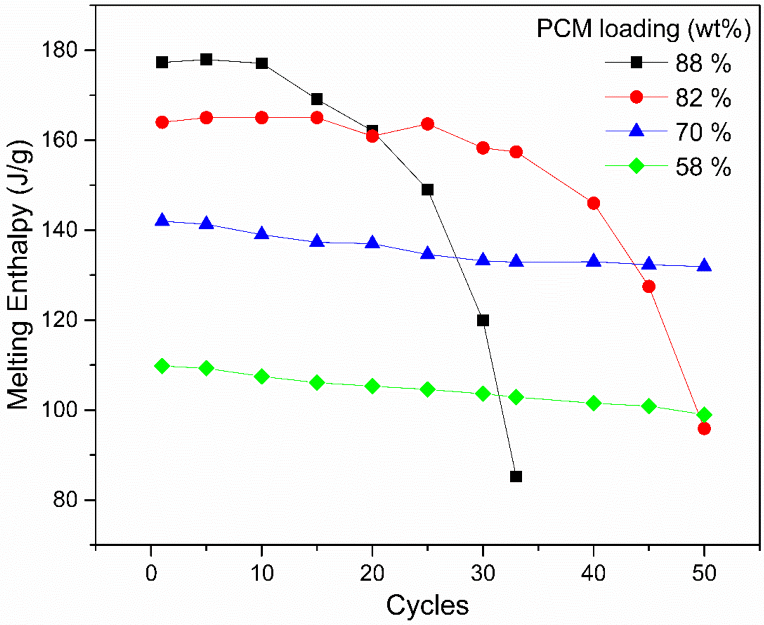

Fig. 4-12 Melting enthalpies of EHS@halloysite with various loading vs. number of heat uptake cycles

4.2.3.3 Structural characterisation

Fig. 4-13a shows the TEM images of halloysite. They are hollow nanotubes with average inner diameter of 30 nm, and the average shell thickness of 20 nm. The average outer diameter is 70 nm, and the tube length ranges from 200 nm to 1 µm, in accordance with the observations from the SEM images (Fig. 4-11a). The EDS measurement detected Si, Al, O elements in pure halloysite (Fig. 4-13b). This corresponds to the unit formula for halloysite as $Al_2Si_2O_5(OH)_4$[2]. The TEM images of crystallohydrates loaded halloysite are displayed in Fig. 4-13c. The inner lumen of the halloysite nanotubes is filled with hydrated salts. The EDS spectrum from Fig. 4-13d shows the presence of P, S, Na elements in the composite, which appear from the crystallohydrates. Combining the observation from the TEM images and the EDS measurement, it can be confirmed that hydrated salts mixture is located inside HNTs in the EDS@halloysite nanocontainer composite.

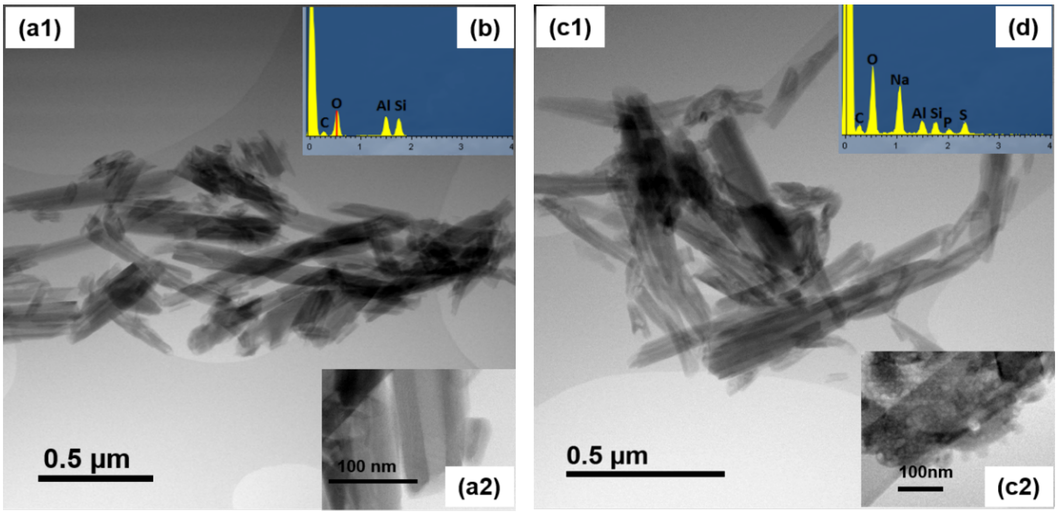

Fig. 4-13 TEM images (collected from technician) of (a) halloysite (c) 70% EHS@halloysite , EDS spectra of (b) halloysite (d) 70% EHS@halloysite

The FTIR spectra of halloysite, EHS@halloysite and pure EHS (1DHPD:1SDH) are displayed in Fig. 4-14. The important peak positions are displayed in Tab. 4-4. The characteristic absorption peaks at 3625 cm^{-1} and 3694 cm^{-1} from the stretching vibrations of O-H connected to aluminium ion in halloysite[9] are also present in EHS@halloysite without shift, indicating the chemical composition of the halloysite does not change in the composite.

In the spectrum of the hydrated salts mixture, the strong broad peak at 3341 cm^{-1} is from the O-H stretching of hydrate water. This peak is also observed in EHS@halloysite, indicating the hydrate water molecules from the PCM are well kept in the composite. The peaks at 1077 cm^{-1} and 985 cm^{-1} from the hydrated salts are due to the asymmetric and symmetric vibration of P-O bonding[10], while the peak at 861 cm^{-1} is form the stretching vibration of P-OH bonding[10], and the peak at 618 cm^{-1} is assigned to the asymmetric bending vibration of S-O bonding[21].

In the composite, the typical peaks from S-O and P-OH are detected at the same wavenumbers as for the hydrated salts mixture. However, both peaks of P-O bond show a shift from 1077 cm^{-1} to 998 cm^{-1} and from 985 cm^{-1} to 908 cm^{-1}, which can be attributed to the electrostatic interactions between negatively charged P-O bonds and positively charged alumina layer in the lumen of halloysite nanotubes. This explains hydrated salts are predominantly absorbed inside positively charged alumina inner space, but not on the negatively charged silica outer surface of halloysite. The stretching vibration of the alumina layer is not influenced by the weak electrostatic interaction from the hydrated salts, which should be due to the strong network structure in the layer. In the FTIR spectra, all characteristic peaks of halloysite and hydrated salts mixture are displayed, and no new peaks are found. This could be considered as evidence, that no new covalent chemical bonding is formed between hydrated salts and halloysite as nanocontainer material.

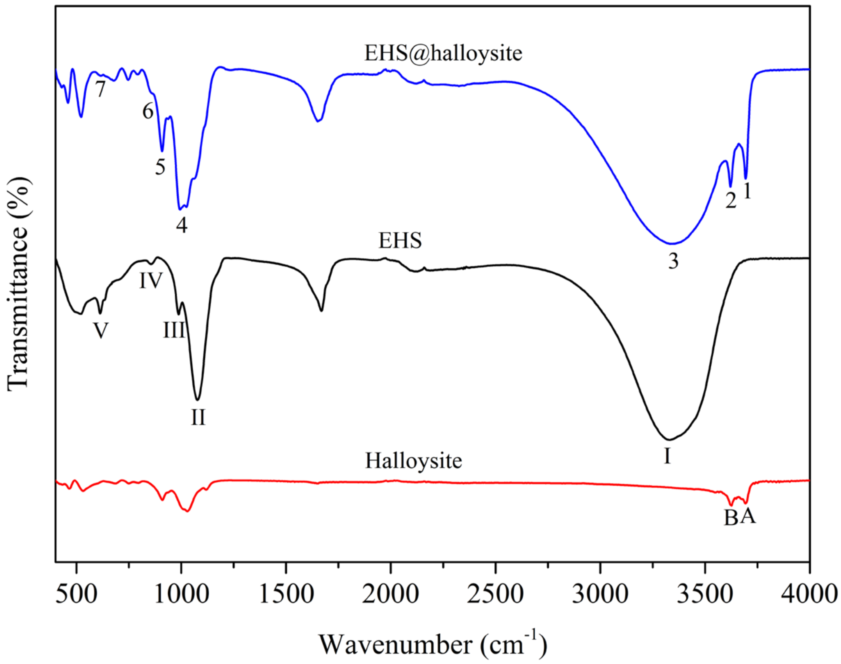

Fig. 4-14 FTIR spectra of halloysite, EHS and EHS@halloysite

Tab. 4-4 Tabulation of FTIR spectra transmittance of halloysite[9], EHS[10][21] and EHS@halloysite

Signal	A	B					
Peak position (cm^{-1})	3694	3625					
Assignment	AlO-H	AlO-H					
Signal	I	II	III	IV	V		
Peak position (cm^{-1})	3341	1077	985	861	618		
Assignment	O-H	P-O	P-O	P-OH	S-O		
Signal	1	2	3	4	5	6	7
Peak position (cm^{-1})	3694	3625	3341	998	908	861	618
Assignment	AlO-H	AlO-H	O-H	P-O	P-O	P-OH	S-O

Fig. 4-15 shows the comparison of the XRD patterns from the EHS@halloysite nanocontainer composite, halloysite and EHS. Halloysite exhibit a characteristic reflection at 11.9 °, which is assigned to the multiwall nano-tubular structure[11]. The same diffraction peak is observed in the XRD pattern of EHS@halloysite, indicating the same tube wall structure of halloysite is preserved in the nanocontainer composite. Other reflections at 26.4 °, 24.8 ° and 19.8 ° from halloysite have also been found in the nanocontainer composite. The diffraction peaks of hydrated salts mixture are also observed in the same place in the nanocontainer composite, confirming the presence of the hydrated salts mixture and the maintenance of their crystal structures in the nanocontainer composite. Moreover, the nanocontainer composite after heating to 60 °C and cooling shows the same XRD pattern as the sample before heating. It demonstrates the crystal structure of the nanocontainer composite sample does not change during heating.

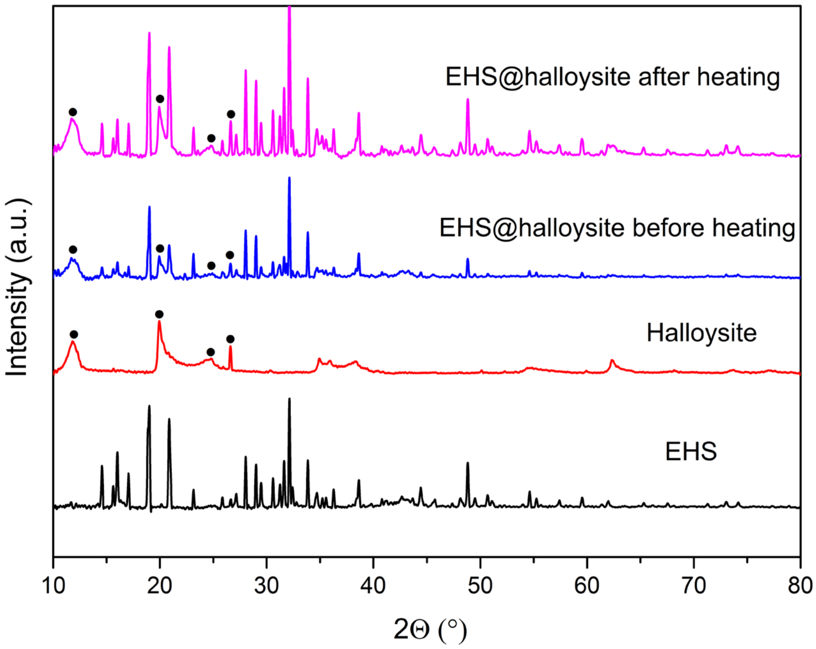

Fig. 4-15 XRD patterns of EHS, halloysite, EHS@halloysite before and after heating at 60 ˚C

4.2.3.4 Stability and cycling properties

The stability of encapsulated EHS during heating/cooling cycles can be visually seen in Fig. 4-16, where images of EHS and encapsulated EHS nanocontainer composite before and after heating at 60 ˚C are displayed. The melting temperature of hydrated salts mixture is about 36 ˚C. While the water leakage is obvious for pure hydrated salts mixture, the EHS-loaded nanocontainers keep a stable powder form and no liquid leakage is observed after heating to 60 ˚C. This observation is in accordance with the XRD characterisation in Fig. 4-15.

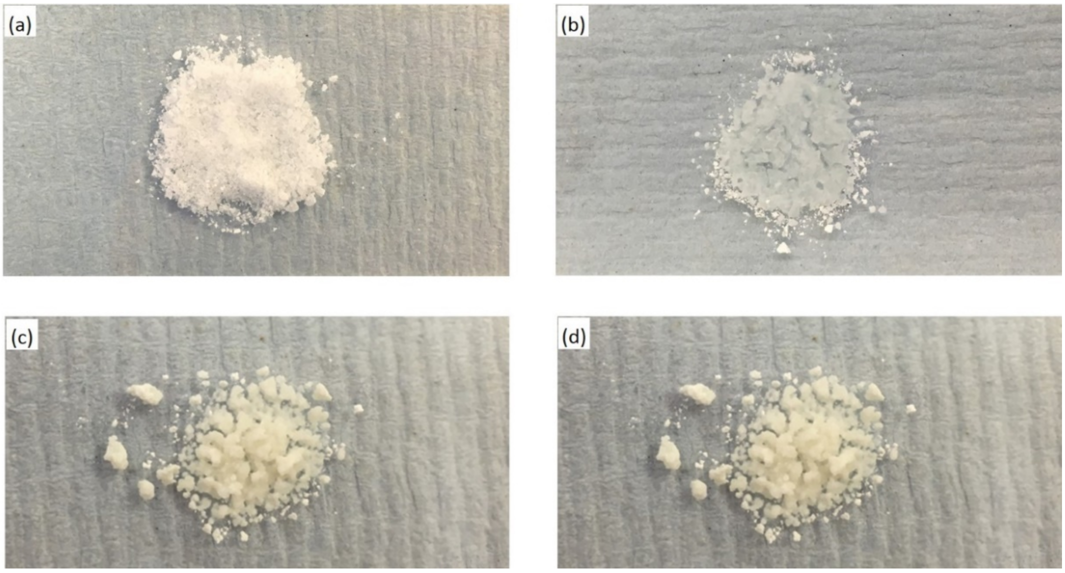

Fig. 4-16 Photos of (a) EHS before and (b) after heating, (c) EHS@halloysite before and (d) after heating at 60 ˚C

The DSC curves of EHS and EHS@halloystite nanocontainer composite during 50 melting/freezing cycles are displayed in Fig. 4-17. The summary of the correspondent DSC data can be seen in Tab. 4-5. EHS has a melting point of 38.5 °C and melting enthalpy of 211 $J \cdot g^{-1}$ during the first cycle. It shows a certain stability for the first twenty cycles due to the eutectic effect. After 20 cycles, the down shift of melting temperature becomes more evident and the melting enthalpy reduces rapidly with increasing cycle number. The melting point shift reaches 2.3 °C and the melting enthalpy reduces by 21 $J \cdot g^{-1}$ after 30 cycles, following 5.3 °C and 83 $J \cdot g^{-1}$ reduction after 50 cycles, which takes over 39.3% of the original melting enthalpy.

EHS@halloysite nanocontainer composite exhibits a melting point of 35.8 °C, which is lower than the pure EHS. The melting enthalpy is 67% of EHS. Since halloysite does not have melting behaviour, the effective loading yield of the composite can thus be calculated as 67% [22]. It is similar to the starting loading percentage of 70%. The eutectic hydrated salt keeps its melting enthalpy efficiently in the composite after the halloysite loading and drying. The composite demonstrates better thermal stability than pure hydrated salts mixture in heat uptake/release cycles. The melting temperature shift is only 0.9 °C, and the melting enthalpy decrease is 10 $J \cdot g^{-1}$ after 50 cycles, which is only 7% of the starting value. The nano-confinement effect from halloysite nanotubes evidently inhibits phase separation and PCM degradation during thermal cycling.

However, further increase of the number of cycles to 100 lead to the decrease of the enthalpy of EHS@halloysite composite, as shown in Fig. 4-18. The DSC data is summarized in supplements Tab. S4-7. This is resulted from the open ends of the halloysite nanotubes and natural defects of the halloysite walls, from which small leak of water occurs. The degraded nanocontainer composite material after 100 cycles could be regenerated by adding small amount of water.

Turbulence in freezing temperature is observed for both EHS and nanocontainer composite during cycling. This could be attributed to the slow nucleation process for crystallohydrate PCMs. The hydrated salts mixture starts to nucleate at slightly different temperature during each cycle, and the process of heat release does not have a uniform rate for all nanotubes because of their difference in length, so the freezing peak can vary between 1 to 6 °C. It should be also noticed, the freezing enthalpy of the pure hydrated salts mixture decreases rapidly after 50 cycles, which is due to the phase separation effect[23]. In comparison, the freezing enthalpy of the nanocontainer composite does not show obvious change during cycling. This proves again the phase separation is eliminated inside halloysite nanocontainer composite. It is assumed, that a relatively ordered crystal structure could be generated repeatedly within a confined space of halloysite lumen.

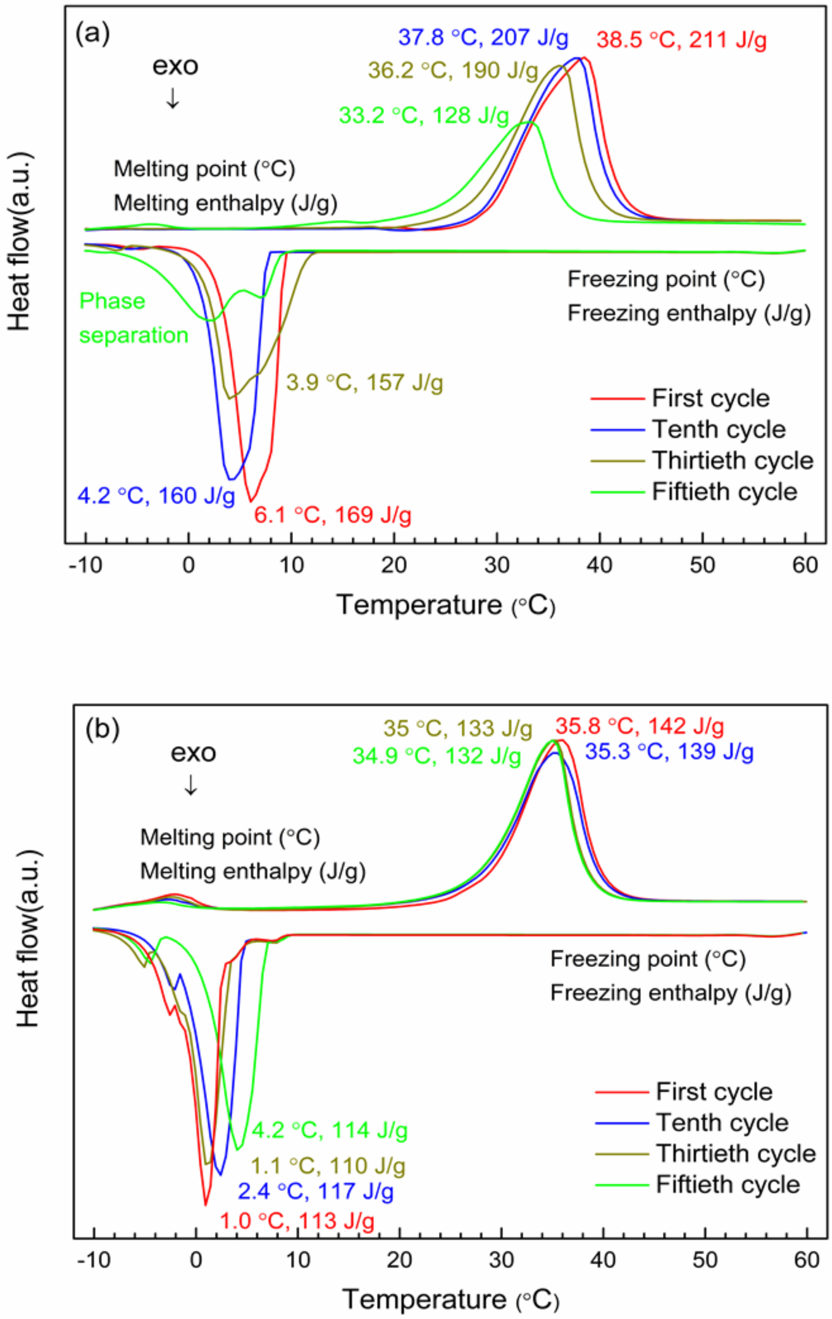

Fig. 4-17 Thermal cycling tests of (a) EHS for 50 cycles, (b) EHS@halloysite for 50 cycles

Tab. 4-5 DSC data from cycling tests of (a) EHS (b) EHS@halloysite

Cycle Nr.	Melting T (°C)	Melting Enthalpy ($J \cdot g^{-1}$)	Freezing T (°C)	Freezing Enthalpy ($J \cdot g^{-1}$)
1	38.5	211	6.1	169
10	37.8	207	4.2	160
20	37	202	5	163
30	36.2	190	3.9	157
40	34.6	169	3.9	136
50	33.2	128	Phase separation	n/a

(a)

Cycle Nr.	Melting T (°C)	Melting Enthalpy ($J \cdot g^{-1}$)	Freezing T (°C)	Freezing Enthalpy ($J \cdot g^{-1}$)
1	35.8	142	1	113
10	35.3	139	2.4	117
20	35.3	137	3.2	116
30	35	133	1.1	110
40	35	133	3	113
50	34.9	132	4.2	114

(b)

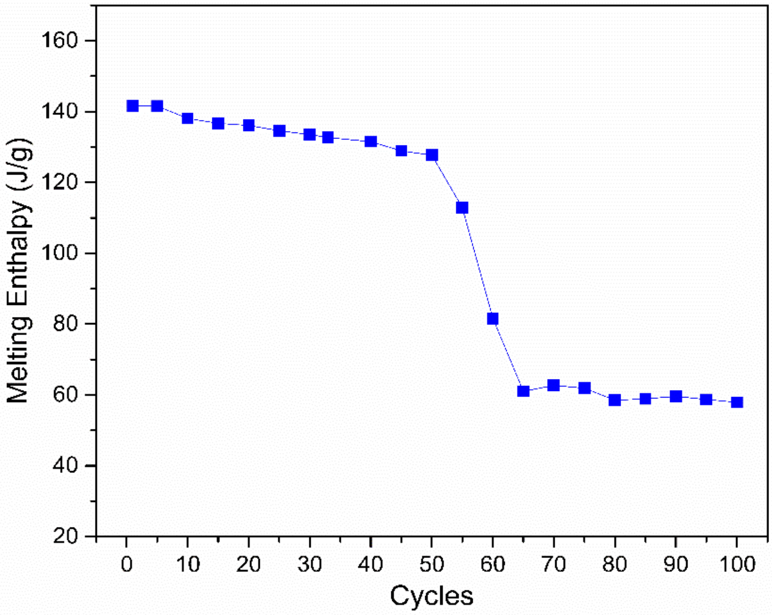

Fig. 4-18 Melting enthalpies of EHS@halloysite at 70% loading vs. number of heat uptake/release cycles

In conclusion, the hydrated salts mixture of DHPD and SDH in 1:1 mass ratio was loaded into halloysite to form EHS@halloysite nanocontainer composite. The composite sample with original 70% loading shows an effective loading of 67%, with the melting temperature of 35.8 ˚C and the melting enthalpy of 142 $J \cdot g^{-1}$. The EHS as PCM was impregnated into the lumen of halloysite nanotubes. The chemical composition and crystal structure of PCM retains well in halloysite. No new covalent bonding is formed between PCM and halloysite in the composite. Due to the electronic interaction between PCM and the inner space of halloysite as well as the nanoconfinement effect, the PCM was kept well in the halloysite nanocotainers and shows no leakage over the solid-liquid phase transformation. Further, the thermal cycling tests demonstrate, the 67% EHS@halloysite composite is thermal stable and shows no phase separation for 50 cycles. In the next section, improvement of EHS@halloysite system regarding to reduction of the supercooling extent by adding nucleating agent is discussed.

4.2.4 Addition of borax

Borax ($Na_2B_4O_7$) is a commonly used nucleating agent to decrease the supercooling degree of hydrated salts[24][25]. Samples with different mass ratios of borax mixed in the EHS in the beginning were prepared as the procedure described in 4.1.2. The effect of borax as nucleating agent on EHS@halloysite composites is evaluated by DSC characterisation, as shown in Fig. 4-19. The data of melting and freezing temperatures are summarised in Tab. 4-6.

On addition of borax, the melting peak temperature and melting enthalpy of EHS@halloysite are barely changed. The melting peak of samples with borax is slightly slimmer comparing to the melting peak of the composite without borax, as the melting end temperature is 1 - 2.5 ˚C lower. No phase separation in melting curves is observed by samples with borax.

The freezing behaviours of EHS@halloysite with borax are different from the pure composite. The freezing of composite starts 7 ˚C -11 ˚C earlier in the presence of borax. Also the freezing enthalpy has increased about 10% by adding borax. This demonstrates, the addition of borax as nucleating agent can decrease the supercooling extent of EHS@halloysite in some degree. Sample with 2% borax shows less supercooling than sample with 1% borax. The increase of borax to 3% does not improve the melting/freezing behaviour further. Despite increasing of the freezing start temperature, samples with borax show more serious phase separation of freezing peak. While EHS@halloysite has only one freezing peak with a neglectable small shoulder, sample with 1% borax shows two separated freezing peaks at 0.5 ˚C and 9.5 ˚C, sample with 2% borax shows two big freezing peaks at 8.2 ˚C and 11.2 ˚C, sample with 3% borax shows a similar freezing pattern as with 2% borax. The phase separation of freezing peaks is not favoured for the application of PCM and could influence the cycling stability of the composite, so the addition of borax should not be considered as an effective option to improve phase change properties of EHS@halloysite.

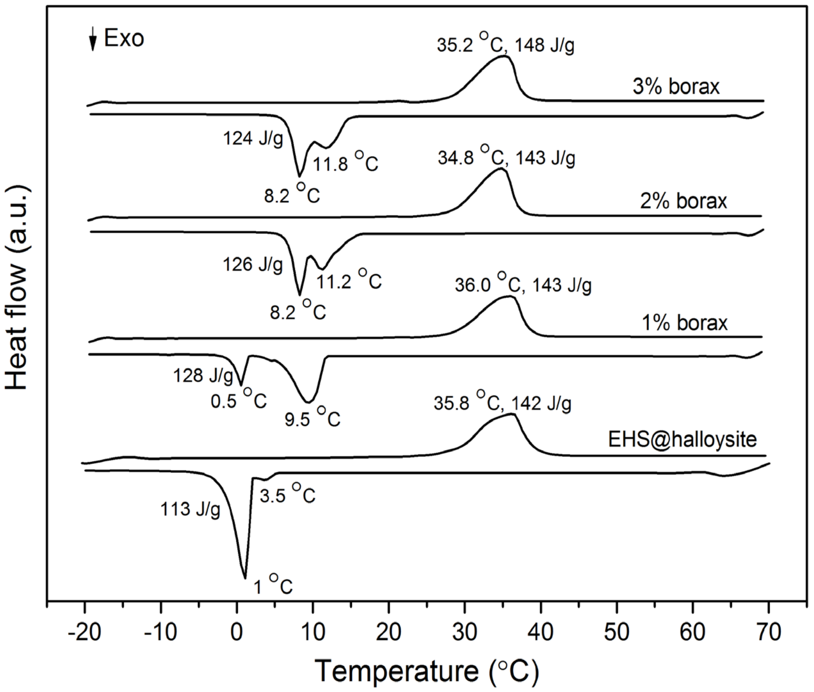

Fig. 4-19 DSC curves of pure EHS@halloysite, EHS@halloysite with 1%, 2% and 3% borax

Tab. 4-6 Melting and freezing T of pure EHS@halloysite, EHS@halloysite with 1%, 2% and 3% borax

Sample	**Melting Start T_s(˚C)**	**Melting End T_e(˚C)**	**Melting Peak T_p(˚C)**	**Freezing Start T_s(˚C)**	**Freezing End T_e(˚C)**	**Freezing Peak T_p(˚C)**
EHS@halloysite	26	41	35.8	5.6	-5.4	1
1% borax	26.5	40	36	12.5	-3	9.5; 0.5
2% borax	26.4	38.5	34.8	16.7	3.7	8.2; 11.2
3% borax	25.8	39.3	35.2	15.2	4.7	8.2; 11.8

4.3 Conclusions

In this study, a eutectic crystallohydrate PCM@halloysite nanocontainer composite system was fabricated to eliminate the phase separation of crystallohydrates as phase change materials as well as to improve their thermal stability over phase change cycling. The mixture of $Na_2HPO_4 \cdot 12H_2O$ (DHPD) and $Na_2SO_4 \cdot 10H_2O$ (SDH) was selected as crystallohydrate PCM because of their ability to form stable eutectic hydrated salt with low melting temperature (<40°C) suitable for domestic heat range. Halloysite as nanocontainer has the advantages of low-cost and easy accessibility. They have long nanotubular morphology with the average inner diameter of 30 nm, the average shell thickness of 20 nm and the tube length ranging from 200 nm to 1 μm. This provides nano-confinement effect on the loaded crystallohydrate PCMs, which can be proven by the improved phase change performance and cycling stability. Meanwhile, the proper ratio of inner diameter to shell thickness endows halloysite as nanocontainers high loading capacity as well as structural stability. Due to the vacuum impregnation process and the electrostatic interaction between Al-OH from the inner alumina layer and P-O from eutectic hydrated salt mixture, PCMs were successfully encapsulated into the lumen of halloysite. The composite with 67% efficient loading of DHPD and SDH in 1:1 mass ratio exhibits no phase separation during heat uptake/release. Its melting temperature retains around 35 °C and the melting enthalpy decreases only by 7% from 142 $J \cdot g^{-1}$ to 132 $J \cdot g^{-1}$ after 50 cycles. However, the further thermal cycling reduced latent heat capacity of the composites due to the water loss through the uncoated edges and natural defects of the halloysite. The heat capacity can be restored by adding small amount of water to the halloysite composites.

The structural characterisation shows the crystallohydrates in halloysite nanocontainer composite have the same IR and XRD pattern as their pure form and no new chemical bonding is formed between crystallohydrates and halloysite. During the heating to 60 °C, the morphology of the nanocontainer composite keeps stable and its crystalline structure remains unchanged after cooling. In general, the encapsulation of eutectic crystallohydrates in HNTs as nanocontainers can be considered as effective strategy to address two common problems when inorganic crystallohydrates are used as PCMs for thermal energy storage, namely the phase separation and poor cycling stability. The employment of the halloysite with low cost and easy accessibility as supporting nanomaterial, the simple fabrication process, as well as the non-toxic property of all chemicals included in the composite, make the PCM@halloysite nanocontainer composite system economically efficient and environment-friendly. The proper melting temperature together with high melting enthalpy render the system big potential for latent heat storage in low temperature range. However, the further improvement of the EHS@halloysite system by adding borax was not effective, as the supercooling degree is not eliminated and phase separation occurs in the freezing curve.

Supplements

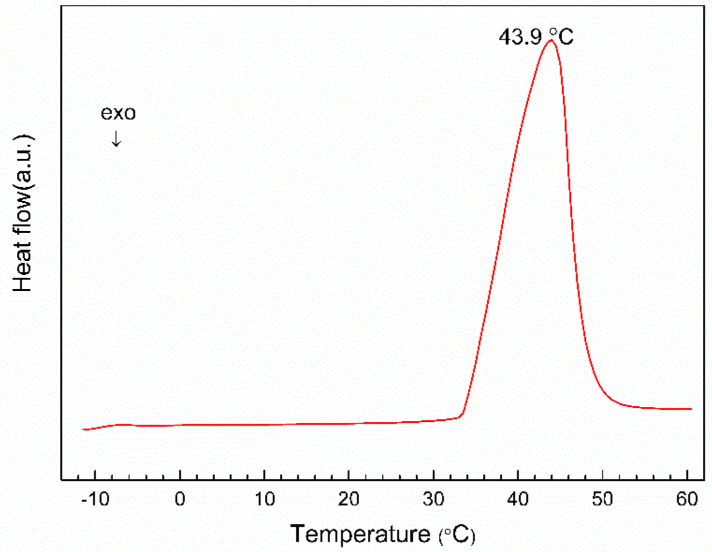

Fig. S4-1 The melting curve of pure SDH

Tab. S4-1 DSC melting points of DHPD vs. DHPD@halloysite and (1DHPD:1SDH) vs. 1DHPD:1SDH@halloysite

Sample	Melting point (°C)	Sample	Melting point (°C)
DHPD	42.6	DHPD@halloysite	42.4
	51.9		47.6
1DHPD:1SDH	38.5	1DHPD:1SDH@halloysie	35.8

Tab. S4-2 DSC melting properties of hydrated salts@halloysite with different mass ratios of DHPD to SDH

DHPD:SDH (mass ratio)	Melting Curve (number of melting peaks)	Melting Point (°C)	Melting Enthalpy ($J \cdot g^{-1}$)
1:0	Two	42.4 and 47.6	n/a
3:1	Two	35 and 46.9	n/a
1:1	One	35.8	142
1:3	One	35.7	124
0:1	One	39.9	114

Tab. S4-3 DSC data from cycling tests of 58% EHS@halloysite for 50 cycles

Cycle Nr.	Melting T (°C)	Melting Enthalpy ($J \cdot g^{-1}$)	Freezing T (°C)	Freezing Enthalpy ($J \cdot g^{-1}$)
1	35	109.8	4.3	86
5	34.8	109.3	3.9	90.2
10	34.6	107.5	3	84.1
15	34.2	106.1	4	93.6
20	34.1	105.3	2.7	83.3
25	34.2	104.6	1.1	84
30	34	103.6	1.7	85.3
33	34	102.9	1	80.8
40	34	101.5	2.8	76.5
45	33.9	100.9	6.2	78.8
50	33.7	99	4.3	77.6

Tab. S4-4 DSC data from cycling tests of 70% EHS@halloysite for 50 cycles

Cycle Nr.	Melting T (°C)	Melting Enthalpy ($J \cdot g^{-1}$)	Freezing T (°C)	Freezing Enthalpy ($J \cdot g^{-1}$)
1	35.8	142	0.5	111
5	35.5	141.3	-0.2	110
10	35.3	139	-0.6	110.8
15	35.4	137.3	-0.8	109.1
20	35.3	137	-1.2	108.5
25	35.2	134.6	-1	108.1
30	35.2	133.2	-0.8	105.3
33	35.1	132.9	2.1	113.6
40	35	133	3.0	108
45	34.8	132.3	4.2	110.3
50	34.4	131.9	5.2	108.6

Tab. S4-5 DSC data from cycling tests of 82% EHS@halloysite for 50 cycles

Cycle Nr.	Melting T (°C)	Melting Enthalpy ($J \cdot g^{-1}$)	Freezing T (°C)	Freezing Enthalpy ($J \cdot g^{-1}$)
1	36.7	164	0.9	134.2
5	36.6	165	2	134.7
10	36.5	165	4.4	140.8
15	36.4	165	3.6	138
20	36.4	160.9	4.9	140
25	36.2	160.6	4.5	139.6
30	36	158.3	3.4	135.1
33	35.8	157.4	4.9	134.3
40	34.5	146	6.1	127.4
45	33.1	127.5	6.9	112.8
50	31.5	95.9	0.4	88.8

Tab. S4-6 DSC data from cycling tests of 88% EHS@halloysite for 33 cycles

Cycle Nr.	Melting T (°C)	Melting Enthalpy ($J\cdot g^{-1}$)	Freezing T (°C)	Freezing Enthalpy ($J\cdot g^{-1}$)
1	36.3	177.3	1.3	144
5	36	177.9	2.2	147
10	35.5	177.1	0.9	143
15	35.4	169.1	2	146.9
20	34.8	162.1	5.5	147.7
25	33.9	149	6.2	137.2
30	32.5	119.9	5.8	115
33	31.7	85.2	-1.7	81.6

Tab. S4-7 DSC data from cycling tests of 70% EHS@halloysite up to 100 cycles

Cycle Nr.	Melting T (°C)	Melting Enthalpy ($J \cdot g^{-1}$)	Freezing T (°C)	Freezing Enthalpy ($J \cdot g^{-1}$)
1	35.8	142	0.7	112
10	35	138	0	118
20	35	136	4	116
30	34.8	134	0.3	110
40	34.6	132	2.1	111
50	34.4	128	4.9	113
55	32.4	113	4.5	103
60	31	82	-1.8	48
65	31.8	61	-12.6	35
70	32.2	62.7	-7.6	50.8
80	33.8	58.5	-5.7	49.7
90	33.6	59.6	-5.9	44.7
100	34	57.9	-2.8	46.1

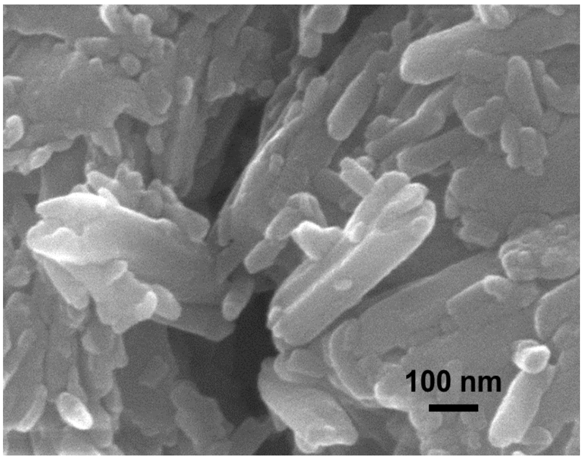

Fig. S4-2. SEM image of (1DHPD:1SDH)/HNTs sample at 70% loading after 70 cycles. No obvious change of the HNTs morphology have been observed

References

[1] Y.M. Lvov, D.G. Shchukin, H. Möhwald, R.R. Price, *ACS Nano* **2008**, *2*, 814.

[2] E. Joussein, S. Petit, J. Churchman, B. Theng, D. Righi, B. Delvaux, *Clay Miner.* **2005**, *40*, 383.

[3] D.G. Shchukin, G.B. Sukhorukov, R.R. Price, Y.M. Lvov, *Small* **2005**, *1*, 510.

[4] E. Abdullayev, R. Price, D. Shchukin, Y. Lvov, *ACS Appl. Mater. Interfaces* **2009**, *1*, 1437.

[5] D. Fix, D. V. Andreeva, Y.M. Lvov, D.G. Shchukin, H. Möhwald, *Adv. Funct. Mater.* **2009**, *19*, 1720.

[6] M. Zhao, P. Liu, *Microporous Mesoporous Mater.* **2008**, *112*, 419.

[7] D. Mei, B. Zhang, R. Liu, Y. Zhang, J. Liu, *Sol. Energy Mater. Sol. Cells* **2011**, *95*, 2772.

[8] W. Liang, Y. Wu, H. Sun, Z. Zhu, P. Chen, B. Yang, A. Li, *RSC Adv.* **2016**, *6*, 19669.

[9] V. Farmer, J. Russell, *Spectrochim. Acta* **1964**, *20*, 1149.

[10] M. Klähn, G. Mathias, C. Kötting, M. Nonella, J. Schlitter, K. Gerwert, P. Tavan, *J. Phys. Chem. A* **2004**, *108*, 6186.

[11] E. Joussein, S. Petit, B. Delvaux, *Appl. Clay Sci.* **2007**, *35*, 17.

[12] S.D. Sharma, H. Kitano, K. Sagara, *Res. Rep. Fac. Eng. Mie Univ.* **2004**, *29*, 31.

[13] M.M. Farid, A.M. Khudhair, S.A.K. Razack, S. Al-Hallaj, *Energy Convers. Manag.* **2004**, *45*, 1597.

[14] S.M. Chathoth et al, *EPL* **2012**, *97*, 66004.

[15] S. Yashonath, P. Santikary, *J. Phys. Chem.* **1994**, *98*, 6368.

[16] A. Striolo, *Nano Lett.* **2006**, *6*, 633

[17] E.G. Derouane, J.B. Nagy, C. Fernandez, E. Laurent, P. Maljean, *Appl. Catal* **1988**, *40*, L1.

[18] W.H. Qi, M.P. Wang, *J. Mater. Sci. Lett.* **2002**, *21*, 1743.

[19] K.K. Nanda, S.N. Sahu, S.N. Behera, *Phys. Rev. A* **2002**, *66*, 013208.

[20] E. Roduner, *Chem. Soc. Rev.* **2006**, 35, 583.

[21] L. Czuchajowski, S. Duraj, M. Kucharska, *J. Mol. Struct.* **2009**, *34*, 187.

[22] L. Geng, S. Wang, T. Wang, R. Luo, *Energy and Fuels* **2016**, *30*, 6153.

[23] S. Cantor, *Thermochim. Acta* **1979**, *33*, 69.

[24] H.W. Ryu, S.W. Woo, B.C. Shin, S.D. Kim, *Sol. Energy Mater. Sol. Cells* **1992**, *27*, 161.

[25] N. Xie, Z. Huang, Z. Luo, X. Gao, Y. Fang, Z. Zhang, *Appl. Sci.* **2017**, *7*, 1317.

5. Bentonite form-stable eutectic hydrated salt phase change material

As investigated in chapter 4, 1 $Na_2HPO_4·12H_2O$:1 $Na_2SO_4·10H_2O$ (1 DHPD:1 SDH) as eutectic hydrated salt mixture (EHS) is an advantageous hydrated salts PCM with no phase separation during melting, showing a certain stability over cycling and exhibits a proper melting temperature. In my further study of mineral porous materials as matrix to form form-stable phase change material (FSPCM) (chapter 5, 6, 7), this hydrated salts mixture is continued to be applied as PCM.

Bentonite is a natural aluminium phyllosilicate mineral[1]. It is also referred as montmorillonite. It is with one octahedral Al_2O_3 sheet in the middle and two tetrahedral SiO_2 sheets outside[1]. It has the merits of low cost and high thermal conductivity[2] due to the nanolayered structure, which are favourable as matrix for FSPCM. Bentonite has been reported to load organic phase change materials (OPCMs) such as paraffin[3], PEG[4], fatty acid[5], dodecanol[6], butyl stearate[7], etc. No chemical bonding was formed between the OPCM and bentonite, as proved by the XRD pattern and FTIR spectrum. The fire resistance of the bentonite form-stable OPCM (OPCM@bentonite) improved with an increasing ratio of bentonite[8].

Despite numerous studies on OPCM@betonite FSPCM, the work on hydrated salts as PCM to form FSPCM with bentonite hasn't been reported. It is noticeable, bentonite has a good water absorbability[9]. When dispersed in water, it swells and remains suspended. There are also some cations (Na^+, Ca^{2+} or Mg^{2+}) dispersing between the silicate nanolayers to compensate their slight negative charges. These cations are loosely held and can be easily replaced by other cations. Based on the water absorbability and cation exchange capacity, bentonite could be a potential matrix for holding hydrated salts to form FSPCM.

In my work, bentonite form-stable eutectic hydrated salt PCM (EHS@bentonite) is fabricated for the first time by vacuum impregnation. The loading efficiency and the structural as well as thermal properties of the FSPCM are investigated in this chapter.

5.1 Experimental part

Bentonite (nanoclay) was purchased from Sigma, UK. It was dried at 120 °C for 12 hours to remove the interlayer water residue[10]. The hydrated salts used and the instruments applied for the fabrication and characterisation were the same as in chapter 4 (Tab. 4-1, 4-2).

To fabricate EHS@bentonite composite, five portions of concentrated hydrated salts soloutions were made by dissolving 7 g EHS in 3 mL deionized H_2O under 40 °C in the first step. 7 g, 4.67 g, 3 g, 1,75 g and 0.78 g of bentonite were added to each of the EHS solution to form EHS/bentonite dispersions with 50%, 60%, 70%, 80% and 90% EHS mass ratio loading. The dispersions were sonicated (output 100 W) at 40 °C for 30 minutes and stood still at R. T. for 10 minutes. The 50% and 60% solutions remained as homogeneous light brown suspensions, while the 70%, 80% and 90% solutions showed obvious phase separation with clear liquid solvent in the upper layer and the light brown sediment in the down layer. Then, all the samples were put under vacuum impregnation at 40 °C for three times as described in 4.1.2. After that, they were again kept still at R.T. for 10 minutes. The 50% and 60% samples remained as homogenous mud-like light brown suspensions, and the samples with higher EHS mass ratio from 70% to 90% still showed phase separation. This demonstrated, bentonite does not have capacity to load 70% or higher mass ratio of EHS. So only the 50% and 60% samples were further cooled at 4 °C for 30 minutes and dried in desiccator at room temperature for 2 days until the weight was constant. For both 50% and 60% EHS@bentonite light brown powder was obtained as end product.

The characterisation techniques and their measuring conditions are the same as described in 4.1.2.

5.2 Results and discussions

5.2.1 Morphology and pore structure of bentonite

As shown in Fig. 5-1, bentonite shows the morphology as nano-/microspheres with size ranging from 800 nm to 30 μm. It is observed, folds are distributed around bentonite particle forming interspace with irregular shapes and different sizes ranging from ten to several hundred nanometre.

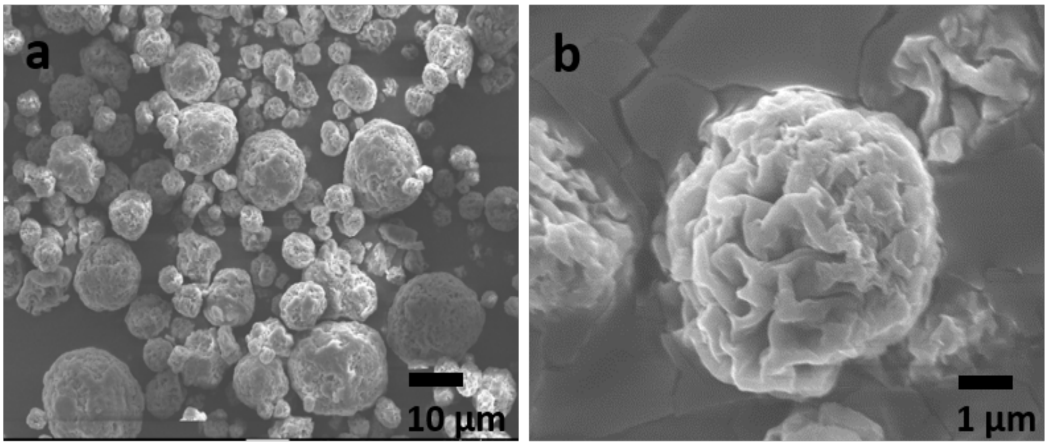

Fig. 5-1 SEM images of bentonite with magnification of (a) *1000 (b)*10000

The N_2 adsorption-desorption isotherms of bentonite are shown in Fig. 5-2. Bentonite has Type IV isotherms, which are associated with mesoporous material. The hysteresis loop is due to the capillary condensation in mesopores. The shape of the hysteresis loop is classified as H4, indicating the presence of particles with irregular internal voids in broad size distribution and narrow slit-like pores, which is in accordance with the SEM images of bentonite. From the BET calculation, bentonite has the pore volume of 0.110 $cm^3 \cdot g^{-1}$ and the surface area of 62.00 $m^2 \cdot g^{-1}$.

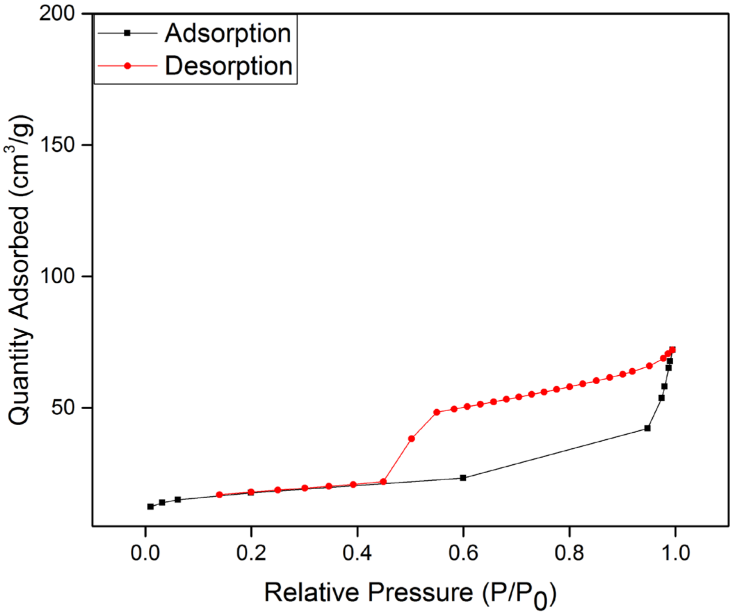

Fig. 5-2 N_2 adsorption-desorption isotherms of bentonite

The pore size distribution of bentonite concluded by BJH method is shown in Fig. 5-3. Pores are distributed most at 24 nm, which could result from the internal voids among the particle folds and the interspace between nanolayers in bentonite.

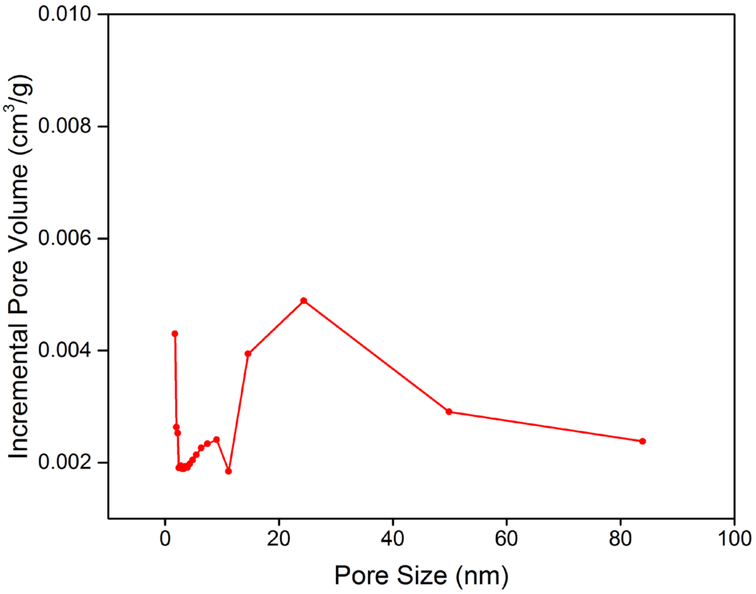

Fig. 5-3 Pore size distribution of bentonite

5.2.2 Properties of bentonite form-stable eutectic hydrated salt

The 50% and 60% EHS@bentonite composites were fabricated by vacuum impregnation as described in 5.1. The FTIR patterns of the composites are compared with the patterns of bentonite and EHS in Fig. 5-4. The relevant peak positions are tabulated in Tab. 5-1. Bentonite shows several characteristic absorption peaks. The peak at 3615 cm^{-1} is due to the stretching vibration of O-H connected to the aluminium ion, which is also present in both composites[11]. The absence of the broad peak at around 3440 cm^{-1} indicates the interlayer water molecules in bentonite have been removed[12]. The peaks at 989 and 448 cm^{-1} are from the antisymmetric vibration and the bending vibration of Si-O-Si[13][14]. EHS shows the broad peak at 3341 cm^{-1} attributed to the O-H stretching of hydrate water. This peak is also present in the composites without much shift, and the broad shape of the peak retains, indicating the hydrate water is well kept in composites. The peaks at 1075 and 981 cm^{-1} from the vibration of P-O in EHS[15] are integrated with the peak at 989 cm^{-1} from Si-O-Si in bentonite, and a relative broad peak at around 980 cm^{-1} is observed in the composites. The peaks at 612 and 446 cm^{-1} in the composites are assigned to the vibration of S-O from the incorporated EHS[16] and the vibration of Si-O-Si from the betonite as matrix. In general, all the characteristic peaks of bentonite and EHS are present in the EHS@bentonite composites. 50% and 60% composites show fast the same FTIR pattern. EHS has been successfully loaded into the EHS@betonite composites. The chemical structures of EHS and betonite are kept well in composites. No new peaks are found, indicating no new covalent bonding is formed between bentonite matrix and EHS in composites.

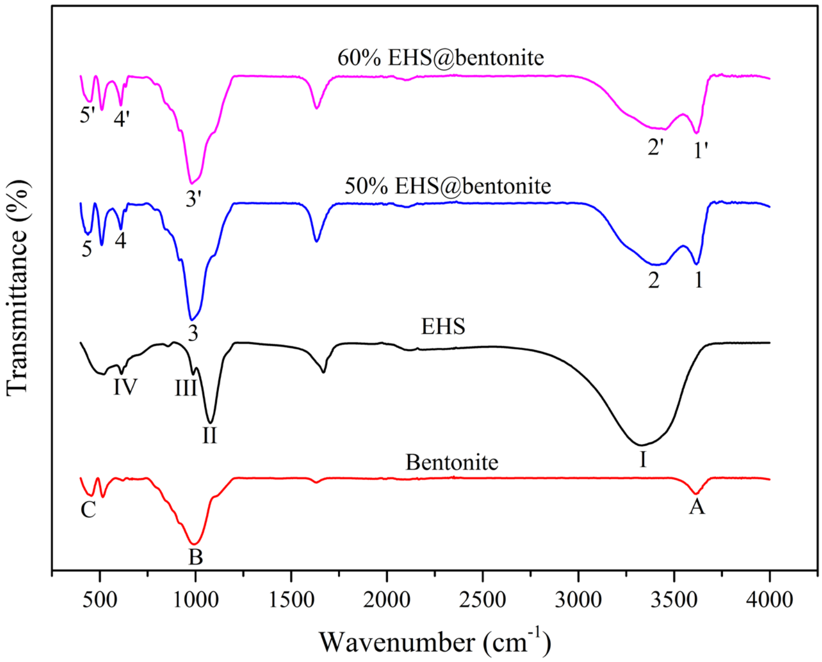

Fig. 5-4 FTIR spectra of bentonite, EHS, 50% and 60% EHS @bentonite

Tab. 5-1 Tabulation of FTIR spectra transmittance of bentonite[11]–[14], EHS[15][16] and EHS@bentonite

Signal	A	B	C		
Peak position (cm^{-1})	3615	989	448		
Assignment	AlO-H	Si-O-Si	Si-O-Si		
Signal	I	II	III	IV	
Peak position (cm^{-1})	3341	1075	981	612	
Assignment	O-H	P-O	P-O	S-O	
Signal	1	2	3	4	5
Peak position (cm^{-1})	3615	3395	980	612	446
Assignment	AlO-H	O-H	Si-O-Si; P-O	S-O	Si-O-Si
Signal	1’	2’	3’	4’	5’
Peak position (cm^{-1})	3615	3400	984	612	446
Assignment	AlO-H	O-H	Si-O-Si; P-O	S-O	Si-O-Si

The XRD patterns of EHS, bentonite and 50% and 60% EHS@bentonite composites are shown in Fig. 5-5. Bentonite shows evident diffraction reflections at 19.8 °, 28.3 °, 35 °, 54.1 ° and 61.8 °, which shows it has a good crystallinity as the nanolayers in the structure are regularly ordered. While the broad reflections at 28.3 ° and 54.1 ° were observed in the same 2Θ carrying some sharp small peaks, the other reflections of bentonite are directly shown in the XRD patterns of the composites without shift. The crystallinity of the matrix bentonite retains well after loading with EHS in both composites. The expanding of the interplanar crystal spacing hasn't taken place, which is unlike the case of loading some long chain organic molecules[3].

Most of the strong diffraction peaks of EHS are present in the 50% EHS@bentonite composite. Some multiplet peaks, such as at 19.7 ° and 20.4 ° from EHS have merged into the broad reflection from bentonite and become indistinguishable in the composites. The peaks at 2Θ at 16.8 ° and from 30 ° to 32 ° show an obviously reduced intensity in the composites comparing to those in EHS. The reduction of the intensity of the EHS peaks is stronger in 50% than in 60% composite. It is suspected, the bentonite has moderately changed the crystallinity of EHS loaded. EHS should be loaded into the nanosized internal voids or intercalated in the nanolayers of bentonite, and the nano-confinement and hydrogen bonding with interlayer water molecules could affect the crystallinity of EHS. Also, the hydrated salts loaded on the surface of bentonite particles could lose hydrate water, so the crystallinity of EHS is degraded in the composite.

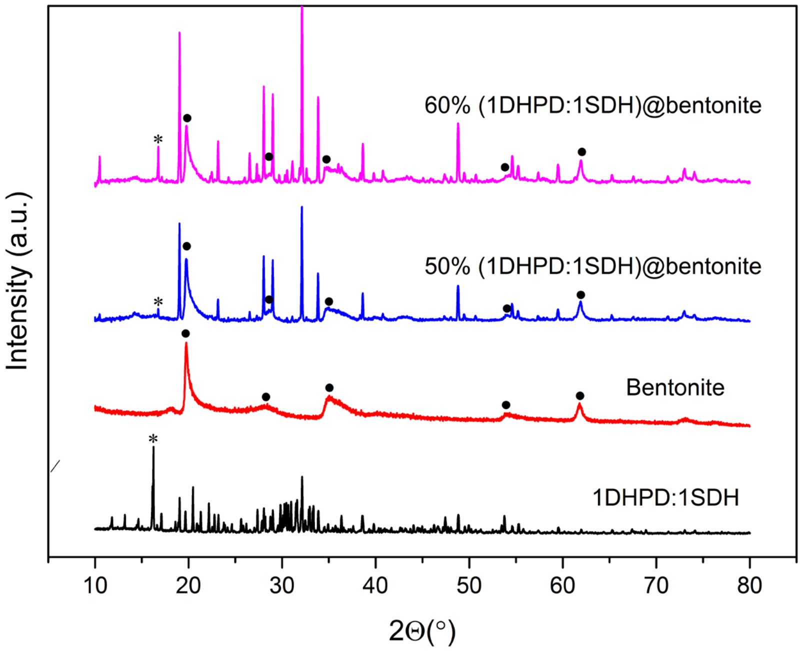

Fig. 5-5 XRD patterns of EHS, bentonite, 50% and 60% EHS@bentonite

The SEM images of the 50% and 60% EHS@bentonite composites comparing to the unloaded betonite are shown in Fig. 5-6. Both composites are covered with PCM as block material on the surface. By 50% composite bigger polyhedral crystals and irregular aggregates are relatively loosely mixed, while by 60% composite smaller size of aggregates are more densely stacked.

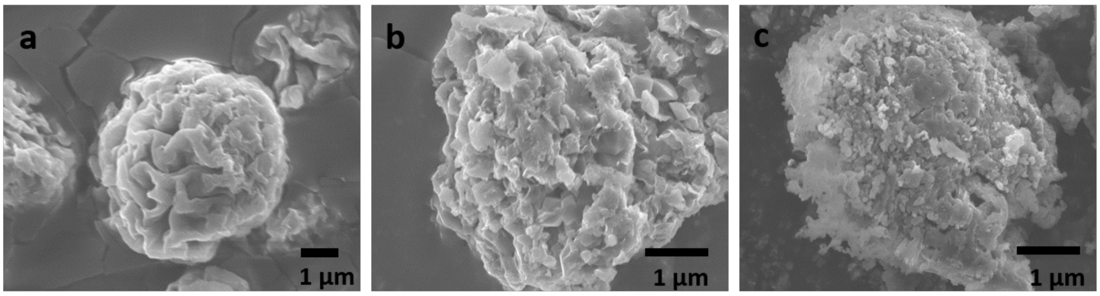

Fig. 5-6 SEM images of (a) pure bentonite (b) 50% and (c) 60% EHS@bentonite

The EDS spectra of bentonite and 50% EHS@bentonite are shown in Fig. 5-7. Bentonite contains the Si, O, Al, Mg, Na elements. The composite shows apart from the elements from the bentonite matrix, also P, S from the EHS as PCM. The amount of Na is largely increased in the composite due to the contribution from EHS.

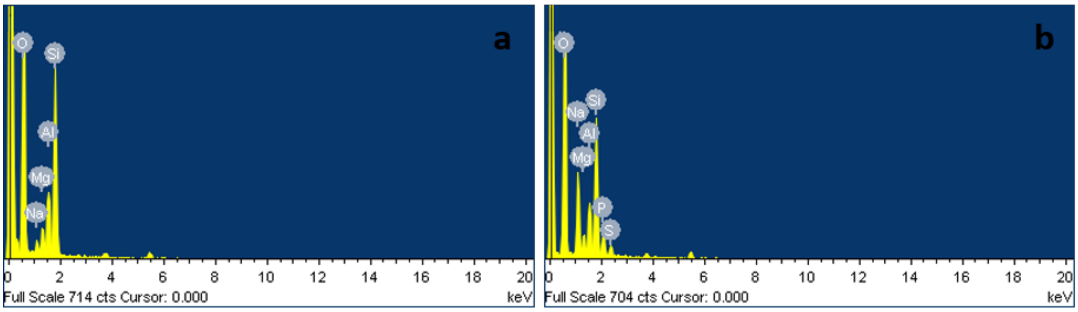

Fig. 5-7 EDS spectra of (a) bentonite (b) 50% EHS@bentonite

The DSC curves of 50% and 60% EHS@bentonite composites are displayed in Fig. 5-8. The 50% composite shows a very low melting enthalpy of 32.5 $J \cdot g^{-1}$, corresponding only 15.3 % loading efficiency of EHS. The melting curve shows a broad peak at 33.7 °C with a small shoulder at 25.7 °C. The pure EHS has one melting peak at 38.5 °C (Fig. 4-10). The main peak at 33.7 °C is attributed to the melting of EHS in the composite. The decreasing of the eutectic melting temperature could be resulted from the nano-confinement of EHS in bentonite, as interplanar space between nanolayers, internal voids among the folds in nanosize and narrow slits are present in this matrix material. The broad shape of the melting peak indicates the confinement effect of betonite on EHS is not uniform, as the shapes of the voids are irregular and some EHS might be absorbed on the surface of the bentonite and not confined at all.

The 60% composite shows a strong phase separation. The main melting peak at 34.7 °C is from EHS, and the smaller peak at 47.2 °C is from $Na_2HPO_4 \cdot 7H_2O$. It also exhibits a similar low melting enthalpy of 35.3 $J \cdot g^{-1}$ as 50% composite. The low loading efficiency of bentonite is in accordance with its relatively limited porosity, with 0.110 $cm^3 \cdot g^{-1}$ pore volume, only about 38.7% of that from halloysite. Large part of EHS by 50% and 60% composites are absorbed on the surface of bentonite. During the loading and drying process, the hydrated salts mixture may get degraded in the air.

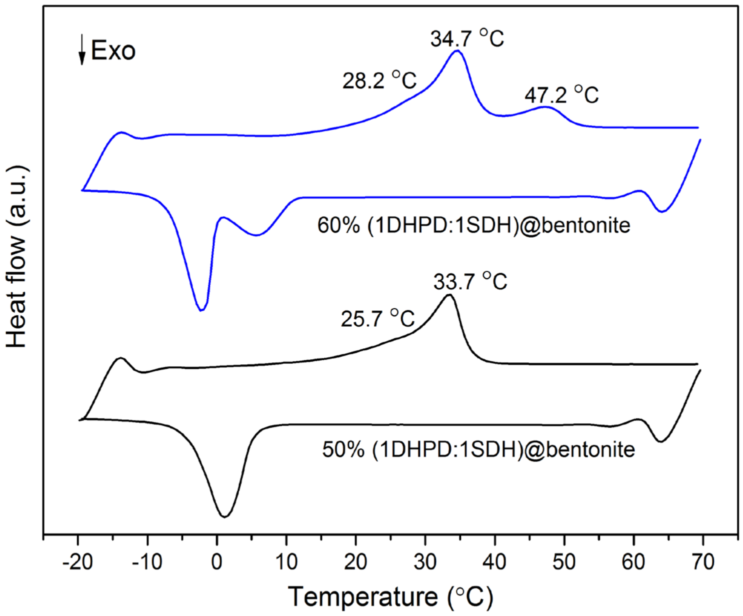

Fig. 5-8 DSC curves of 50% and 60% EHS@bentonite

Due to the low loading efficiency and tend to show phase separation, the stability and cycling tests of EHS@bentonite are not further carried.

5.3 Conclusions

In this work, bentonite as porous matrix material to form EHS loaded composites was studied. It shows the morphology of porous nano-/microparticles. Due to the limited absorption and swelling properties, 50% and 60% EHS@bentonite were able to be fabricated by vacuum impregnation. FTIR shows no new peaks are formed in the composite, though hydrogen bonding makes small shifts of some EHS peaks in the composites. XRD shows the crystallinity of bentonite is remained in the composite, while the EHS might lose some crystallinity in the composites. The SEM images reveal part of the PCM are located on surface of betonite in both composites. Finally, the DSC characterisation shows the loading efficiency of EHS PCM in betonite reaches only about 15%. So big ratio of EHS loaded in 50% and 60% composites are degraded. On one hand the porosity of bentonite is not very high, on the other hand some internal voids of it could be shallow and relative big, so the leakage of the PCM occurs easily and the hydrated salts on surface of bentonite can lose hydrate water in the air and thus lose the thermal energy storage capacity.

References

[1] J. Hrachová, P. Komadel, V.Š. Fajnor, *Mater. Lett.* **2007**, *61*, 3361.

[2] A. Sari, *Energy Convers. Manag.* **2016**, *117*, 132.

[3] M. Li, Z. Wu, H. Kao, J. Tan, *Energy Convers. Manag.* **2011**, *52*, 3275.

[4] A. Sari, C. Alkan, A. Biçer, C. Bilgin, *Int. J. Energy Res.* **2014**, *38*, 1478.

[5] M. Chen, S. Zheng, S. Wu, G. Xu, *J. Wuhan Univ. Technol. Sci. Ed.* **2010**, *25*, 674.

[6] X. Fang, Z. Zhang, *Energy Build.* **2006**, *38*, 377.

[7] X. Fang, Z. Zhang, Z. Chen, *Energy Convers. Manag.* **2008**, *49*, 718.

[8] Y. Cai, Y. Hu, L. Song, H. Lu, Z. Chen, *Thermochim. Acta* **2006**, *451*, 44.

[9] J. Wilson et al, *Bentonite: A Review of key properties, processes and issues for consideration in the UK context*, **2011**.

[10] A. Kutlić, G. Bedeković, I. Sobota, *Rud. Geol. Naft. Zb.* **2013**, *24*, 61.

[11] V.C. Farmer, J.D. Russell, *Spectrochim. Acta* **1964**, *20*, 1149.

[12] G.R. Hunt, J.W. Salisbury, C.J. Lenhoff, *Mod. Geol.* **1973**, *4*, 85.

[13] H.W. van der Marel, R. Van Der Marel, H. van der Marel, H. Beutelspacher, *Atlas of Infrared Spectroscopy of Clay Minerals and Their Admixtures*, Elsevier **1976**.

[14] A. Gupta, V. Amitabh, B. Kumari, B. Mishra, *RJPBCS* **2013**, *4*, 360.

[15] M. Klähn, G. Mathias, C. Kötting, M. Nonella, J. Schlitter, K. Gerwert, P. Tavan, *J. Phys. Chem. A* **2004**, *108*, 6186.

[16] L. Czuchajowski, S. Duraj, M. Kucharska, *J. Mol. Struct.* **2009**, *34*, 187.

6. Diatomite form-stable eutectic hydrated salt phase change material

Diatomite is a natural siliceous mineral originated from fossilised remains of diatoms[1], which consists of 80-90 wt% silica (SiO_2)[2]. It has an abundant reserve, 90% porosity, large specific surface area and properties such as non-toxicity, heat resistance and wear resistance. It is considered as a material with broad application prospects, such as adsorbent[3]–[5] and catalyst matrix[6]. To improve the purity and adsorbability of diatomite, it is usually treated by calcination or acid-washing, etc. before application. It has been applied as matrix for organic phase change material (OPCM) and salts to form form-stable phase change material (FSPCM) with a wide range of melting temperature[7][8]. Qian et al.[8] used PEG, $LiNO_3$ and Na_2SO_4 to fabricate diatomite based FSPCM with melting temperature at 58.0 ˚C, 250.7 ˚C, and 887.6 ˚C. Qin et al.[9] synthesised diatomite form-stable Na_2SO_4 PCM (Na_2SO_4@diatomite) with the loading of PCM increasing from 50% to 85%. Accordingly, the melting enthalpy of the composite was increased.

Hydrated salts as PCM to form FSPCM with diatomite are rarely studied. In this chapter, diatomite is applied as matrix material to form diatomite form-stable eutectic hydrated salt PCM (EHS@diatomite). Before the loading process the raw diatomite was pre-treated by calcination and acid-washing. The change of the morphology and porosity of the material was recorded. The loading was proceeded by vacuum impregnation. Properties of EHS@diatomite such as loading efficiency, composition, crystallinity, morphology and phase transformation were investigated and the effect of diatomite as matrix for EHS was evaluated.

Hydrated salts as PCM to form FSPCM with diatomite are rarely studied. In this chapter, diatomite is applied as matrix material to form EHS@diatomite FSPCM. Before the loading process the raw diatomite was pre-treated by calcination and acid-washing. The change of the morphology and porosity of the material was recorded. The loading was proceeded by vacuum impregnation. Properties of EHS@diatomite such as loading efficiency, composition, crystallinity, morphology and phase transformation were investigated and the effect of diatomite as matrix for EHS was evaluated.

6.1 Experimental part

Diatomite (flux calcined, nanoclay) was purchased from Sigma, UK. The raw diatomite was calcined at 450 ˚C for 3h, and then treated with sulfuric acid (H_2SO_4, 60%) for 4h, then dried at 105 ˚C for 4h. The diatomite after the treatment was applied for the fabrication of EHS@diatomite composites. The hydrated salts used and the instruments applied for the fabrication and characterisation were the same as in chapter 3 (Tab. 3-1, 3-2).

To fabricate EHS@diatomite composites with various loadings, first EHS/diatomite dispersions with various mass ratio of EHS were formed by adding diatomite into EHS water solution with 7 g EHS dissolved in 3 mL deionized water at 40 °C. By adding 7 g, 4.67 g, 3 g, 1.75 g and 0.78 g diatomite, dispersions of 50%, 60%, 70%, 80% and 90% (mass ratio) EHS were formed. The dispersions were sonicated (output 100 W) at 40 °C for 30 minutes and stood still at R. T. for 10 minutes. The 50% and 60% solutions were homogeneous white suspensions, while the 70%, 80% and 90% solutions showed phase separation of liquid upper layer and white thick sediment at the bottom. Next, all the samples were put to vacuum impregnation at 40 °C for three times as described in 3.1.2. Then, they were again kept still at R.T. for 10 minutes. The 50% and 60% samples remained as homogenous thick suspensions, while the 70% to 90% samples still showed phase separation. Diatomite was only capable to load up to 60% EHS, so the 50% and 60% samples were further cooled at 4 °C for 30 minutes and dried in desiccator at room temperature for 2 days until the weight was constant. White powder was obtained as end product for 50% and 60% EHS@diatomite. The conditions for each characterisation are described in 3.1.2.

6.2 Results and discussions

6.2.1 Morphology and pore structure of diatomite

The morphology of diatomite is shown in the SEM images in Fig. 6-1. Diatomite is plate like solid with size ranging from 1μm to 20 μm (Fig. 6-1a). The raw diatomite has the morphology of dense plates with dents on the periphery (Fig. 6-1b). After the calcination and acid treatment, numerous nanopores are formed on the plate surface of diatomite and the plate shape retains (Fig. 6-1c).

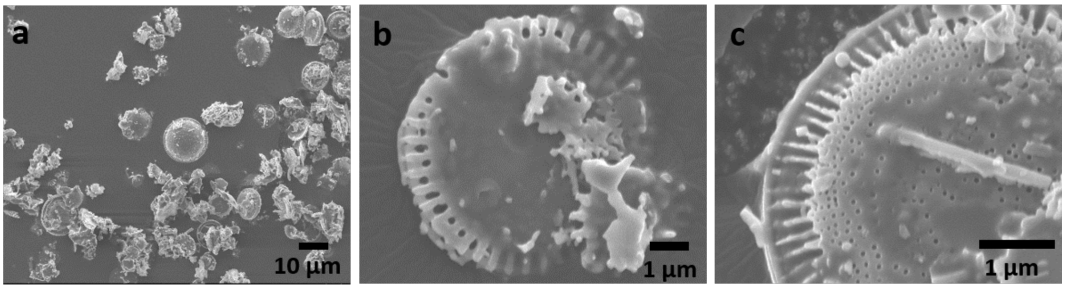

Fig. 6-1 SEM images of (a) raw diatomite with magnification of *800 (b) *8000, (c) processed diatomite with magnification of *20000

The N_2 adsorption-desorption isotherms of processed diatomite are shown in Fig. 6-2. The Type IV isotherms indicates the mesoporous character of diatomite. The H3 hysteresis loop is from the loose assemblages of plate like particles.

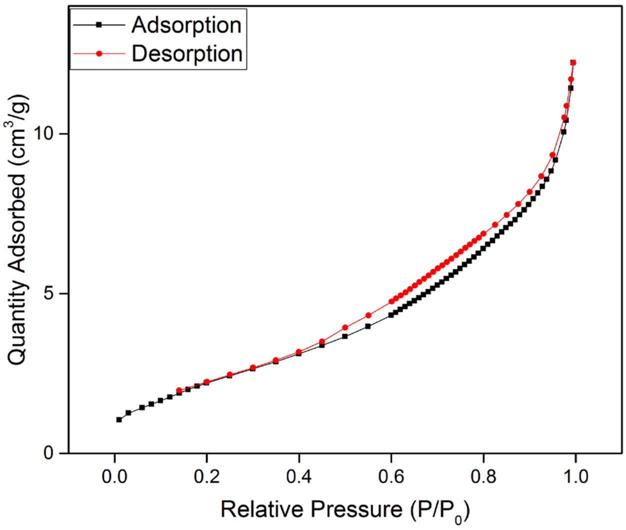

Fig. 6-2 N_2 adsorption-desorption isotherms of diatomite

The pore size distribution of diatomite obtained by BJH is displayed in Fig. 6-3. The pores at 57 nm take up the highest pore volume, which could result from the internal void among stacked diatomite plates.

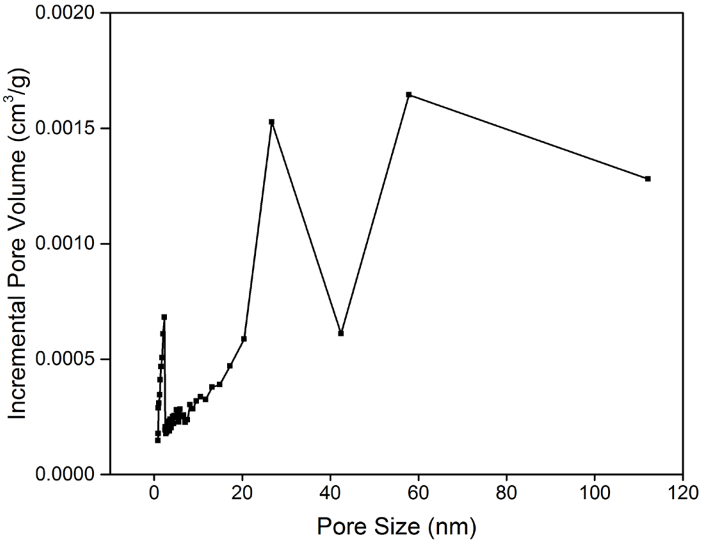

Fig. 6-3 Pore size distribution of diatomite

The pore properties of raw and processed diatomite is calculated by BET method and listed in Tab. 6-1. The raw diatomite shows a very small pore volume. After processing, the pore volume is largely increased from 0.001 to 0.018 $cm^3 \cdot g^{-1}$, but still relatively limited. The surface area has evidently increased from 0.96 to 8.76 $m^2 \cdot g^{-1}$.

Tab. 6-1 Pore properties of diatomite

Diatomite Sample	Pore Volume ($cm^3 \cdot g^{-1}$)	Surface Area ($m^2 \cdot g^{-1}$)
Before processing	0.001	0.96
After processing	0.018	8.76

6.2.2 Properties of diatomite form-stable eutectic hydrated salt

The FTIR spectra of diatomite, EHS, 50% and 60% EHS@diatomite are illustrated in Fig. 6-4. The relevant peak positions are tabulated in Tab. 6-2. Diatomite shows the characteristic peaks at 1070 cm^{-1}, 791 cm^{-1} and 468 cm^{-1} from the Si-O vibration[10] and Si-O-Si symmetric stretching vibration[11] and the O-Si-O bending vibration[11], respectively. The broad peak at 1070 cm^{-1} from diatomite fuses with the peak at 1077 cm^{-1} from the P-O asymmetric stretching vibration in EHS, resulting the peak at 1064 cm^{-1} in both composites. The peaks at 791 cm^{-1} and 468 cm^{-1} from diatomite are found in composites without shift. This proves the chemical structure of diatomite remains well in the EHS@diatomite composites.

The EHS shows the strong broad peak at 3341 cm^{-1} from the O-H stretching vibration and the peak at 1668 cm^{-1} from the H-O-H bending vibration of hydrate water[12]. In the 50% composite, these two peaks are much weaker and show some shift to 3287 cm^{-1} and 1621 cm^{-1}. The 60% composite shows a similar FTIR pattern as the 50% composite, with slightly stronger intensities regarding the peaks from hydrate water. This suggests, the effective loading of hydrated salts are low in diatomite composites, though the 60% composite may have a bit higher loading than the 50% composite. The shifts of the O-H vibration peaks should be from the hydrogen bonding between Si-OH and crystal water. The new peak at 3458 cm^{-1} in the composites is due to the O-H stretching vibration from Si-O-H. The peaks at 985 cm^{-1} and 861 cm^{-1} due to the stretching vibrations of P-O and P-OH[13] are present in the composites with nearly no shift. There should be no evident interaction between the salt anion HPO_4^{2-} and the diatomite matrix.

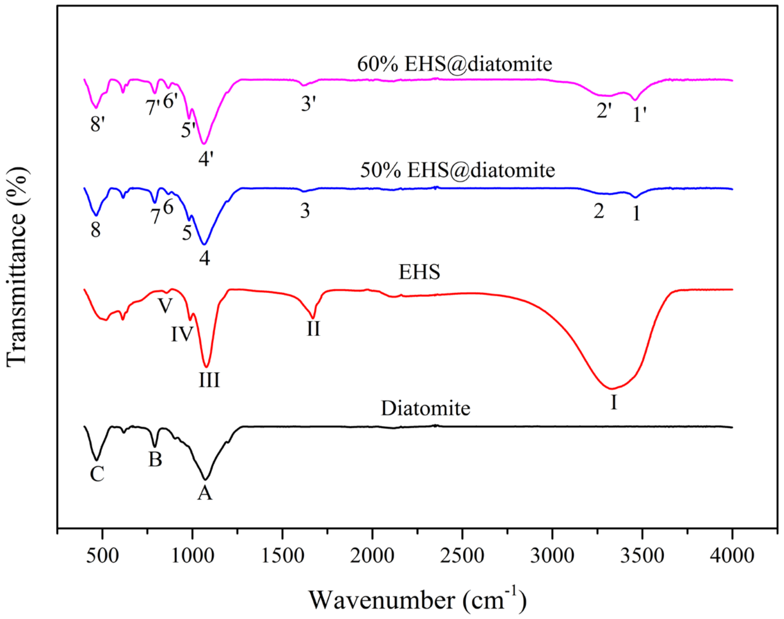

Fig. 6-4 FTIR spectra of diatomite, EHS, 50% and 60% EHS@diatomite

Tab. 6-2 Tabulation of FTIR spectra transmittance of diatomite[10][11], EHS[12][13] and EHS@diatomite

Signal	A	B	C					
Peak position (cm^{-1})	1070	791	468					
Assignment	Si-O	Si-O-Si	O-Si-O					
Signal	I	II	III	IV	V			
Peak position (cm^{-1})	3341	1668	1077	985	861			
Assignment	O-H	H-O-H	P-O	P-O	P-OH			
Signal	1	2	3	4	5	6	7	8
Peak position (cm^{-1})	3458	3287	1621	1064	981	863	791	468
Assignment	Si-O-H	O-H	H-O-H	Si-O;P-O	P-O	P-OH	Si-O-Si	O-Si-O
Signal	1’	2’	3’	4’	5’	6’	7’	8’
Peak position (cm^{-1})	3458	3282	1614	1064	981	863	791	468
Assignment	Si-O-H	O-H	H-O-H	Si-O;P-O	P-O	P-OH	Si-O-Si	O-Si-O

The XRD patterns of 50% and 60% EHS@diatomite comparing with diatomite and EHS are shown in Fig. 6-5. Diatomite has a strong diffraction peak at 21.8 ° from the quartz crystalline phase[14], which is also observed in the composites. Not all diffraction peaks from EHS are present in the composites. This suggests, the crystallinity of EHS has reduced after loading to diatomite. The 60% composite shows a similar diffraction pattern as the 50% composite, with the intensity of some peaks slightly higher.

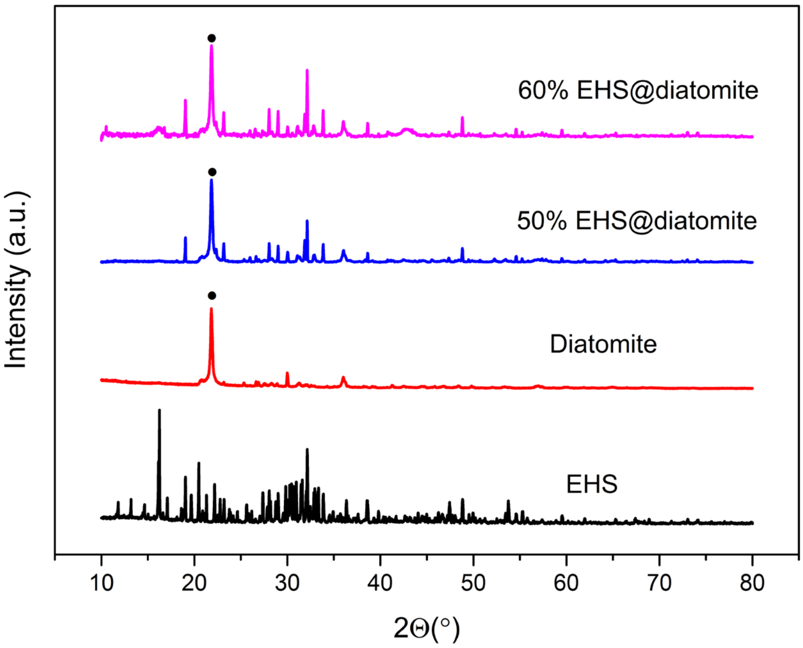

Fig. 6-5 XRD patterns of EHS, diatomite, 50% and 60% EHS@diatomite

The SEM images of 50% and 60% EHS@diatomite comparing to the unloaded diatomite are displayed in Fig. 6-6. In both composites, big blocks of aggregates are observed on the surface of diatomite plate. The sediments by the 60% composite are in a bigger amount than by 50%.

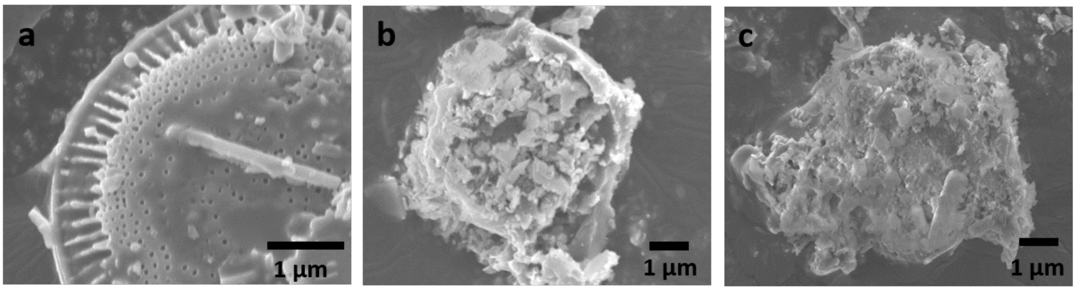

Fig. 6-6 SEM images of (a) processed diatomite (b) 50% and (c) 60% EHS @diatomite

The EDS characterisation in Fig. 6-7 shows that, diatomite consists of the elements Si and O. By loading with EHS, P, S, Na elements were found and the amount of O is largely increased. The amount of P detected is much higher than S, which indicates the distribution of phosphate salt and sulphate salt is not uniform as it originally mixed in the EHS. In the measured area, the phosphate is in much bigger proportion than the sulphate. A separation of the hydrated salts mixture into aggregated phosphate and sulphate could occur in the composite.

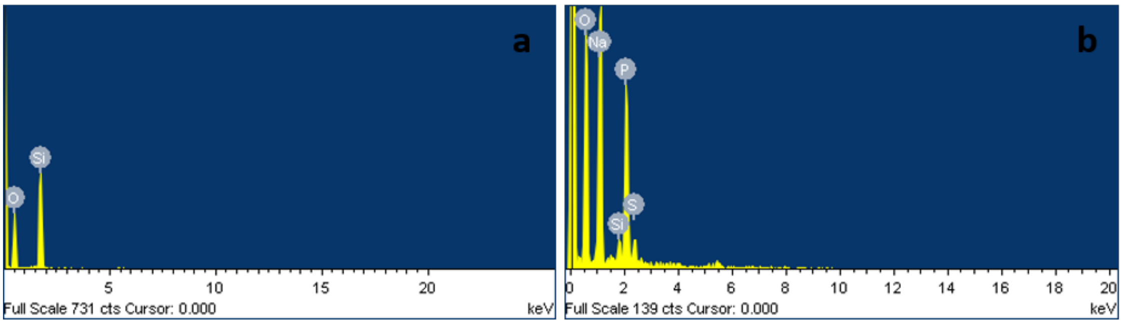

Fig. 6-7 EDS of (a) diatomite (b) 50% EHS@diatomite

The phase change properties of the 50% and 60% EHS@diatomite composites are demonstrated by DSC curves in Fig. 6-8. Both composites show serious phase separation. The 50% EHS@diatomite has the melting peak at 34.7 °C and 52.7 °C. The peak at 34.7 °C is from the mixture of hydrated sulphate salt and hydrated phosphate salt, and the peak at 52.7 °C is attributed to the phase separation of DHPD. The melting enthalpy at 34.7 °C is 17.3 $J \cdot g^{-1}$, which is equal to the efficiency of only 8.2% EHS loading. The 60% composite also shows a similar pattern of phase separation with two big melting peaks at 36.1 °C and 50 °C. The phase separation of DHPD is also obvious. The melting enthalpy at 36.1 °C is 31.2 $J \cdot g^{-1}$, corresponding to 14.7% EHS loading. In general, the EHS@diatomite composites do not exhibit good phase change properties. The phase separation and low loading efficiency makes it unsuitable as FSPCM for practical applications.

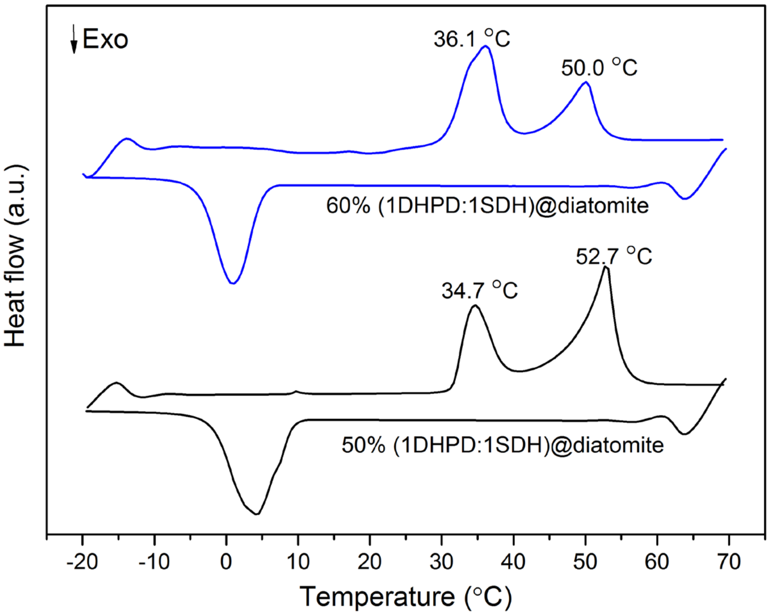

Fig. 6-8 DSC curves of 50% and 60% EHS@diatomite

6.3 Conclusions

In this chapter, diatomite as matrix to form EHS@diatomite FSPCM is investigated. After calcinating and acid processing, it becomes nanoporous plate-like material. Its porosity is evidently smaller than halloysite and bentonite. So its loading capacity of PCM is rather restricted. 50% and 60% EHS@diatomite can be fabricated. The hydrated PCMs are mostly located on plate surface instead being impregnated into the nanopores of diatomite in both composites, as observed from SEM images. Also, as diatomite matrix is composed of SiO_2, which is slightly negatively charged in the presence of water, an electron repulsive interaction with negatively charged P-O from hydrated hydrogen phosphate salt should be considered. It is suspected, DHPD tends to separate from SDH after loading to diatomite and sediment outside the nanopores. The separated hydrated salts exposed as block aggregates could be easily degraded under dried atmosphere. This explains the small hydrate water content in the composites as shown in FTIR spectra, poor crystallinity compared to EHS in XRD patterns and the low efficiency and phase separation of their DSC curves.

References

[1] L. E. Antonides, *Diatomite in United States Geological Survey* **1997.**

[2] S. Mendioroz, M.J. Belzunce, J.A. Pajares, *J. Therm. Anal.* **1989**, *35*, 2097.

[3] M.A.M. Khraisheh, Y.S. Al-degs, W.A.M. Mcminn, *Chem. Eng. J.* **2004**, *99*, 177.

[4] M. Al-Ghouti, M.A.M. Khraisheh, M.N.M. Ahmad, S. Allen, *J. Colloid Interface Sci.* **2005**, *287*, 6.

[5] M.A. Al-Ghouti, M.A.M. Khraisheh, M.N.M. Ahmad, S. Allen, *J. Hazard. Mater.* **2009**, *165*, 589.

[6] E. Modiba, C. Enweremadu, H. Rutto, *Chinese J. Chem. Eng.* **2015**, *23*, 281.

[7] X. Li, J.G. Sanjayan, J.L. Wilson, *Energy Build.* **2014**, *76*, 284.

[8] T. Qian, J. Li, X. Min, Y. Deng, W. Guan, L. Ning, *Energy Convers. Manag.* **2015**, *98*, 34.

[9] Y. Qin, G. Leng, X. Yu, H. Cao, G. Qiao, Y. Dai, Y. Zhang, Y. Ding, *Powder Technol.* **2015**, *282*, 37.

[10] P. Pookmanee, A. Wannawek, S. Satienperakul, R. Putharod, N. Laorodphan, S. Sangsrichan, S. Phanichphant, *Mater. Sci. Forum* **2016**, *872*, 211.

[11] S. Music, N. Filipović-Vinceković, L. Sekovanić, *Brazilian J. Chem. Eng.* **2011**, *28*, 89.

[12] M. Falk, T.A. Ford, *Can. J. Chem.* **1966**, *44*, 1699.

[13] M. Klähn, G. Mathias, C. Kötting, M. Nonella, J. Schlitter, K. Gerwert, P. Tavan, *J. Phys. Chem. A* **2004**, *108*, 6186.

[14] T. Qian, J. Li, Y. Deng, *Sci. Rep.* **2016**, *6*, 1.

7. Sepiolite form-stable eutectic hydrated salt phase change material

Sepiolite is a natural magnesium silicate mineral[1]. It has long fibrous morphology. Its unit cell is a sandwich like a block consisting of one octahedral MgO sheet in the middle and two tetrahedral SiO_2 sheets on the side[2]. These blocks stagger with each other and form parallel channels in the internal structure of the filamentary sepiolite[2]. Due to the loose interleaving of the long fibres and the internal channel structure, sepiolite has a high specific surface area[3]. It is of low cost and in abundant reserve. Other important merits of it include high thermal stability, good mechanical property, chemical resistance and flame retardance[4].As a result, it is a widely applied raw materials in the industry[5][6]. Common applications are for example heterogeneous catalyst[7][8] and adsorbent[9][10]. In the application of form-stable PCM (FSPCM), it has been reported to load various organic phase change material (OPCM), such as paraffin[11][12], dodecanol[11] and lauric acid[13]. The OPCMs were compounded to sepiolite as liquid phase either from the melting[12] or from the concentrated solution in alcohol[11][13].

The study to load hydrated salts as PCM is however rarely reported. Considering its numerous internal channels in nanosize and hydrophilic surface, it shows potential to form hydrated salts FSPCM. In this chapter, sepiolite form-stable eutectic hydrated salt PCM (EHS@sepiolite) with various loading ratios are fabricated by vacuum impregnation. The morphology, chemical bonding and crystallinity of the composites are investigated comparing to the pure PCM and matrix material. The phase change properties and the cycling stability were also characterised. The suitability of sepiolite to fabricate FSPCM with EHS was evaluated.

7.1 Experimental part

Sepiolite (nanoclay) was purchased form Sigma, UK. It was dried at 120 °C for 12 hours before utilisation. The hydrated salts used and the instruments applied for the fabrication and characterisation were the same as in chapter 4 (Tab. 4-1, 4-2).

To fabricate EHS@sepiolite composites, first six portions of concentrated EHS water solutions were formed by dissolving 7 g EHS in 3 mL water at 40 °C. 7 g, 4.67 g, 3g, 1.75 g, 0.78 g and 0.37 g sepiolite were added to each solution to form EHS/sepiolite dispersions with mass ratio of 50%, 60%, 70%, 80%, 90% and 95%. The dispersions were sonicated (output 100 W) at 40 °C for 30 minutes and stood still at R. T. for 10 minutes. The 95% dispersion showed phase separation, while other dispersions were as homogeneous light grey suspensions. Then, all the samples were put to vacuum impregnation at 40 °C for three times as described in 4.1.2, after which, they were kept still at R.T. for 10 minutes. The 95% sample still had phase separation. It was not further processed. Samples of other concentrations remained as homogeneous mixtures and no phase separation was observed. The density and viscosity of the mixtures decreased as the mass ratio of EHS increased. Samples with 50% to 90% EHS loading were further cooled at 4 °C for 30 minutes and dried in desiccator at room temperature for 2 days until the weight was constant. Light grey powder was obtained as end product for all samples.

The characterisation techniques and their measuring conditions are the same as described in 4.1.2.

7.2 Results and discussions

7.2.1 Morphology and pore structure of sepiolite

The SEM images of sepiolite are shown in Fig. 7-1. It has long tubular morphology with the length from 1 to 5μm and the average diameter of 30 nm. They are randomly placed, with the trends to aggregate and tangle with each other. The aggregation could result from the hydrogen bonding between $Si(OH)_2$ groups on the external surface of fibres and a small amount of adhered water in the structure[14]–[16].

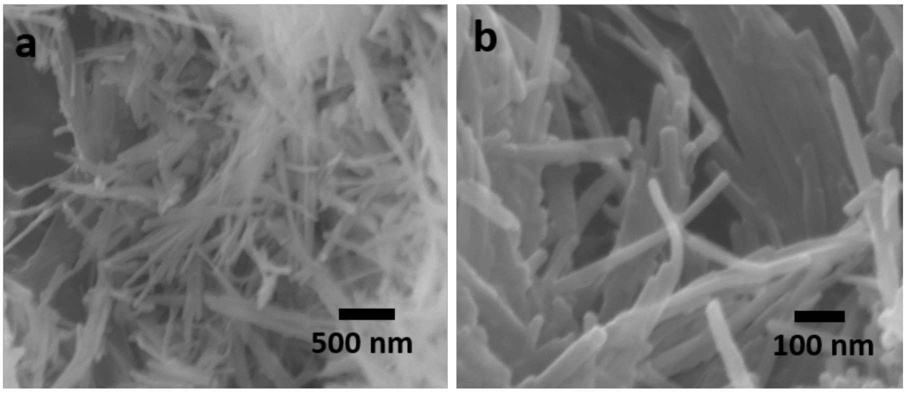

Fig. 7-1 SEM images of sepiolite with magnification of (a)*20000 (b)*40000

The N_2 adsorption-desorption isotherms of sepiolite are shown in Fig. 7-2. The isotherms are of Type IV, which means sepiolite has mesoporous structure. The hysteresis loop is H1, indicating cylindrical pore geometry with fairly uniform pore size.

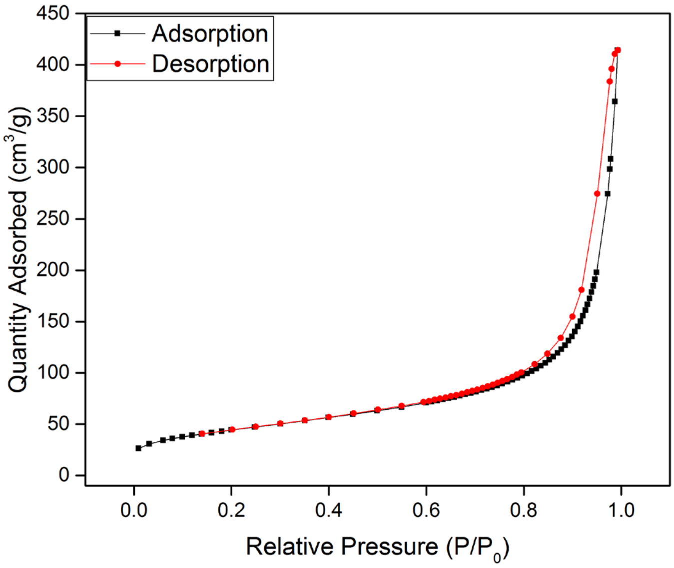

Fig. 7-2 N_2 adsorption-desorption isotherms of sepiolite

The pore size distribution from BJH is shown in Fig. 7-3. The pore size at 24 nm gives the highest pore volume, which should be attributed to the inner voids of the intermeshed long fibres.

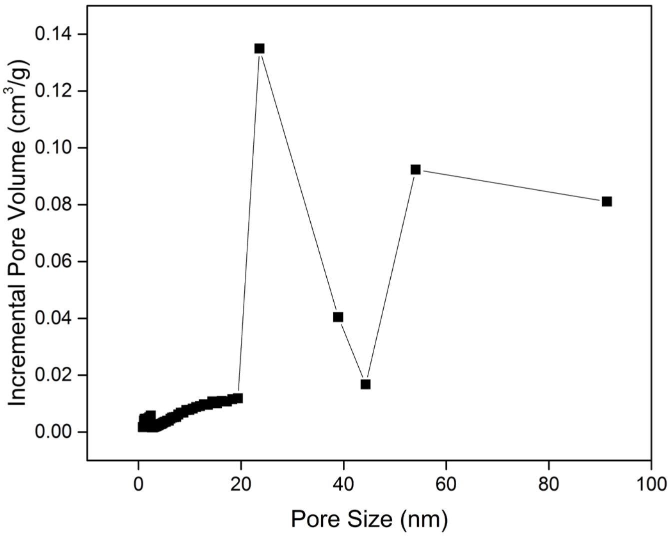

Fig. 7-3 Pore size distribution of sepiolite

According to the BET calculation, sepiolite has a very high pore volume of 0.640 $cm^3 \cdot g^{-1}$ and a big surface area of 156.82 $m^2 \cdot g^{-1}$. Corresponding to the good porosity, sepiolite should show a high loading capacity of PCM.

7.2.2 Properties of sepiolite form-stable eutectic hydrated salt

7.2.2.1 Loadings

The DSC melting curves of EHS@sepiolite with EHS loadings ranging from 50% to 90% are displayed in Fig. 7-4. The corresponding melting T, melting enthalpy and calculated effective loading are listed in Tab. 7-1. All EHS@sepiolite composites show no phase separation during the melting. The melting peaks of the composites are uniform, all near 36 °C, which come from the eutectic melting point of EHS. It shifts to a bit higher temperature as the loading of EHS in the composite increases. 50% EHS@sepiolite exhibits the melting point at 35.5 °C, while the 90% composite is at 38.1 °C, which is quite similar to the melting point of pure EHS at 38.5 °C.

Also, the shape of the melting curves turns broader as the loading increases. This suggests, with higher loadings, some EHS are not confined in the nano channels of sepiolite. The melting enthalpy of the composite grows with the mass ratio of EHS in a consistent rate at about 2 $J \cdot g^{-1} \cdot \%^{-1}$. The loading efficiency of each composite is approximately the original loading ratio of EHS with less than 5% loss. This demonstrates, sepiolite has a high loading capacity of EHS.

Different from EHS@halloysite, by which EHS could lose phase change property when seated outside halloysite nanotubes, all EHS maintain their melting enthalpy well in EHS@sepiolite composites.

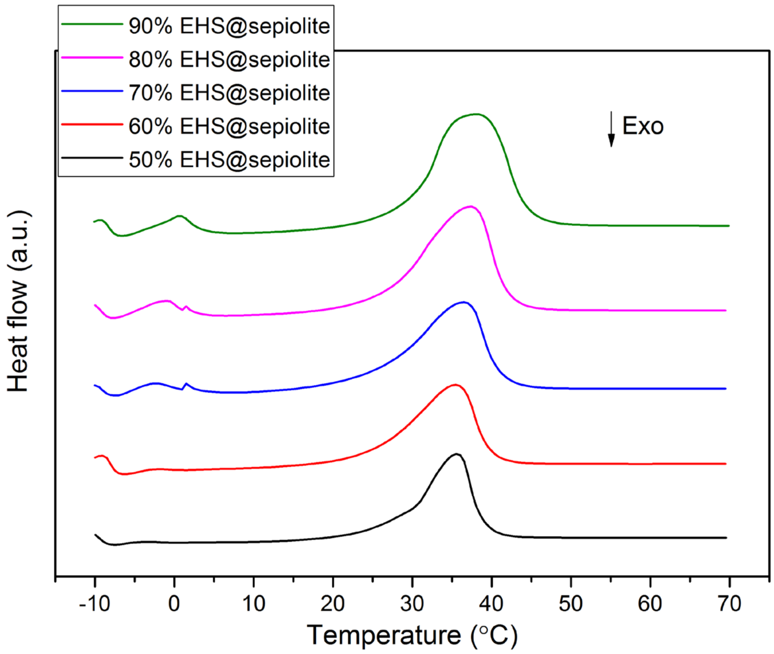

Fig. 7-4 DSC melting curves of EHS@sepiolite with EHS loadings from 50% to 90%

Tab. 7-1 DSC data for melting curves of EHS@sepiolite with various loadings of EHS

EHS mass ratio in EHS@sepiolite	Melting T (°C)	Melting Enthalpy ($J \cdot g^{-1}$)	Effective loading (wt%)
50%	35.5	102	48%
60%	35.7	120	57%
70%	36.4	140	66%
80%	37.3	158	75%
90%	38.1	185	88%

The SEM images of sepiolite and EHS@sepiolite with various loadings are displayed in Fig. 7-5. While the unloaded sepiolite fibres are relatively loosely distributed, the composites show compactness on the surface morphology. By the 50% EHS@sepiolite, the fibres are arranged tight with einander. The individual fibre is still distinguishable, with small voids between fibres or bundles of fibres present. No block material is observed outside the fibres. EHS should be absorbed mainly in the nanochannels of sepiolite fibres. The 60% composite displays a more compact congregation. The fibres are adhered to each other due to the hydrogen bonding between absorbed water and numerous –OH groups on fibre surface[14][15]. The voids are observed only at the ports of fibre bundles. No obvious leakage of block material is observed on the surface of fibre bundles. Apart from the quantity absorbed in nanochannels of sepiolite, some EHS could exist among sepiolite fibres and function as adhesive. The 70%, 80% and 90% EHS@sepiolite show a similar morphology. Fibres are tightly assembled to form sheet like material. The voids are hardly observed between fibres. No block material is present outside fibre sheets. It is suggested, sepiolite fibres have formed porous network to contain big quantities of EHS inside. The EHS should be stable in the network, as no obvious leakage is observed.

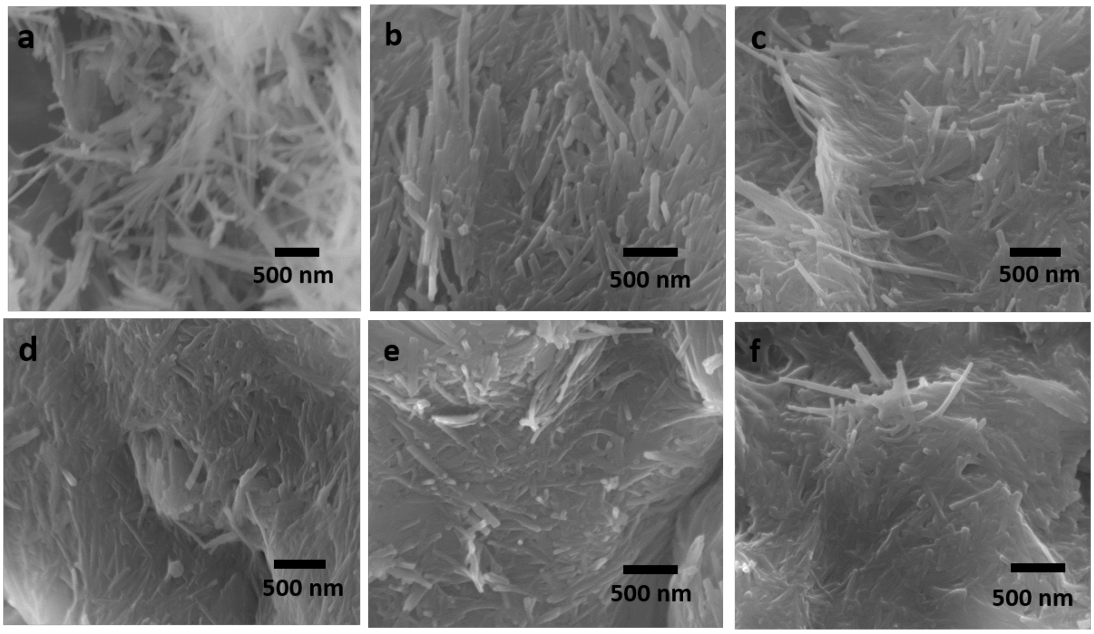

Fig. 7-5 SEM images of (a)sepiolite (b)50% (c)60% (d)70% (e)80% (f)90% EHS@sepiolite

The change of melting enthalpies of EHS@sepiolite with 50%, 60%, 70%, 80% and 90% loadings regarding numbers of thermal cycling is illustrated in Fig. 7-6. The relative DSC data are listed in Tab. S7-1 to S7-5. EHS@sepiolite composites show good cycling stability by all loadings. The decrements of the melting enthalpy after 50 cycles are 2.3%, 6.6%, 0.5%, 2.4% and 3.6% for the 50%, 60%, 70%, 80% and 90% composite respectively. As the loading of EHS increases, no evident reduction on melting enthalpy against growing cycling numbers is observed. The melting enthalpy of the 90% EHS@sepiolite reduces only 7 J·g^{-1} after 50 cycles. The 90% composite sample is used for further characterisations in this chapter.

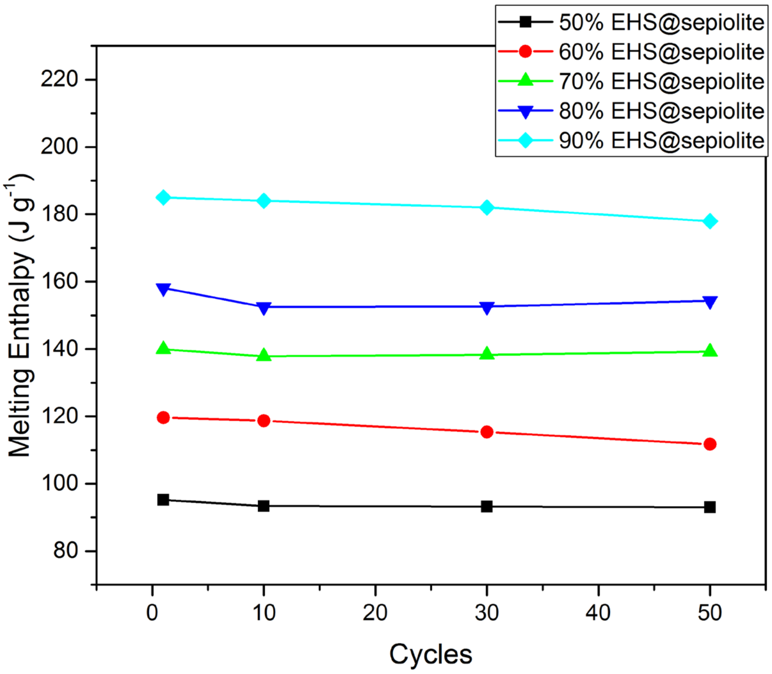

Fig. 7-6 Melting enthalpies of EHS@sepiolite with various loadings vs. numbers of heat uptake cycles

7.2.2.2 Properties

The TEM images of sepiolite and 90% EHS@sepiolite composite are shown in Fig. 7-7. Sepiolite has the morphology of nanofibre with homogeneous texture. The fibres are thin with the average diameter of 30 nm, and the length of 1 to 5 µm, which is consistent with the observation from SEM images (Fig. 7-1). The fibres are easily sticked to each other. Although not directly observed from the TEM image (Fig. 7-7a2), sepiolite fibres should exhibits parallel channels with dimensions of 3.7 Å * 10.6 Å along the axis[5]. These nanochannels are formed by continuous SiO_2 tetrahedrons and discontinuous MgO octahedrons[17]. The composite shows different from pure sepiolite a heterogeneous structure. PCM as dark irregular blocks of several hundred nanometre size are intercalated in the light matrix material (Fig. 7-7b1). The matrix is made of congregation of sepiolite nanofibres (Fig. 7-7b2). On each single fibre, scattering of

PCM as dark dots is also detected (Fig. 7-7b3), indicating the filling of nano channels in sepiolite with EHS.

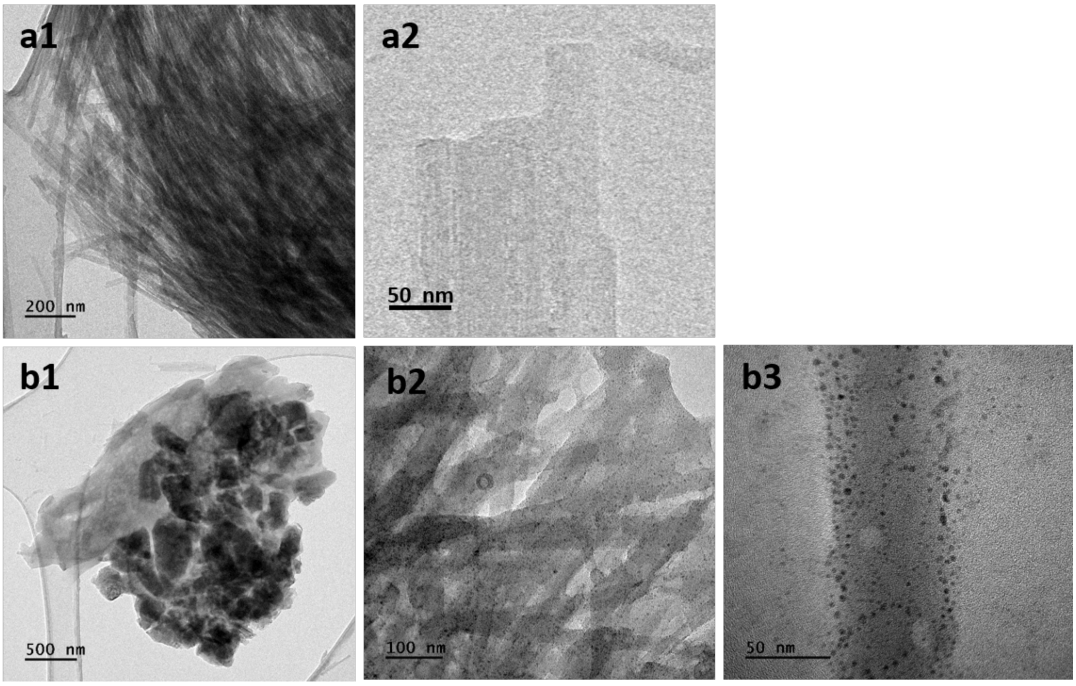

Fig. 7-7 TEM images of (a) sepiolite (b) 90% EHS@sepiolite

The EDS spectra of sepiolite and its composite in Fig. 7-8 demonstrates, EHS has been successfully loaded in the composite. Strong peaks of O, Mg, Si are shown in the EDS of sepiolite (Fig. 7-8a), due to the MgO and SiO_2 nanosheets in the basic unit cell. The small peak of Na is from a trace of Na^+ in channels of sepiolite. In the composite, new peaks of P, S and increased intensity of Na, O peaks are observed, corresponding to the addition of EHS.

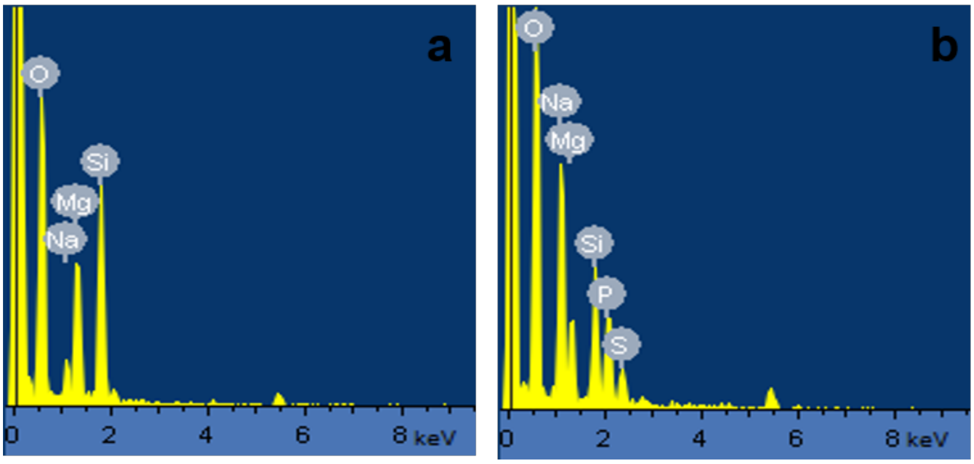

Fig. 7-8 EDS of (a) sepiolite (b) 90% EHS@sepiolite

The FTIR spectrum of 90% EHS@sepiolite comparing to the spectra of EHS and sepiolite is shown in Fig. 7-9. The relevant peak assignments are listed in Tab. 7-2. Sepiolite exhibits the characteristic peak at 3684 cm^{-1} from the stretching vibration of Mg-OH, the peak at 1011 cm^{-1} from the stretching vibrations of Si-O and the peak at 971 cm^{-1} from O-H deformation vibration[18].The peaks at 464 cm^{-1} and 427 cm^{-1} are from the O-Si-O bending vibrations[18]. EHS has the peaks at 1077 cm^{-1} and 985 cm^{-1} due to the vibrations of P-O bonding[19]. In the composite, these two peaks from EHS merge together with the peaks from sepiolite around 1000 cm^{-1} and generate a broad peak at 1075 cm^{-1} with a strong shoulder at 988 cm^{-1}. The peak at 861 cm^{-1} from the P-OH stretching vibration [19] in EHS is present in composite without shift. A relative broad peak at 468 cm^{-1} in the composite is considered as the fusion of O-Si-O vibration peaks and the peak at 521 cm^{-1} from O-P-O bending vibration[19] in EHS. The small peak at 3684 cm^{-1} from the stretching of Mg-OH[18] in sepiolite is present in the composite without shift. The chemical structure of sepiolite should be retained well in the composite. The strong broad peak at 3341 cm^{-1} from the O-H stretching of hydrate water and the sharp peak at 1668 cm^{-1} from the H-O-H bending vibration of hydrate water[20] are observed without shift in both EHS and composite. Hydrate water is kept well in the EHS@sepiolite composite. No new peaks except from sepiolite and EHS are found in the composite, indicating no covalent bonding is formed between EHS and sepiolite.

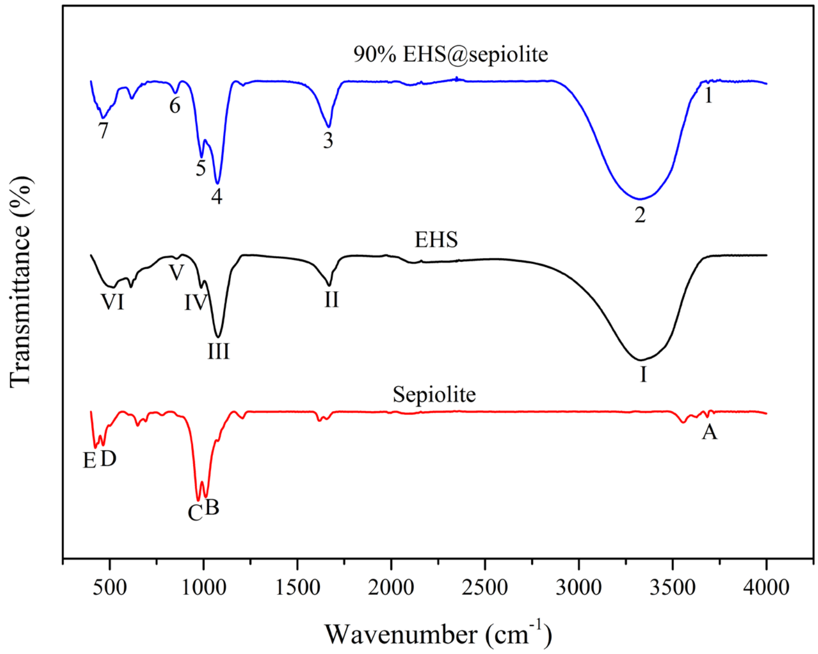

Fig. 7-9 FTIR spectra of EHS, sepiolite and 90% EHS@sepiolite

Tab. 7-2 Tabulation of FTIR spectra transmittance of sepiolite[18], EHS[19][20] and EHS@sepiolite

Signal	A	B	C	D	E	
Peak position (cm^{-1})	3684	1011	971	464	427	
Assignment	Mg-OH	Si-O	O-H	O-Si-O	O-Si-O	
Signal	I	II	III	IV	V	VI
Peak position (cm^{-1})	3341	1668	1077	985	861	521
Assignment	O-H	O-H	P-O	P-O	P-OH	O-P-O

Signal	1	2	3	4	5	6	7
Peak position (cm^{-1})	3684	3341	1668	1075	988	861	468
Assignment	Mg-OH	O-H	O-H	P-O;Si-O; O-H	P-O;Si-O; O-H	P-OH	O-P-O; O-Si-O

The crystal structure of 90% EHS@sepiolite is characterised by XRD pattern as shown in Fig. 7-10. Sepiolite exhibits broader diffraction peaks than EHS. The obvious diffraction reflections from sepiolite including 19.6°, 20.6°, 23.8 °, 35.1°, 36.8 °, 39.8 ° and 73.0° are also observed in the XRD pattern of the composite, indicating the crystal structure of the sepiolite is kept well in EHS@sepiolite. On the other hand, the typical diffraction peaks from EHS such as 19.0°, 23.2°, 29°, 38.7° and 48.8° are completely preserved in the composite. This demonstrates, the crystal structure of EHS is well retained in the 90% EHS@sepiolite.

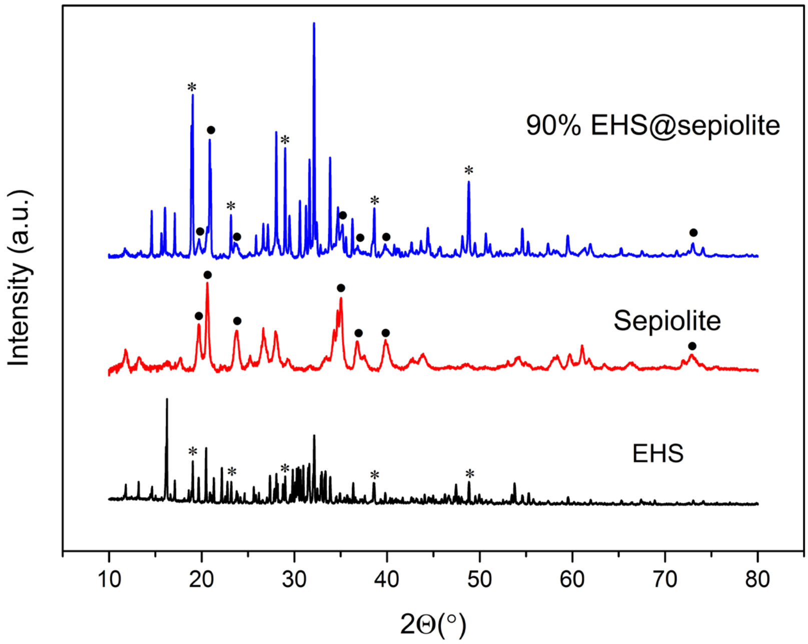

Fig. 7-10 XRD patterns of EHS, sepiolite and 90% EHS@sepiolite

The DSC curves of the 90% EHS@sepiolite composite for 50 thermal cycles are demonstrated in Fig. 7-11. The composite has the melting point of 38.1 °C and the melting enthalpy of 185 $J\cdot g^{-1}$, corresponding to 88% loading efficiency of EHS. The phase change behaviours are stable during 50 heat uptake/release cycles. No phase separation is observed in the melting curves and the freezing behaviour is consistent. After 50 cycles, the shift of the melting temperature is 1.6 °C and the melting enthalpy decreases only 4% with 7 $J\cdot g^{-1}$. Comparing to the phase change behaviours of pure EHS for 50 cycles (chapter 4), the EHS@sepiolite shows obviously better thermal cycling resistance. This could result from the special composition and structure of sepiolite. One part of hydrated salts is absorbed in numerous nanochannels of sepiolite fibres.

The capillary effect and the hydrogen bonding hold the hydrated salts stable in nanochannels on melting. With presence of bigger amount of water, sepiolite fibres tend to intermesh densely with each other to form a network. EHS is kept in the small voids inside the network. The hydrogen bonding as well as the electronic interaction between Mg-OH from sepiolite and P-O from EHS prevent leakage of EHS outside the network. Further, the absorbed water in nanochannels of sepiolite could replenish loss of hydrate water during cycling.

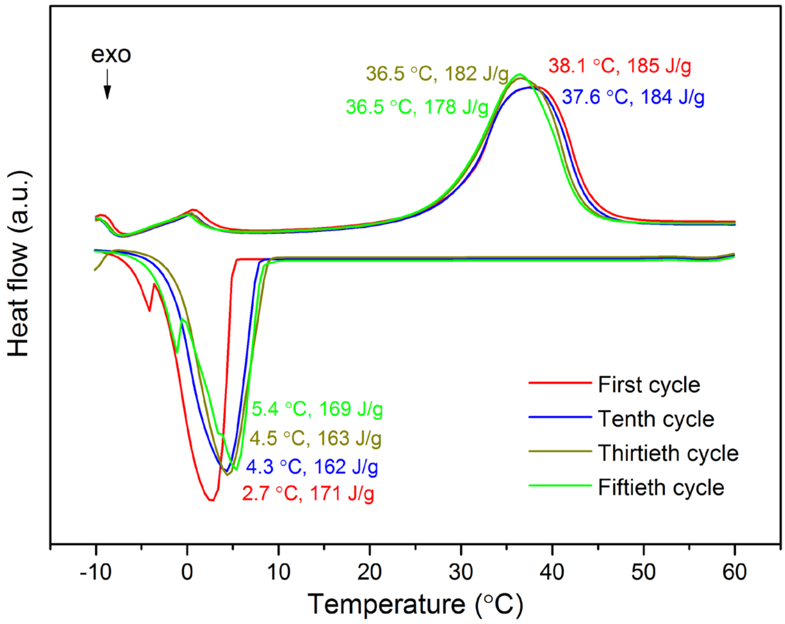

Fig. 7-11 Thermal cycling tests of 90% EHS@sepiolite for 50 cycles

7.3 Conclusions

In this study, sepiolite is applied as matrix material to load EHS (mass ratio 50% DHPD: 50% SDH) to form EHS@sepiolite FSPCM. Sepiolite has a long nanofibrous morphology with the average diameter of 30 nm, and the length ranging from 1 to 5µm. Inside the fibres, numerous nanochannels with size of 3.7 Å * 10.6 Å are present. The unique structure of sepiolite determines its characteristics of very high specific surface area of 156.82 $m^2 \cdot g^{-1}$ and big pore volume of 0.640 $cm^3 \cdot g^{-1}$, which enables its high loading capacity of PCM. Further, zeolitic structural water molecules in nannochannels and plenty of Si–OH groups on surface of fibres function as active hydrogen bonding sides to interact with hydrated salts. The EHS@sepiolite FSPCM with 88% effective loading is successfully fabricated. The structural characterisation shows the crystal structures of both sepiolite and EHS are well kept in the composite. No covalent bonding is formed between PCM and matrix. The composite has the high melting enthalpy of 185 $J{\cdot}g^{-1}$, and the melting temperature of 38.1 °C. The melting temperature is not obviously reduced comparing to the pure EHS, as big part of EHS is contained in the networks formed by sepiolite fibres and the nanoconfinement effect is not evident. The hydrogen bonding, the electronic interaction and the structural water in sepiolite make the phase change behaviour of the composite stable over thermal cycling. The melting enthalpy and the melting temperature are hardly changed over 50 heat uptake/release cycles. Considering the low cost and abundant reserve of sepiolite, the simple fabrication procedure, the high loading efficiency and the good cycling stability, EHS@sepiolite is FSPCM with big potential in thermal energy storage application in low temperature range.

Supplements

Tab. S7-1 DSC data from cycling tests of 50% EHS@sepiolite for 50 cycles

Cycle Nr.	Melting T (°C)	Melting Enthalpy ($J \cdot g^{-1}$)	Freezing T (°C)	Freezing Enthalpy ($J \cdot g^{-1}$)
1	33.8	95.2	-5.4	73.4
5	33.8	93.2	-6.0	70.4
10	33.8	93.4	-5.1	72.6
15	34	92.9	-5.8	71.4
20	34.2	93.0	-5.4	72.8
25	34.2	92.5	-6.0	71.8
30	34.4	93.2	-7.4	72.6
33	34.4	91.9	-11.5	70.4
40	34.5	91.7	-8.9	74.3
45	34.5	92.9	-6.7	74.5
50	34.5	93	-10.4	68.4

Tab. S7-2 DSC data from cycling tests of 60% EHS@sepiolite for 50 cycles

Cycle Nr.	Melting T (°C)	Melting Enthalpy ($J\cdot g^{-1}$)	Freezing T (°C)	Freezing Enthalpy ($J\cdot g^{-1}$)
1	35.7	119.6	0.8	88.5
5	35.4	118.5	0.8	88.8
10	35.5	118.7	0.9	90.4
15	35.6	116.9	3.0	90.7
20	35.7	118.4	1.6	90.3
25	35.7	117.1	-1.6	83.7
30	35.7	115.3	-1.1	86.2
33	35.5	115	-5.3	81.5
40	35.6	112.4	-4.9	81.3
45	35.6	112.2	-5.0	82.5
50	35.8	111.7	0.7	86.7

Tab. S7-3 DSC data from cycling tests of 70% EHS@sepiolite for 50 cycles

Cycle Nr.	Melting T (°C)	Melting Enthalpy ($J \cdot g^{-1}$)	Freezing T (°C)	Freezing Enthalpy ($J \cdot g^{-1}$)
1	36.4	139.9	1.1	107.8
5	36.7	137.6	-5.2	103.8
10	36.9	137.8	-0.5	110.2
15	37.1	134.7	-0.1	100.2
20	37.2	137.4	-1.7	106.3
25	37.2	135.5	-0.8	103.4
30	37.3	138.3	-0.9	106.8
33	37.4	136.1	-3.8	104.4
40	37.4	134.8	-0.9	106.1
45	37.5	138.6	-1.8	109.9
50	37.5	139.2	-0.3	105.7

Tab. S7-4 DSC data from cycling tests of 80% EHS@sepiolite for 50 cycles

Cycle Nr.	Melting T (°C)	Melting Enthalpy ($J \cdot g^{-1}$)	Freezing T (°C)	Freezing Enthalpy ($J \cdot g^{-1}$)
1	37.3	158.1	2.3	123.4
5	36.4	158.6	-0.9	128.2
10	36.4	152.5	2.8	133.9
15	36.3	157.4	1.2	137.9
20	36.2	154.9	3.0	132.3
25	36.2	151.9	2.4	135.2
30	36.1	152.6	4.7	132.7
33	35.7	156.2	-2.1	125.7
40	35.8	149.5	3.0	132
45	35.7	153.2	2.0	130.1
50	35.7	154.3	2.8	130.5

Tab. S7-5 DSC data from cycling tests of 90% EHS@sepiolite for 50 cycles

Cycle Nr.	Melting T (°C)	Melting Enthalpy ($J \cdot g^{-1}$)	Freezing T (°C)	Freezing Enthalpy ($J \cdot g^{-1}$)
1	38.1	185	2.7	170.9
5	38.1	181.1	-2.3	164.1
10	37.6	184	4.3	162.4
15	36.9	181.7	2.7	167.6
20	36.5	180.1	5.0	163.6
25	36.5	175.3	3.5	165.1
30	36.5	182.3	4.5	163.1
33	36.7	175.2	-1.7	160.5
40	36.5	175.5	5.0	165.6
45	36.4	176.9	4.1	165.2
50	36.5	178.2	5.4	168.9

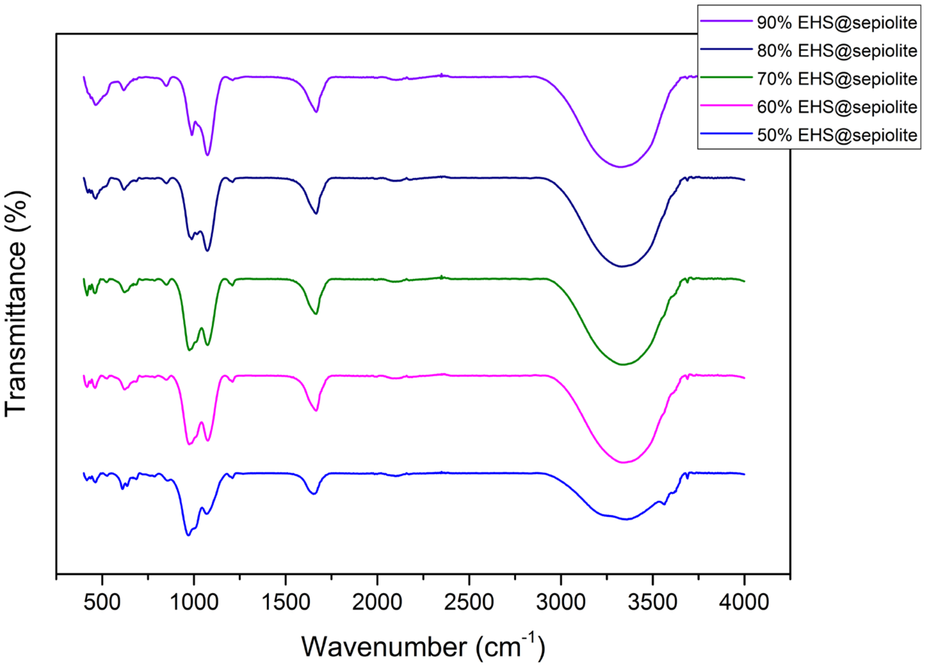

Fig. S7-1 FTIR spectra of EHS@sepiolite with various loadings

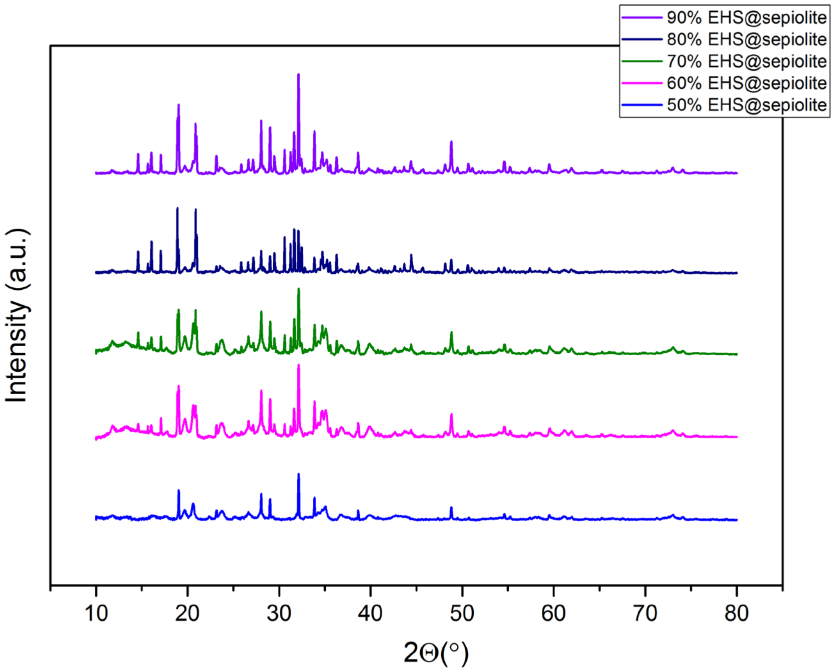

Fig. S7-2 XRD patterns of EHS@sepiolite with various loadings

References

[1] B.F. Jones, K.M. Conko, in *Developments Palygorskite-Sepiolite Research*, Elsevier **2011**, 69-83.

[2] G. Zhuang, J. Gao, H. Chen, Z. Zhang, *Appl. Clay Sci.* **2018**, *153*, 1.

[3] A. Sun, J.-B. d'Espinose de la Caillerie, J.J. Fripiat, *Microporous Mater.* **1995**, *5*, 135.

[4] A. Alvarez, in *Palygorskite - Sepiolite Occurrences, Genesis and Uses* Elsevier **1984**, 253-287.

[5] G. Tian, G. Han, F. Wang, J. Liang, *Sepiolite Nanomaterials: Structure, Properties and Functional Applications*, Elsevier **2019**.

[6] E. Galan, *Clay Miner.* **1996**, *31*, 443.

[7] Y. Ma, G. Zhang, *Chem. Eng. J.* **2016**, *288*, 70.

[8] M. Akkari, P. Aranda, C. Belver, J. Bedia, A. Ben Haj Amara, E. Ruiz-Hitzky, *Appl. Clay Sci.* **2018**, *160*, 3.

[9] F. Marrakchi, W.A. Khanday, M. Asif, B.H. Hameed, *Int. J. Biol. Macromol.* **2016**, *93*, 1231.

[10] S.C.R. Santos, R.A.R. Boaventura, *J. Environ. Chem. Eng.* **2016**, *4*, 1473.

[11] S. Jianli, N. Bo, *Non-Matallic Mines* **2014**, *5*, 11.

[12] Z. Guo, Y. Jia, X. Wang, *Research on the Capric Acid / Paraffin and Sepiolite Combination as Phase Change Energy Storage Materials*, the 7th Chinese National Conference on Functional Materials and Applications **2010**, 1927-1931

[13] J. Dahua, Z. Yunchao, S. Fan, R. Rushan, *Guangdong Chem Ind* **2010**, *7*, 37.

[14] F.R. Cannings, *J. Phys. Chem.* **1968**, *72*, 1072.

[15] R. Prost, *Spectrochim. Acta Part A Mol. Spectrosc.* **1975**, *31*, 1497.

[16] C. Serna, J.L. Ahlrichs, J.M. Serratosa, *Clays Clay Miner.* **1975**, *23*, 452.

[17] J.E. Post, D.L. Bish, P.J. Heaney, *Am. Mineral.* **2007**, *92*, 91.

[18] R.L. Frost, O.B. Locos, H. Ruan, J.T. Kloprogge, *Vib. Spectrosc.* **2001**, *27*, 1.

[19] M. Klähn, G. Mathias, C. Kötting, M. Nonella, J. Schlitter, K. Gerwert, P. Tavan, *J. Phys. Chem. A* **2004**, *108*, 6186.

[20] M. Falk, T.A. Ford, *Can. J. Chem.* **1966**, *44*, 1699.

8. Nanoencapsulation of liquid metal phase change material

8.1 Introduction

Liquid metal is a new class of phase change material (PCM) with different properties to traditional phase change material. Due to its relative high price and less availability than traditional PCMs such as hydrated salts and organic phase change material (OPCM), it would be in the first sight not taken as economical PCM. However, as the demand on coolant to electronic devices is rising in recent years[1], this type of PCMs shows inherent superiority to other PCMs. Thanks to its high thermal conductivity[2], considerable heat dissipated from electronic devices could be transferred instantaneously, which avoids the damage of devices by accumulated heat and increases the use security as well as the working time. Due to its stable chemical structure and very high evaporation point[3], this material does not get degraded during the solid-liquid phase transition, which guarantee its long life span and economic benefit as PCM. Gallium and gallium-based metal alloys have been reported as PCM in thermal management of electronic devices[4]-[6]. With low melting temperature, high melting enthalpy, high thermal conductivity and good thermal stability their performances as PCM are proved to be excellent.

Liquid metal is often used as block material filled in heat sinks in previous studies as PCM[7]-[10]. The encapsulation, especially nanoencapsulation of liquid metal is rarely reported. Blaiszik et al.[11] made microcapsules with gallium-indium core and urea-formaldehyde shell in large sizes from 3 to 245 µm. These microcapsules were used for self-healing, not as phase change material. The encapsulation of liquid metal could prevent its leakage on melting and make the incorporation into the target device facile. Also, the nanoencapsulated liquid metal can be added to thermal fluid such as water or poly-α-olefin to extend the applicable scenes[12]. In this study, the eutectic gallium-indium alloy (EGaIn) with the melting point of 20 °C was utilised as PCM core material. Nanocapsules with gelatine, the electronic polymers poly(sodium 4-styrenesulfonate) (PSS)-poly(diallyldimethyl ammonium chloride) (PDADMAC) and inorganic SiO_2 as shell materials were fabricated, respectively. Nanocomposite with halloysite as nanocontainers was also formed. The morphology, chemical composition and phase change properties of each nanoencapsulated EGaIn system were studied.

8.2 Gelatine nanocapsules with eutectic Ga-In as phase change material

8.2.1 Experimental part

8.2.1.1 Chemicals and instruments

The chemical reagents applied in the fabrication of gelatine nanocapsules with eutectic Ga-In PCM (EGaIn@gelatine) are listed in Tab. 8-1.

Tab. 8-1 Chemical reagents for the fabrication of EGaIn@gelatine

Reagent	Purity/Form	Supplier
Gelatine	Reagent grade, Type A, powder, gel strength 300 g Bloom	Sigma, China
Eutectic gallium-indium alloy (EGaIn)	≧99.99%, 70% Ga and 30% In	Sigma, China
poly-α-olefin (PAO)	Reagent grade, 98%	Aladdin, China
Ethanol	Reagent grade, 99%	Aladdin, China

All the reagents were used as purchased without further purification. Milli Q water has been used in the washing process.

The instruments used for the fabrication and characterisation of EGaIn@gelatine samples are shown in Tab. 8-2.

Tab. 8-2 Instruments for the fabrication and characterisation of EGaIn@gelatine

Instrument	Model	Supplier
Ultrasonic processor	Fisher Scientific 505	Thermo Fisher Scientific, USA
Centrifuge	Sigma 1-16	Sigma, Germany
Scanning electron microscopy (SEM)	FEI-Apreo SEM	Thermo Fisher Scientific, USA
Energy-dispersive X-ray spectroscopy (EDS)	FEI-Apreo SEM	Thermo Fisher Scientific, USA
Fourier transform infrared spectroscopy (FTIR)	TENSOR II	Bruker, Germany
Raman spectroscopy (Raman)	inVia^{TM} confocal Raman microscope	Renishaw, UK
Differential scanning calorimeter (DSC)	214 NETZSCH	NETZSCH, Germany

8.2.1.2 Procedure and characterisation

20 mg EGaIn was added in 10 mL Poly-α-olefin (PAO) and sonicated by 30% amplitude for 10 min. Homogeneous dark grey suspension was obtained. The gelatine solution obtained by dissolving 20 mg gelatine in 2 mL H_2O at 45°C was added to EGaIn suspension. The mixture was stirred at 1000 rpm for 10 min to deposit gelatine on the surface of the nanoparticles. After stirring, it was kept still for 5 min at R.T. No precipitate was formed. Then the suspension was heated to 140 °C. After stirring for 10 min at 140 °C, the sample was cooled down to R.T. In the following, it was centrifuged (4000 rpm, 5min) and washed with ethanol. After dried in the air for 24 hours, dark grey powder as end product was obtained.

The morphology of the sample was characterised by scanning electron microscopy (SEM). SEM images were recorded by FEI-Apreo. The samples were sputter coated by 100 nm chromium layer before measuring. Energy-dispersive X-ray spectroscopy (EDS) was used for elemental analysis. Fourier transform infrared spectroscopy (FTIR) were obtained by TENSOR II instrument (Bruker, Germany). The transmittance mode was recorded in the wavenumber range from 400 to 4000 cm^{-1} with 64 consecutive scans. The phase change properties including cycling tests were characterised by differential scanning calorimeter (DSC). The instrument 214 NETZSCH (NETZSCH, Germany) was applied. The measurements were undertaken in the temperature range of -20 to 50 °C with the ramp of under nitrogen atmosphere. The Raman spectroscopy was carried out by inVia^{TM} confocal Raman microscope (Renishaw, UK). The pattern was recorded in the wavenumber range from 100 to 3200 cm^{-1}. The DSC and Raman measurements were carried out by technician.

8.2.2 Results and discussions

The SEM images of EGaIn@gelatine nanocapsules are shown in Fig. 8-1. The size of the particles ranges from 70 nm to 1 μm. Each particle is distinguishable, although aggregation of particles is observed. The shape of particles keeps stable. Gel-like shell is found on the surface of nanoparticles. No blocks of white gel material are observed. Gelatine should deposite successfully on the nanoparticles.

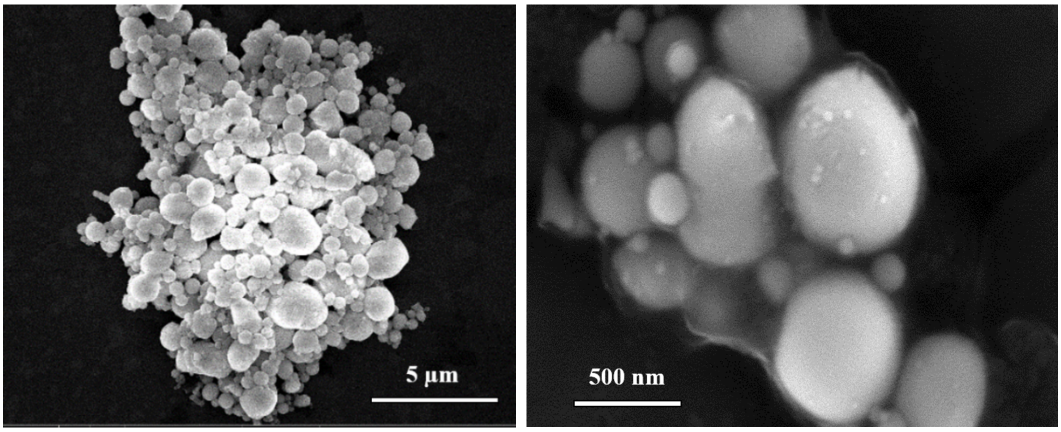

Fig. 8-1 SEM images of EGaIn@gelatine with magnification of (a) *8000 (b)*80000

The EDS of EGaIn@gelatine nanocapsules is shown in Fig. 8-2. The elements of Ga, In from the EGaIn are detected. Gelatine exhibits the elements C, N, O. However, the holder surface also contains C. It is not conclusive from EDS, gelatine is included in the capsules.

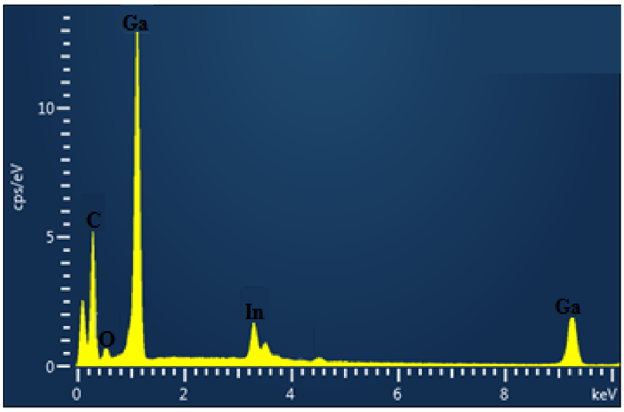

Fig. 8-2 EDS spectrum of EGaIn@gelatine

The FTIR spectrum of EGaIn@gelatine is shown in Fig. 8-3. No obvious peak can be assigned to the liquid metal. Two aspects should be taken into consideration. One is the metal-metal bonds absorbs light in the Far-IR range below 600 cm^{-1}, which needs a special Far-IR set-up for the measurement. In case of the oxidation of the metal surface, the metal-oxide cannot be characterised by standard FTIR technique[13]. The small peak at 1620 cm^{-2} can be attributed to the C=O stretching of amide group from gelatine.

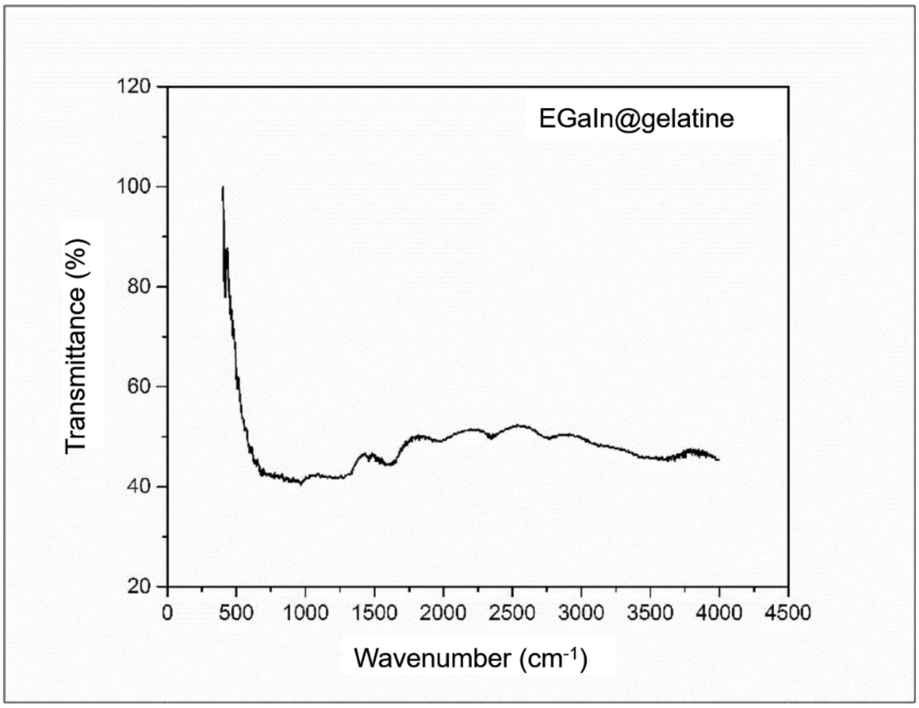

Fig. 8-3 FTIR spectrum of EGaIn@gelatine

The Raman spectrum of EGaIn@gelatine in Fig. 8-4 shows no characteristic peaks.

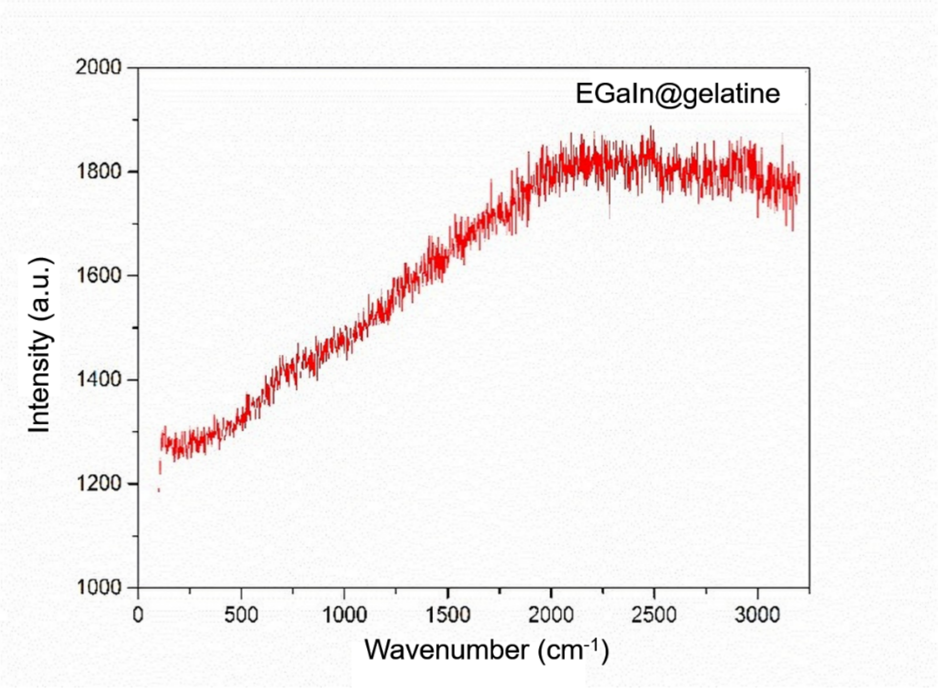

Fig. 8-4 Raman spectrum of EGaIn@gelatine (collected from technician)

The phase change behaviours of pure EGaIn as block material and EGaIn@gelatine capsules are displayed in the DSC curves in Fig. 8-5. Four heat uptake/release cycles were recorded for each sample. The DSC data of EGaIn block material is summarized in Tab. 8-3. The pure EGaIn block shows identical melting behaviour for all cycles, with the melting temperature of 20 °C and the high melting enthalpy of 355 J·g^{-1}. Supercooling is observed by EGaIn, as the freezing temperatures were around -10 °C. In comparison, EGaIn@gelatine capsules show no phase change peak. The small peaks in the beginning and end of the phase change curves are due to change of measurement condition and should not be considered.

Oxidation should be occurred on the surface of EGaIn. In case of block EGaIn, the oxidized surface layer is rather small and thin. The high phase change enthalpy is from the inner part of EGaIn, which is protected from the oxidation by the surface oxide layer. By EGaIn@gelatine nanocapsules, the surface area is largely increased and the oxidization of EGaIn could be enhanced by sonication in the fabricating process. The phase change property of liquid metal is thus lost.

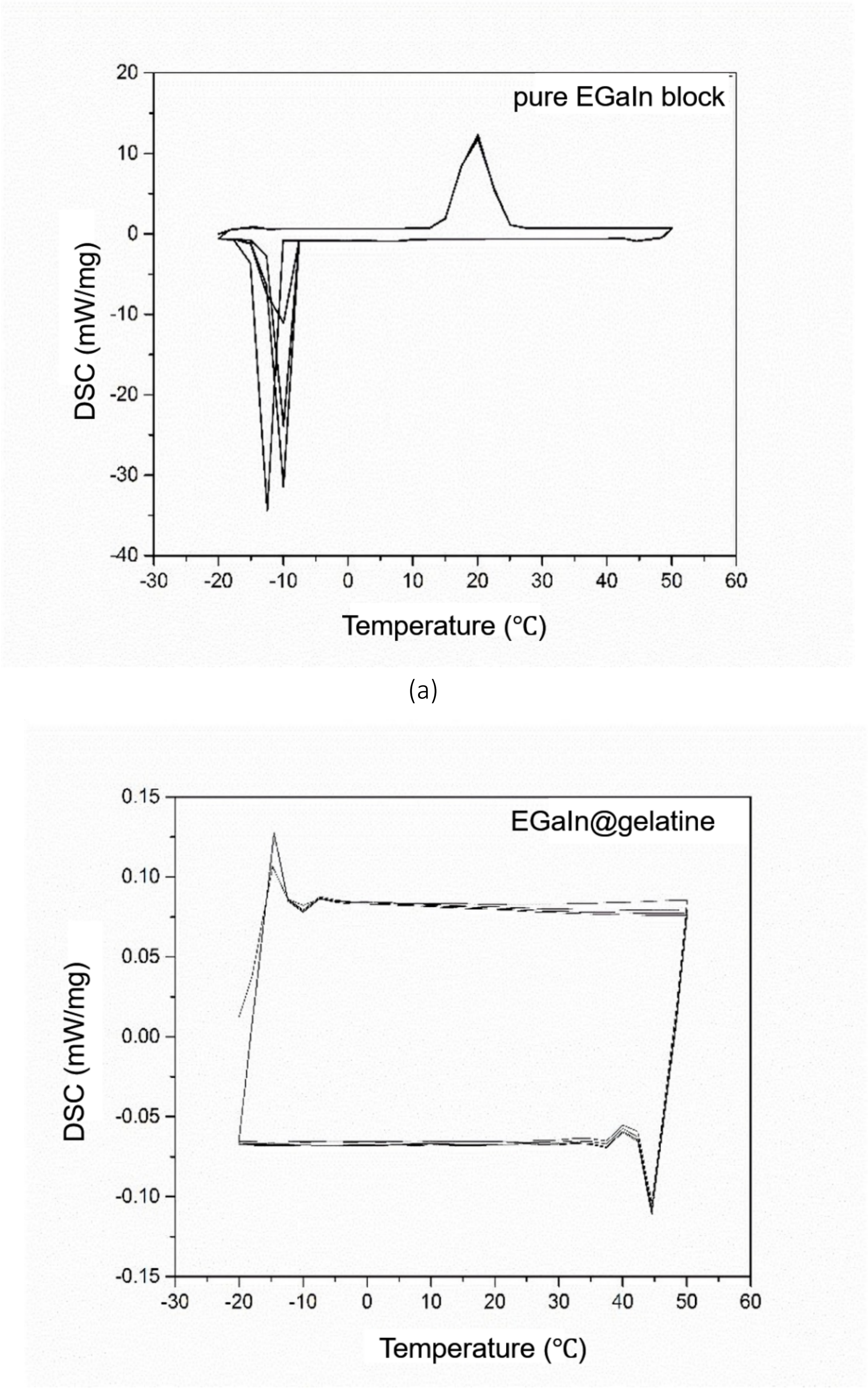

(a)

（b）

Fig. 8-5 DSC curves of (a) pure EGaIn block (b) EGaIn@gelatine (collected from technician)

Tab. 8-3 DSC data from cycling tests of EGaIn block material

Cycle Nr.	Melting T (°C)	Melting Enthalpy ($J\cdot g^{-1}$)	Freezing T (°C)	Freezing Enthalpy ($J\cdot g^{-1}$)
1	20	355	-13	350
2	20	355	-10	331
3	20	355	-10	282
4	20	355	-10	254

8.2.3 Conclusions

In this section, EGaIn@gelatine nanocapsules were fabricated by depositing gelatine on EGaIn nanoparticles and subsequently denaturating the gelatine shell by heating. The nanocapsules have stable morphology with size in the range of 70 nm to 1 µm. However, the phase change property of EGaIn disappears by EGaIn@gelatine nanocapsules. The possible reason is the oxidation of the liquid metal.

8.3 Poly(sodium 4-styrenesulfonate)-poly(diallyldimethyl ammonium chloride) nanocapsules with eutectic Ga-In as phase change material

8.3.1 Experimental part

8.3.1.1 Chemicals and instruments

The chemical reagents applied in the fabrication of poly(sodium 4-styrenesulfonate)-poly(diallyldimethyl ammonium chloride) nanocapsules with eutectic Ga-In PCM (EGaIn@poly(sodium 4-styrenesulfonate)-poly(diallyldimethyl ammonium chloride)) are listed in Tab. 8-4. All the reagents were used as purchased without further purification. Milli Q water has been used in the washing process.

Tab. 8-4 Chemical reagents for the fabrication of EGaIn@poly(sodium 4-styrene sulfonate)-poly(diallyldimethyl ammonium chloride)

Reagent	Purity/Form	Supplier
poly(sodium 4-styrenesulfonate) (PSS)	powder	Sigma, China
poly(diallyldimethyl ammonium chloride) (PDADMAC)	20 wt% in H_2O	Sigma, China
EGaIn	≧99.99%, 70% Ga and 30% In	Sigma, China
poly-α-olefin	Reagent grade, 98%	Aladdin, China
Ethanol	Reagent grade, 99%	Aladdin, China

The instruments for the fabrication and characterisation of EGaIn@poly(sodium 4-styrenesulfonate)-poly(diallyldimethyl ammonium chloride) include all from Tab. 8-2 and a digital pen pH meter (PH30, Cunye Shanghai).

8.3.1.2 Procedure and characterisation

20 mg EGaIn was dispersed in 10 mL poly-α-olefin, and sonicated by 30% amplitude for 10 min. The homogeneous dark grey suspension was obtained. The suspension was centrifuged (4000 rpm, 5 min) and the obtained nanoparticles were washed with ethanol. Then, they were dispersed in 5 mL water. 10 mL 20 mg·mL^{-1} poly(sodium 4-styrenesulfonate) (PSS) in H_2O solution was added. The pH value of the mixture was 6.7. The sample was stirred at 600 rpm for 1h. After that it was centrifuged (4000 rpm, 10 min) and washed with water. Subsequently, 10 mL 20 mg·mL^{-1} poly(diallyldimethyl ammonium chloride) (PDADMAC) in H_2O solution was added. The pH value was 3.7. After stirring at 600 rpm for 1h, the sample was centrifuged and washed. The above procedure of depositing poly(sodium 4-styrenesulfonate) and poly(diallyldimethyl ammonium chloride) was repeated three times. The final product was obtained after drying for 24 hrs at R.T.

The characterisation techniques of EGaIn@poly(sodium 4-styrenesulfonate)-poly(diallyldimethyl ammonium chloride) are the same as described in 8.2.1.2.

8.3.2 Results and discussions

The SEM images of EGaIn@poly(sodium 4-styrenesulfonate)-poly(diallyldimethyl ammonium chloride) are shown in Fig. 8-6. Nanoparticles with sizes ranging from 180 nm to 1.15 µm are observed. The shape of single nanoparticle keeps stable during the SEM measurement.

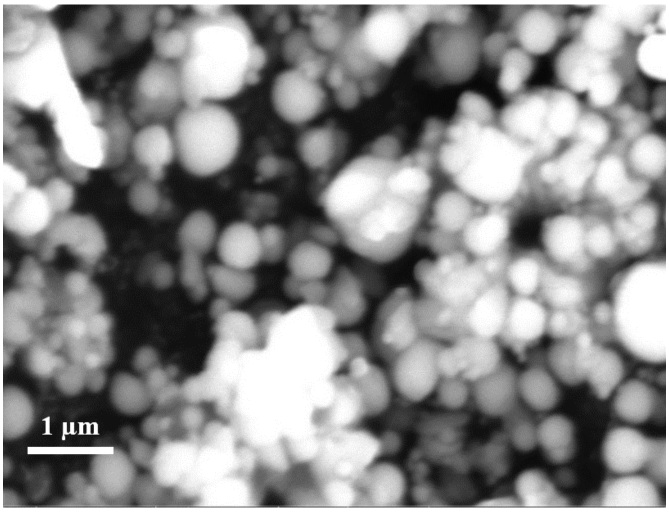

Fig. 8-6 SEM image of EGaIn@poly(sodium 4-styrenesulfonate)-poly(diallyldimethyl ammonium chloride)

The EDS of EGaIn@poly(sodium 4-styrenesulfonate)-poly(diallyldimethyl ammonium chloride) is shown in Fig. 8-7. The elements Ga, In are from the EGaIn. The element S from poly(sodium 4-styrenesulfonate) and N from poly(diallyldimethyl ammonium chloride) have not been detected, which could be due to the low concentration of the element. Further characterisations of FTIR and Raman are needed to verify the presence of poly(sodium 4-styrenesulfonate) and poly(diallyldimethyl ammonium chloride) in sample.

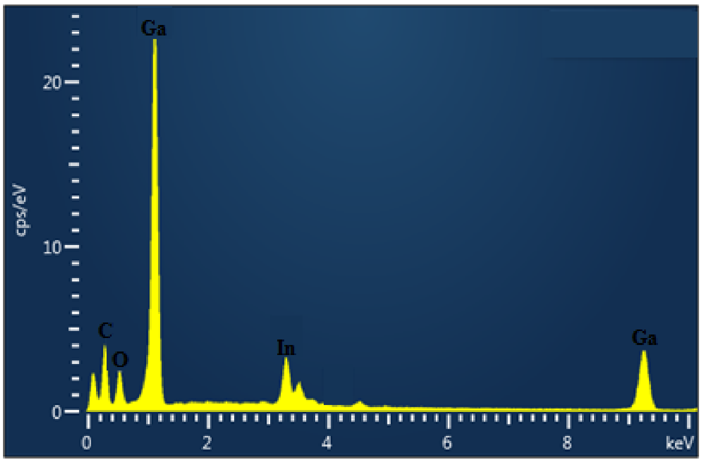

Fig. 8-7 EDS of EGaIn@poly(sodium 4-styrenesulfonate)-poly(diallyldimethyl ammonium chloride)

The FTIR spectrum of EGaIn@poly(sodium 4-styrenesulfonate)-poly(diallyldimethyl ammonium chloride) as shown in Fig. 8-8 exhibits no characteristic peak.

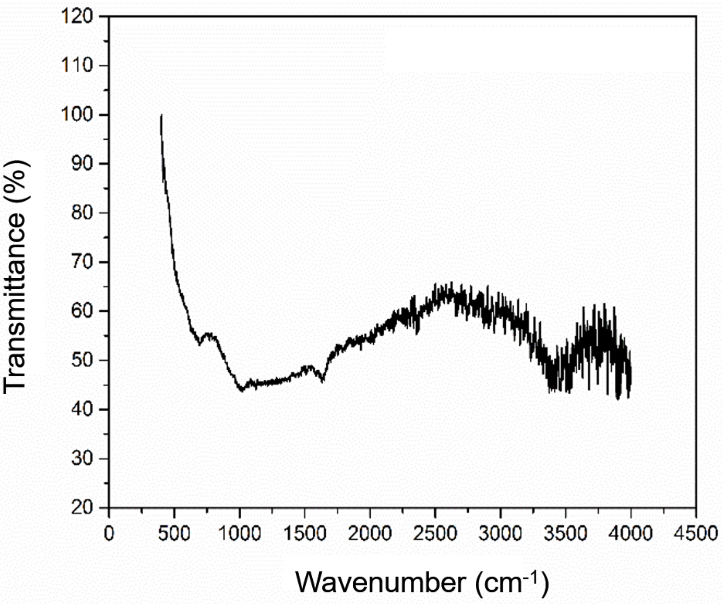

Fig. 8-8 FTIR spectrum of EGaIn@poly(sodium 4-styrenesulfonate)-poly(diallyldimethyl ammonium chloride)

The Raman spectrum of EGaIn@poly(sodium 4-styrenesulfonate)-poly(diallyldimethyl ammonium chloride) is shown in Fig. 8-9. Obvious peaks in the spectrum can be attributed to poly(sodium 4-styrenesulfonate) (PSS)[14]-[17] and poly(diallyldimethyl ammonium chloride) (PDADMAC)[18][19], as tabulated in Tab. 8-5. In the wavenumber range from 100 to 600 cm^{-1}, the peak at 454 cm^{-1} is assigned to poly(diallyldimethyl ammonium chloride) ring and chain skeletal deformation[19]. Characteristic peaks of PSS can be detected at 1035 and 1458 cm^{-1}. The peak at 1035 cm^{-1} is from sulfonate ion[14]-[16], and the peak at 1458 cm^{-1} is from the aromatic CCH quadrant stretching[14][17]. The Raman pattern in the range from 2500 to 3000 cm^{-1} can be assigned to PDADMAC. The peaks at 2838 and 2882 cm^{-1} are due to the CH_2-chain symmetric stretching mode [19]. The peak at 2963 cm^{-1} is from the CH_2-ring asymmetric stretching mode [19].

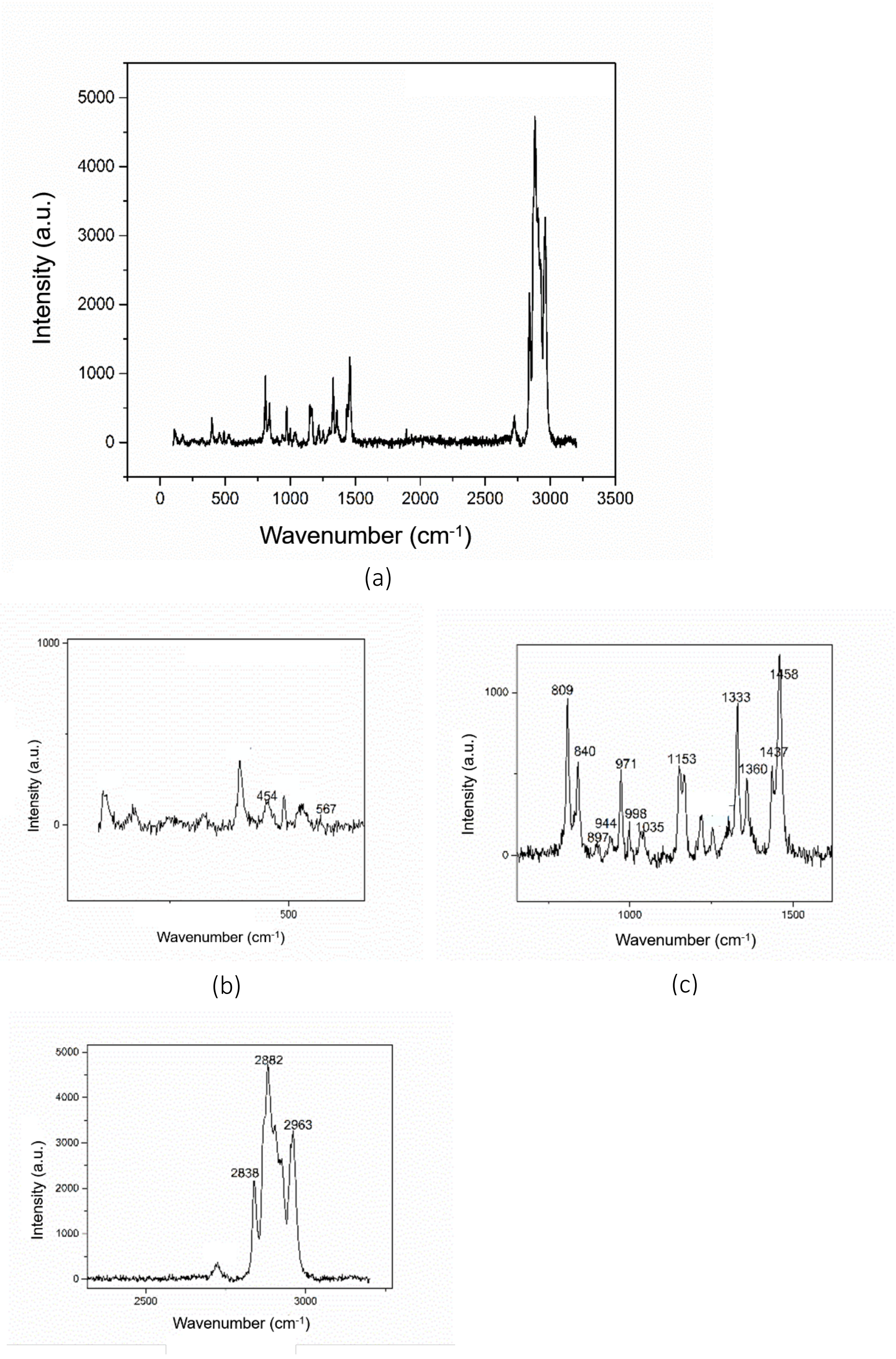

(a)

(b)

(c)

(d)

Fig. 8-9 Raman spectrum of EGaIn@poly(sodium 4-styrenesulfonate)-poly(diallyldimethyl ammonium chloride) with wavenumber range of (a) 100 -3200 cm^{-1} (b) 100-600 cm^{-1} (c) 600-1600 cm^{-1} (d) 2250-3250 cm^{-1} (collected from technician)

Tab. 8-5 Tabulation of RAMAN peaks of EGaIn@poly(sodium 4-styrenesulfonate)-poly(diallyldimethyl ammonium chloride)[14]–[19]

Peak position (cm^{-1})	454	567	809	840
Assignment	PDADMAC ring + chain skeletal deformation	PDADMAC CH_3-N-CH_3 scissoring	PDADMAC CH_2 chain rocking + C-N stretching	PDADMAC CH_2 cycle rocking + C-C ring stretching
Peak position (cm^{-1})	897	971	998	1333
Assignment	PDADMAC ring breathing	PDADMAC ring deformation + C−N stretching	PDADMAC skeletal C−C stretching mode	PDADMAC CH_2 chain twisting
Peak position (cm^{-1})	1035	1153	1458	1360
Assignment	PSS -SO_3^- stretching	PSS -SO stretching	PSS aromatic CCH quadrant stretching	PSS –CH_3 bending
Peak position (cm^{-1})	2838	2882	2963	
Assignment	PDADMAC CH_2 chain sym. stretching	PDADMAC CH_2 chain sym. stretching	PDADMAC CH_2 ring asym. stretching	

The DSC curves of EGaIn@poly(sodium 4-styrenesulfonate)-poly(diallyldimethyl ammonium chloride) are shown in Fig. 8-10. No melting or freezing peaks are observed over thermal cycling.

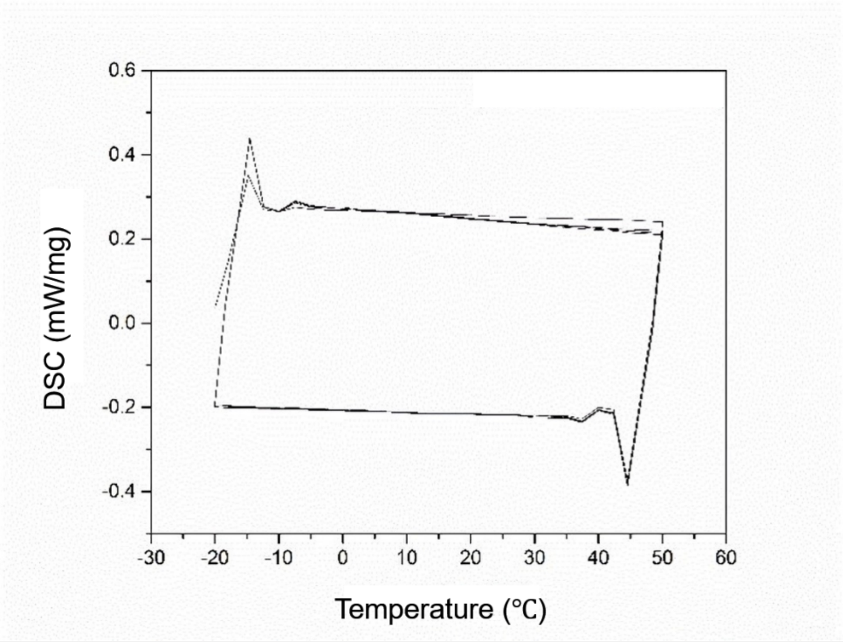

Fig. 8-10 DSC curves of EGaIn@poly(sodium 4-styrenesulfonate)-poly(diallyldimethyl ammonium chloride) (collected from technician)

8.3.3 Conclusions

EGaIn@poly(sodium 4-styrenesulfonate)-poly(diallyldimethyl ammonium chloride) nanocapsules have been fabricated using layer-by-layer deposition of anionc polyelectrolyte PSS and cationic polyelectrolyte poly(diallyldimethyl ammonium chloride). The EDS verified the elements from EGaIn, poly(sodium 4-styrenesulfonate) and poly(diallyldimethyl ammonium chloride). The presentation of polymer poly(sodium 4-styrenesulfonate)-poly(diallyldimethyl ammonium chloride) in the nanoparticles is also detected by Raman spectrum. However, the phase change property of EGaIn has been lost in EGaIn@poly(sodium 4-styrenesulfonate)-poly(diallyldimethyl ammonium chloride) sample. EGaIn should be oxidized during the composite nanocapsules fabrication process.

8.4 Silica nanocapsules with eutectic Ga-In as phase change material

8.4.1 Experimental part

8.4.1.1 Chemicals and instruments

The chemical reagents applied in the fabrication of silica nanocapsules with eutectic Ga-In PCM (EGaIn@SiO_2) are listed in Tab. 8-6. All the reagents were used as purchased without further purification. Milli Q water has been used in the washing process.

Tab. 8-6 Chemical reagents for the fabrication of EGaIn@SiO_2

Reagent	Purity/Form	Supplier
Tetraethyl orthosilicate	GC, ≧99.5%	Sigma, China
EGaIn	≧99.99%, 70% Ga and 30% In	Sigma, China
Poly-α-olefin	Reagent grade, 98%	Aladdin, China
Ethanol	Reagent grade, 99%	Aladdin, China
Ammonia solution	28% NH_3 in H_2O	Aladdin, China

The instruments used for fabrication and characterisation of EGaIn@SiO_2 are as described in Tab. 8-2.

8.4.1.2 Procedure and characterisation

100 mg EGaIn in 50 mL poly-α-olefin was sonicated by 30% amplitude for 15 min to obtain the homogeneous dark grey suspension. The suspension was poured into 200 mL ethanol. The mixture was centrifuged (4000 rpm, 5 min) to separate nanoparticles, which were subsequently washed with ethanol. Then, the nanoparticles were dispersed in 100 mL ethanol. 0.4 mL tetraethyl orthosilicate (TEOS) and 4 mL 28wt% ammonia solution were added dropwise in the nanoparticles dispersion. The mixture was stirred

at 800 rpm under 70 °C for 1.5 h in oil bath. After centrifuging and washing with ethanol, the sample was dried in the air for 24 h. Grey powder was obtained as final product. The characterisation techniques of EGaIn@SiO_2 are the same as described in 8.2.1.2.

8.4.2 Results and discussions

The SEM image of EGaIn@SiO_2 is shown in Fig. 8-11. Micro/nanocapsules are formed with size ranging from 100 nm to 1.8 µm. The shape of each single particle is stable. No obvious aggregation of nanoparticles is observed.

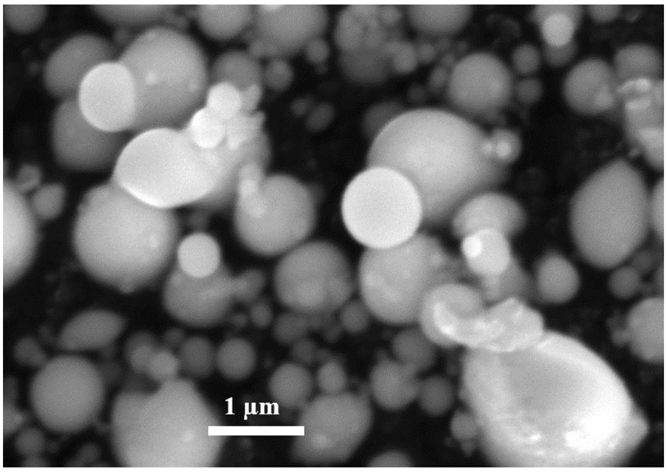

Fig. 8-11 SEM image of EGaIn@SiO_2

The EDS of EGaIn@SiO_2 in Fig. 8-12 shows the presence of elements Ga, In from EGaIn and Si, O from SiO_2.

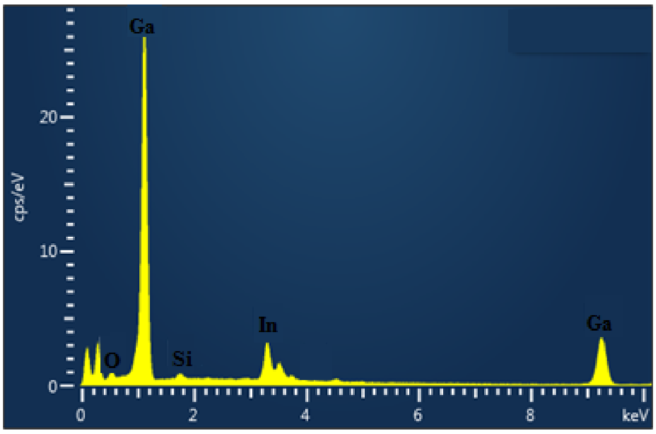

Fig. 8-12 EDS of EGaIn@SiO_2

The FTIR spectrum of EGaIn@SiO_2 shows no characteristic peak (Fig. 8-13).

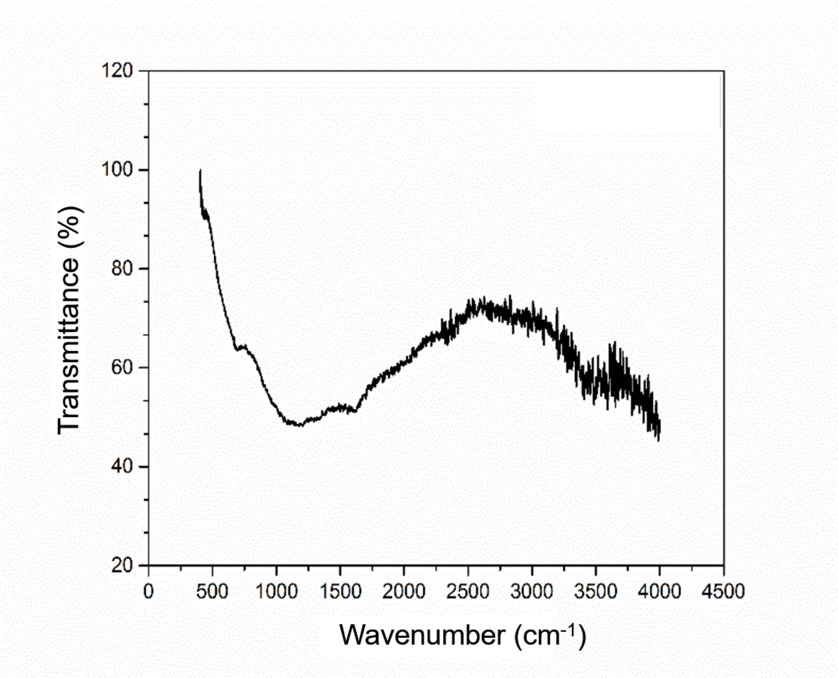

Fig. 8-13 FTIR spectrum of EGaIn@SiO_2

The Raman spectrum of EGaIn@SiO_2 (Fig. 8-14) shows no characteristic peak.

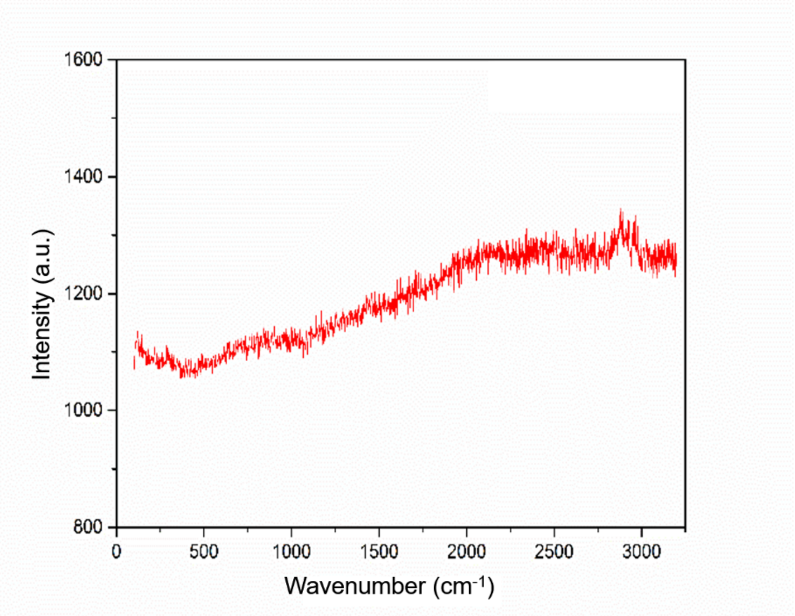

Fig. 8-14 Raman spectrum of EGaIn@SiO_2 (collected from technician)

The DSC curves of EGaIn@SiO_2 in Fig. 8-15 shows the sample has lost its phase change property, which should be from the oxidation of EGaIn during the sample preparation.

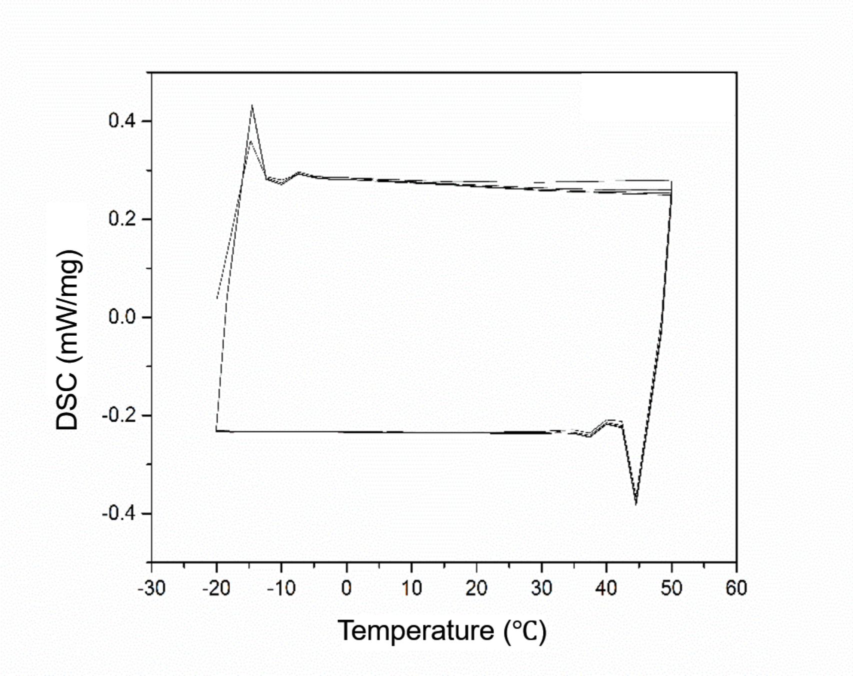

Fig. 8-15 DSC curves of EGaIn@SiO_2 (collected from technician)

8.4.3 Conclusions

EGaIn@SiO_2 micro/nanocapsules have been fabricated by sol-gel method. The formation of SiO_2 shell is proved by EDS. However, the sample does not exhibit any phase change property. EGaIn should have been oxidized during the fabrication of EGaIn@SiO_2.

8.5 Halloysite form-stable eutectic Ga-In phase change material

8.5.1 Experimental part

8.5.1.1 Chemicals and instruments

The chemical reagents applied in the fabrication of halloysite form-stable eutectic Ga-In PCM (EGaIn@halloysite) are listed in Tab. 8-7. All the reagents were used as purchased without further purification. Milli Q water has been used in the washing process.

Tab. 8-7 Chemical reagents for the fabrication of EGaIn@halloysite

Reagent	Purity/Form	Supplier
Halloysite	Nano powder	Sigma, China
EGaIn	≧99.99%, 70% Ga and 30% In	Sigma, China
Poly-α-olefin	Reagent grade, 98%	Aladdin, China
Ethanol	Reagent grade, 99%	Aladdin, China

The instruments for the fabrication and characterisation of EGaIn@halloysite are the same as described in 8.2.1.2. The vacuum oven used is model 450 (Goldbrunn, UK).

8.5.1.2 Procedure and characterisation

40 mg EGaIn was dispersed in 10 mL poly-α-olefin by sonication under 30% amplitude for 10 min. Homogeneous dark grey suspension was obtained. Subsequently, 40 mg of halloysite was added into the suspension. The mixture was sonicated at 30% amplitude for 30 s and a homogeneous suspension was obtained. Then, the suspension was put under vacuum for 10 min and exposed to the air. The process was repeated twice. Next, the suspension was dispersed in 100 mL ethanol. The mixture was centrifuged (4000 rpm, 5 min), washed with ethanol and dried at R.T. overnight. Light grey powder was finally obtained.

The conditions for the characterisation techniques were as described in 8.2.1.2.

8.5.2 Results and discussions

The SEM images of EGaIn@halloysite are shown in Fig. 8-16. Bright nanoparticles are randomly distributed among aggregate of halloysite nanorods. Large quantity of EGaIn is not impregnated into halloysite nanotubes.

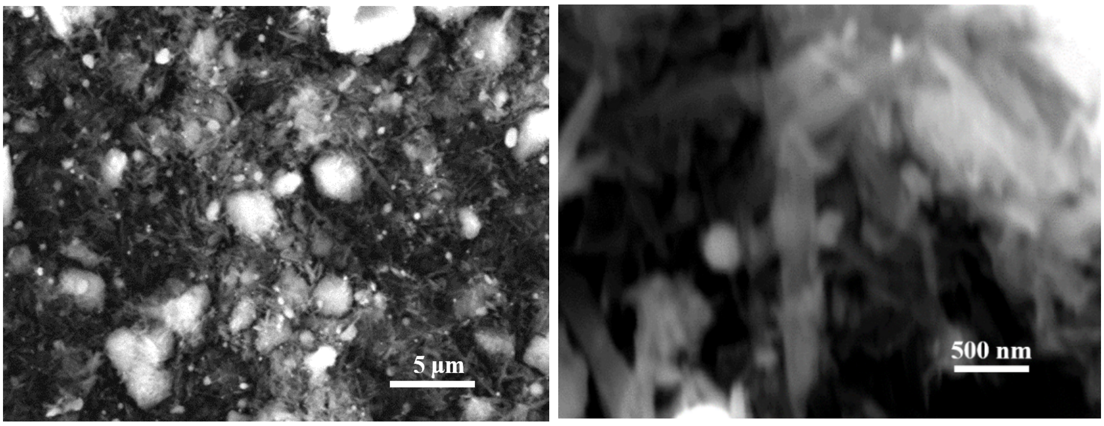

Fig. 8-16 SEM images of EGaIn@halloysite

The EDS of EGaIn@halloysite is shown in Fig. 8-17. The elements Ga, In are from EGaIn, and Al, Si are from the halloysite.

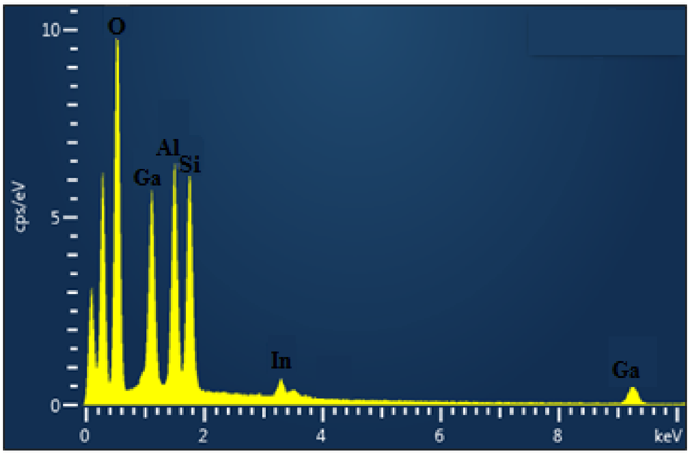

Fig. 8-17 EDS of EGaIn@halloysite

As shown in Fig. 8-18, EGaIn@halloysite shows the same FTIR pattern as halloysite, as the liquid metal is not IR active. The chemical structure of halloysite retains in EGaIn@halloysite.

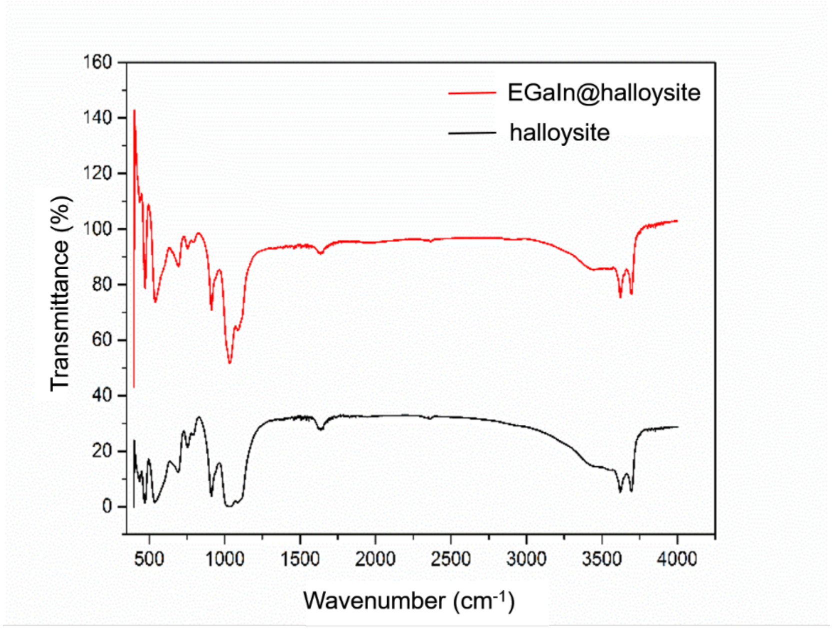

Fig. 8-18 FTIR spectra of EGaIn@halloysite and halloysite

Also, the XRD pattern of EGaIn@halloysite is the same as halloysite, as displayed in Fig. 8-19. Liquid metal shows no XRD peak. The crystallinity of halloysite keeps well in the composite.

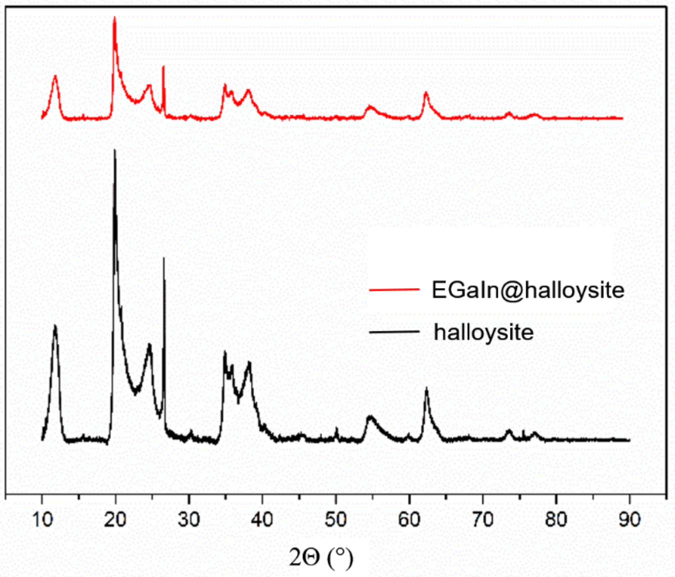

Fig. 8-19 XRD patterns of EGaIn@halloysite and halloysite

EGaIn@halloysite composite shows no phase change peaks in the DSC curves, as shown in Fig. 8-20. EGaIn should be oxidized during the fabrication of the composite.

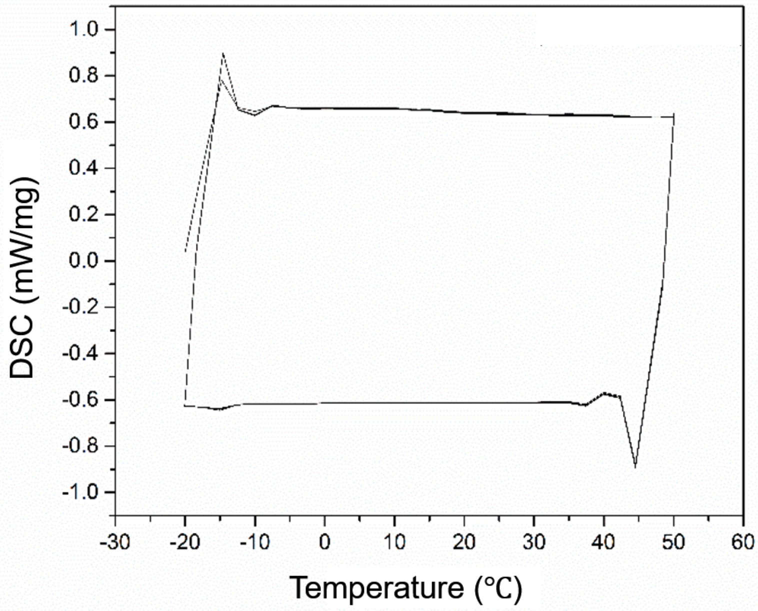

Fig. 8-20 DSC curves of EGaIn@halloysite (collected from technician)

8.5.3 Conclusions

EGaIn@halloysite composite fabricated by vacuum impregnation shows a mixture of liquid metal micro/nanoparticles and halloysite nanotubes. The halloysite has kept its chemical structure and crystallinity well in the composite. The EGaIn should be oxidized and lose the phase change property in the composite.

8.6 Summary

In this chapter, three types of nanocapsules: EGaIn@gelatine, EGaIn@poly(sodium 4-styrenesulfonate)-poly(diallyldimethyl ammonium chloride), EGaIn@SiO_2 were fabricated by various methods according to the correspondent shell material. In all three cases, good morphology of nanoparticles was obtained. By EGaIn@SiO_2, the elements from EGaIn and shell material were detected. In case of EGaIn@poly(sodium 4-styrenesulfonate)-poly(diallyldimethyl ammonium chloride), the shell material of poly(sodium 4-styrenesulfonate) and poly(diallyldimethyl ammonium chloride) layers was verified by Raman spectrum. However, the phase change property of EGaIn was lost in all types of nanocapsules. By the composite EGaIn@halloysite, the liquid metal was not well impregnated in halloysite nanotubes. It is suspected, due to the high portion of Ga, the applied EGaIn could easily get oxidized when sonicated or stirred in the air, which leads to the loss of the phase change property of the liquid metal.

References

[1] B. Agostini, M. Fabbri, J.E. Park, L. Wojtan, J.R. Thome, B. Michel, *Heat Transf. Eng.* **2007**, *28*, 258.

[2] G. Bo, L. Ren, X. Xu, Y. Du, S. Dou, *Adv. Phys. X* **2018**, *3*, 412.

[3] N. Greenwood, A. Earnshaw, *Chemistry of the Elements*, Elsevier **1997**, 216.

[4] Y. Zhao, S. Thapa, L. Weiss, Y. Lvov, *Adv. Eng. Mater.* **2014**, *16*, 1391.

[5] H. Ge, J. Liu, *Front. Energy* **2012**, *6*, 207.

[6] H. Ge, J. Liu, *J. Heat Transfer* **2013**, *135*, 054503.

[7] S. Krishnan, S. V. Garimella, S.S. Kang, *Thermomechanical Phenom. Electron. Syst. -Proceedings Intersoc. Conf.* **2004**, *1*, 310.

[8] R. Kandasamy, X.Q. Wang, A.S. Mujumdar, *Appl. Therm. Eng.* **2008**, *28*, 1047.

[9] R. Kandasamy, X.-Q. Wang, A.S. Mujumdar, *Appl. Therm. Eng.* **2007**, *27*, 2822.

[10] X.-Q. Wang, C. Yap, A.S. Mujumdar, *Int. J. Therm. Sci.* **2008**, *47*, 1055.

[11] B.J. Blaiszik, A.R. Jones, N.R. Sottos, S.R. White, *J. Microencapsul.* **2014**, *31*, 350.

[12] A. Jamekhorshid, S.M. Sadrameli, M. Farid, *Renew. Sustain. Energy Rev.* **2014**, *31*, 531.

[13] C. Yang, C. Wöll, *Adv. Phys. X* **2017**, *2*, 373.

[14] H.G.M. Edwards, I.R. Lewis, *J. Mol. Struct.* **1993**, *301*, 37.

[15] H.G.M. Edwards, D.N. Smith, *J. Mol. Struct.* **1990**, *238*, 27.

[16] H.G.M. Edwards, *Spectrochim. Acta Part A Mol. Spectrosc.* **1989**, *45*, 715.

[17] D. Lin-Vien, N.B. Colthup, W.G. Fateley, J.G. Grasselli, *Infrared and Raman Characteristic Frequencies of Organic Molecules*, Academic Press **1991**.

[18] J. Adebahr, P. Johansson, P. Jacobsson, D.R. MacFarlane, M. Forsyth, *Electrochim. Acta* **2003**, *48*, 2283.

[19] G. Francius, A. Razafitianamaharavo, M. Moussa, M. Dossot, E. André, J. Bacharouche, B. Senger, V. Ball, J.F.L. Duval, *J. Phys. Chem. C* **2016**, *120*, 5599.

9. Conclusions and future work

This PhD thesis is focused to the fabrication of core-shell nanocapsules and form-stable nanocomposites as two strategies to form nanoconfined hydrated salts PCMs, aiming to overcome the disadvantages of hydrated salts as PCMs such as leakage, phase separation and degradation during thermal cycling. Halloysite and sepiolite hosts have demonstrated excellent properties for including eutectic hydrated salt into nanoporous mineral matrixes.

The conclusions for various PCM nanocapsule systems are:

-The fabrication of nanocapsules with polyethylcyanoacrylate shell and $NaOAc\cdot 3H_2O$ PCM core by miniemulsion and interfacial polymerisation has not been successful because block material has been obtained instead of nanocapsules because of the very fast polymerisation of ethyl cyanoacrylate in the presence of water.

-The fabrication of nanocapsules with polymethylmethacrylate shell and $Na_2HPO_4\cdot 12H_2O$ PCM core by miniemulsion and solvent evaporation precipitation method formed irregular aggregates of nano/microparticles. The phase separation of $Na_2HPO_4\cdot 7H_2O$ was observed.

-The fabrication of nanocapsules with gelatine shell and $KAl(SO_4)_2\cdot 12H_2O$ PCM core by miniemulsion and thermal denaturation has resulted in nano/microcapsules with diameter from 200 nm to 4 μm. However, the hydrate water of the PCM has been lost during the synthesis leading to no energy uptake/release property of the capsules.

-Nanocapsules with SiO_2 shell and $Na_2SO_4\cdot 10H_2O$ PCM core have been obtained by miniemulsion and sol-gel method with uniform morphology and average diameter of 120 nm. These nanocapsules have shown no phase change peak because the encapsulated $Na_2SO_4\cdot 10H_2O$ degraded at room temperature during storage.

In general, the nanoencapsulation of hydrated salt as PCM in a core-shell structure is not very practical. On one hand, the morphology of the particles was irregular and aggregates were formed due to the complexity of the polymerisation reactions, as shown in polyethylcyanoacrylate and polymethylmethacrylate systems. On the other hand, the shell was not compact enough to prevent the loss of the hydrate water during thermal cycling.

The conclusions for different form-stable eutectic hydrated salt PCM nanocomposite systems are:

-The halloysite nanocomposite with 1:1 mass ratio of $Na_2HPO_4 \cdot 12H_2O$ and $Na_2SO_4 \cdot 10H_2O$ as eutectic hydrated salt (EHS) PCM and halloysite as nanocontainer has been successfully prepared by vacuum impregnation. The nanocomposite has demonstrated no leakage of PCM outside halloysite nanotubes. Its melting enthalpy was 142 $J \cdot g^{-1}$, corresponding to 67% loading efficiency. Its melting temperature was 35.8 ℃, which is suitable for many applications in the low temperature range. The FTIR characterisation has proven that chemical composition of EHS retained in halloysite nanotubes. The XRD characterisation has confirmed high crystallinity of the encapsulated EHS. Most important, it has exhibited excellent thermal cycling performance. No phase change separation has been observed over 50 heat uptake/release cycles. The melting enthalpy reduced only by 7% and the melting temperature shifted only by 0.9 ℃ after 50 cycles.

-The bentonite nanocomposite has demonstrated maximum loading of EHS of 60%. The presence of PCM on the surface of 50% and 60% bentonite has been observed due to the shallow pore structure. Phase separation of EHS and very low melting enthalpy have been found for bentonite samples, which have made bentonite not suitable as the matrix for loading hydrated salt PCM.

-Diatomite form-stable nanocomposites have demonstrated large amount of PCM on the diatomite plate surface, leading to the loss of hydrate water and low melting enthalpy.

-Sepiolite with very high porosity and good swelling property with original 90% EHS loading has shown a perfect phase change property and thermal cycling performance. The melting enthalpy was 185 $J \cdot g^{-1}$. The melting temperature was 38.1 °C, close to the melting temperature of EHS as 38.5 °C. EHS has been absorbed in the nanocomposite interlaced by sepiolite long fibres. The chemical composition of EHS has retained well in sepiolite nanocontainers. No new covalent bonds have been formed between EHS and sepiolite. After 50 thermal cycles, the nanocomposite has shown nearly unchanged melting enthalpy and unchanged melting temperature. The phase separation of EHS was not present over 50 thermal cycles.

In summary, in the research of form-stable hydrated salt PCM nanocomposites, halloysite, bentonite, diatomite and sepiolite as four most common and representative nanoporous natural host minerals have been chosen as matrixes. Due to the porosity, physical morphology of pores, the chemical composition of the matrix material and further its interaction with EHS, halloysite and sepiolite nanocomposites have demonstrated perfect phase change properties and cycling stability.

The nanoconfinement of eutectic Gallium-Indium (EGaIn) as low-temperature liquid metal PCM has been implemented by the nanocapsule systems with the shell materials of gelatine, poly(sodium 4-styrenesulfonate)-poly(diallyldimethyl ammonium chloride) and silica as well as the nanocomposite with halloysite as matrix. The gelatine nanocapsules in the size from 70 nm to 1 μm have been obtained by ultrasonication of EGaIn suspension and thermal denaturation of gelatine. The poly(sodium 4-styrenesulfonate)-poly(diallyldimethyl ammonium chloride) nanocapsules from 180 nm to 1.15 μm have been generated by ultrasonication followed by layer-by-layer deposition of polyelectrolyte polymers. The SiO_2 capsules from 100 nm to 1.8 μm have been fabricated by the sol-gel method. The halloysite nanocomposites have been formed by vacuum impregnation of the suspension of EGaIn nanoparticles. Unfortunately, all the nanoconfined EGaIn systems have exhibited no melting peak due to the oxidation of EGaIn during formation of EGaIn nanoparticles.

As for the future perspective work, form-stable nanocomposites with inorganic PCMs loaded in various nanoporous materials can be further studied, as they could be formed in a simple and environment-friendly procedure with stable morphology and well-retained phase change property of PCM. The main idea is to use natural material available in UK for thermal energy storage.

More characterisations of form-stable PCM nanocomposite systems, such as halloysite and sepiolite form-stable EHS nanocomposites can be carried out to understand the dynamic phase change process. For example, the real-time 3D mappings of the form-stable nanocomposite could be recorded by SEM and TEM over thermal cycling. For new applications of form-stable PCM nanocomposites such as electro-thermal and light-thermal energy transition and storage, properties such as electrical conductivity, thermal conductivity and light absorbability are of research interest.

The crystallisation mechanism of hydrated salts in nanoporous matrixes by form-stable PCM nanocomposites needs to be further researched in order to eliminate the supercooling phenomenon. The influencing parameters such as pore size, pore structures and surface functionality for the crystallisation performance could be systematically and deeply researched.

In this thesis, halloysite and sepiolite form-stable eutectic hydrated salt PCM are found to be excellent PCM nanocomposite systems with good phase change properties and thermal cycling stability. The mineral materials keep the hydrated salt PCM intact during thermal cycling. Mineral nanocontainer materials endow composites with promising merits such as good mechanical properties, good thermal conductivity and flame resistance. These PCM nanocomposite systems can be considered for thermal energy storage in building, waste heat recovery and keeping the temperature of packages or clothes. Due to the high latent heat enthalpy of the hydrated salt PCM and the high loading efficiency, the thermal energy storage capacity of these nanocomposites is much better comparing to organic PCMs. Besides the applications based on the present properties of the nanocomposites, the modification of the materials may lead to some new applications. For example, by adding the magnetic nanoparticles in the nanocomposites, they can harvest magnetic energy and store it as thermal energy. Similarly, by adding photon-capturing materials, they could be efficient in transferring light to thermal energy.

Academic activities

Conference

03. 2014	Poster in 2014 Annual Research Conference in Chemistry, University of Bochum, Bochum, Germany
09. 2016	Attendance in 23th Joint Annual Conference of Chinese Society of Chemical Science and Technology (CSCST) and Society of Chemical Industry (SCI), Newcastle, UK
07. 2017	Attendance in 13th International Conference on Materials Chemistry, Liverpool, UK
03. 2018	Poster in 2018 Annual PhD Poster Session, University of Liverpool, Liverpool, UK
11. 2018	Poster in 2018 National Young Scholar Nanomaterial Forum, Xi’an, China
01. 2019	Talk in 2019 Annual PhD Talk Session in Chemistry, University of Liverpool, Liverpool, UK
10. 2019	Attendance in 2019 Workshop on Development of Complex Materials and Self-Regulating Chemical Systems, University of Liverpool, Liverpool, UK
12. 2019	Poster in 2019 International Conference on Green Energy and Recycling, Berlin, Germany

Research Exchange Stay

09.2018 - 12.2018	Northwestern Polytechnical University, Xi‘an, China

Publication

Xiaolei Zhu, Dmitry Shchukin, Crystallohydrate loaded Halloysite Nanocontainers for Thermal Energy Storage Adv. Energy Mater. in Nov. 2018

Xiaolei Zhu, Dmitry Shchukin, Sepiolite form-stable hydrated salt PCM, submitted in 2020